
DESIGN, FABRICATION AND TESTING OF A TIMED-ARRAY OF TEM HORNS FOR BEAM STEERING

Dave V. Giri et al.

Pro-Tech
11-C Orchard Court
Alamo, CA 94507-1541

November 2001

Final Report

APPROVED FOR PUBLIC RELEASE; DISTRIBUTION IS UNLIMITED.



AIR FORCE RESEARCH LABORATORY
Directed Energy Directorate
3550 Aberdeen Ave SE
AIR FORCE MATERIEL COMMAND
KIRTLAND AIR FORCE BASE, NM 87117-5776

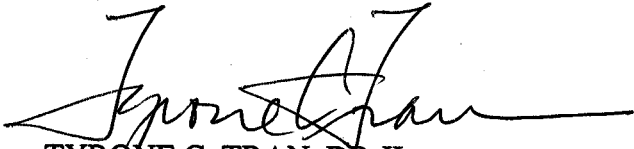
Using Government drawings, specifications, or other data included in this document for any purpose other than Government procurement does not in any way obligate the U.S. Government. The fact that the Government formulated or supplied the drawings, specifications, or other data, does not license the holder or any other person or corporation; or convey any rights or permission to manufacture, use, or sell any patented invention that may relate to them.

This report has been reviewed by the Public Affairs Office and is releasable to the National Technical Information Service (NTIS). At NTIS, it will be available to the general public, including foreign nationals.

If you change your address, wish to be removed from this mailing list, or your organization no longer employs the addressee, please notify AFRL/DEHP, 3550 Aberdeen Avenue SE, Kirtland AFB, NM 87117-5776

Do not return copies of this report unless contractual obligations or notice on a specific document requires its return.

This report has been approved for publication.



TYRONE C. TRAN, DR-II
Project Manager



PAUL L. THEE, Lt Col, USAF
Chief, High Power Microwave Division



R. EARL GOOD, SES
Director, Directed Energy

REPORT DOCUMENTATION PAGE			<i>Form Approved</i> <i>OMB No. 0704-0188</i>	
Public reporting burden for this collection of information is estimated to average 1 hour per response, including the time for reviewing instructions, searching existing data sources, gathering and maintaining the data needed, and completing and reviewing this collection of information. Send comments regarding this burden estimate or any other aspect of this collection of information, including suggestions for reducing this burden to Department of Defense, Washington Headquarters Services, Directorate for Information Operations and Reports (0704-0188), 1215 Jefferson Davis Highway, Suite 1204, Arlington, VA 22202-4302. Respondents should be aware that notwithstanding any other provision of law, no person shall be subject to any penalty for failing to comply with a collection of information if it does not display a currently valid OMB control number. PLEASE DO NOT RETURN YOUR FORM TO THE ABOVE ADDRESS.				
1. REPORT DATE (DD-MM-YYYY) November 2001		2. REPORT TYPE Final Report		3. DATES COVERED (From - To) September 1999 – September 2001
4. TITLE AND SUBTITLE Design, Fabrication and Testing of a Timed-Array of TEM Horns for Beam Steering			5a. CONTRACT NUMB F29601-99-C-0165	
			5b. GRANT NUMBER N/A	
			5c. PROGRAM ELEMENT NUMBER 65502F	
6. AUTHOR(S) David V. Giri Vic Carboni* and Heinz Lackner*			5d. PROJECT NUMBER 3005	
			5e. TASK NUMBER D0	
			5f. WORK UNIT NUMBER CK	
7. PERFORMING ORGANIZATION NAME(S) AND ADDRESS(ES) Pro-Tech 11-C Orchard Court Alamo, CA 94507-1541			8. PERFORMING ORGANIZATION REPORT NUMBER	
9. SPONSORING / MONITORING AGENCY NAME(S) AND ADDRESS(ES) AFRL/DEHP 3550 Aberdeen Ave SE Kirtland AFB, NM 87117-5776			10. SPONSOR/MONITOR'S ACRONYM(S) AFRL	
			11. SPONSOR/MONITOR'S REPORT NUMBER AFRL-DE-TR-2001-1085	
12. DISTRIBUTION / AVAILABILITY STATEMENT APPROVED FOR PUBLIC RELEASE; DISTRIBUTION IS UNLIMITED.				
13. SUPPLEMENTARY NOTES *TITAN Systems Corporation Pulse Sciences Division 2700 Merced Street San Leandro, CA 94577				
14. ABSTRACT The objective of this study is to demonstrate one-dimensional steerability of a linear array of TEM horn antennas, using the true-time delay approach. Three TEM horns have been fabricated and tested in an array configuration. Initially, the boresight radiation of a single TEM horn is measured at low-voltages, and seen to be in agreement with theoretical models. To demonstrate the linearity, limited measurements were also performed using a 300 kV pulser with a single antenna completely immersed in oil. In a linear array configuration, the three TEM horns can be excited simultaneously or in some prescribed time sequence. Controlling the time sequence of excitation of the individual elements, the radiated beam can be configured to have its peak on boresight or at some angle in the azimuth. Although fixed time delays were introduced in this experiment, future transient arrays are expected to be excited with triggered switches developed in this effort and described in a separate report.				
15. SUBJECT Timed-array antennas, Beam steering, TEM horn array, Time-delay, Linear Array				
16. SECURITY CLASSIFICATION OF:			17. LIMITATION OF ABSTRACT Unlimited	18. NUMBER OF PAGES 100
a. REPORT Unclassified	b. ABSTRACT Unclassified	c. THIS PAGE Unclassified		

TABLE OF CONTENTS

Section	Page
1.0 INTRODUCTION	1
2.0 THEORETICAL MODELING OF THE TEM HORN	2
2.1 Physical Model.....	2
2.2 Elementary Sources in Transient Regime.....	4
2.3 Radiations From the TEM Horn	7
2.4 Horn Edge Matching.....	11
2.5 The TEM Horn Radiation Pattern.....	12
2.6 “Time Array” in Comparison to “Phase Array” Antennas	13
2.6.1 Phase Array Analysis Time Domain.....	13
2.6.2 The Transient Regime.....	16
2.6.3 Additional Considerations	21
3.0 EXPERIMENTAL SETUP AND EQUIPMENT.....	24
3.1 Pulser	24
3.2 Source Voltage Characteristics.....	24
3.3 Ground Plane B-dot Sensor	26
3.4 Experimental Setup.....	27
4.0 TERMINATION CONSIDERATIONS	31
5.0 TEM HORN ARRAY STEERING CONSIDERATION.....	34
6.0 LOW-VOLTAGE DATA-TAKE MEASUREMENT LOG (SUMMARY).....	35
7.0 LOW VOLTAGE SIMULTANEOUS MEASUREMENTS	37
7.1 On Axis	37
7.2 Horizontal Radiation Pattern.....	39
8.0 LOW-VOLTAGE “TIME ARRAY” MEASUREMENTS	44
8.1 On Axis	44
8.2 Horizontal Radiation Pattern.....	44
9.0 HIGH-VOLTAGE MEASUREMENTS.....	46
10.0 SUMMARY	49
REFERENCES	50
APPENDIX A.....	51
APPENDIX B	55
APPENDIX C	56
APPENDIX D.....	93
Distribution List.....	94

1.0 INTRODUCTION

The objective of this study was to demonstrate one-dimensional steerability of multi-TEM horn configuration using true time delay approach. The electric field values were derived using the measured values of temporal rate of change of magnetic induction ($\partial B/\partial t$), commonly referred to as B-dot.

We have built and tested three TEM horn configuration in the laboratory environment, where 2.5 kV solid state pulser with $t_{10-90}=169$ ps and was used to energize the antenna system. The radiated field was calculated in the horizontal plane along three directions: on boresight, along the axis 26.57° off the boresight and at the range of 300 cm along a circular arc centered at the central TEM horn. Each horn in the three-horn system was energized sequentially to yield the maximum power along 26.57° off the boresight axis. Electric field measurements show peak value at 29.89° off boresight. We believe that the discrepancy between the measured and theoretical value of the angle where maximum occurs is due to errors in cable cuts. It should be noted that 1 mm error in cable cut correspond to 4 ps error in true time delay.

Three different inductance loads (low, medium and high) were used in the back of horn aperture for the determination of an optimal configuration that will minimize the radiated energy in the backward direction at low frequencies, when the array element can be characterized by a set of electric (\vec{p}) and magnetic (\vec{m}) dipole moments.

To show a scalability of the experiments, a limited number of high-voltage measurements along the boresight were carried out using 300-kV pulser and one TEM horn completely submerged in oil. The results show $(1/r)$ dependence of the field in far zone, as expected.

Finally, we have developed theoretical time-domain formulation and models for radiation along a boresight for a single TEM horn, and fair agreement between theoretical and experimental results is shown. Moreover, theoretical comparison between phased array antennas and “timed” array antennas shows large degree of similarity. In particular, the formulation for an effective radiation lobe width (similar to 3-dB concept in the phased arrays) is presented and uniform and non-uniform (tapered) antenna element excitations are discussed.

2.0 THEORETICAL MODELING OF THE TEM HORN

2.1 Physical Model

Let us consider the TEM horn as depicted in figure 1. The horn is modeled as a transmission line of a constant characteristic impedance Z_c and wave speed c , so that signals propagate with the speed of light in vacuum, c . Furthermore, let's assume that the horn is driven by a voltage:

$$v_0(t) = 2 V_0 u(t) \quad (1)$$

where $u(t)$ is the applied signal waveform, and that the source is matched to the transmission line, as shown in figure 2.

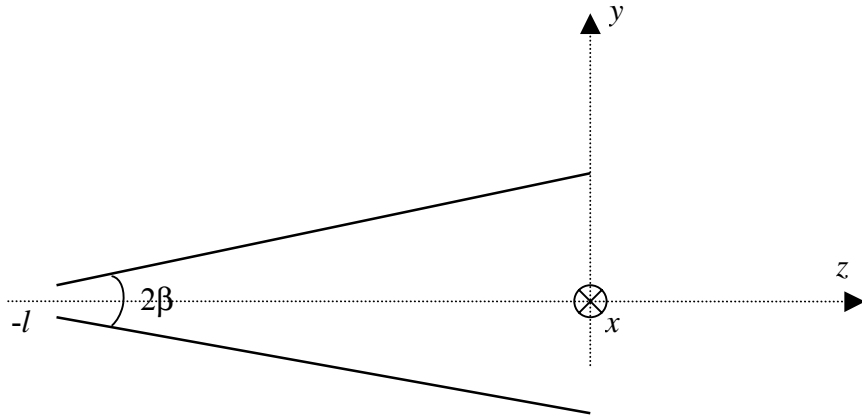


Figure 1. Geometry of the problem

In the transmission line model we assume that the end of the line behaves as an open circuit.

Accordingly, the voltages and the currents along the line are:

$$\begin{aligned} v(z,t) &= Z_c I_0 \left[u \left(t - \frac{l}{c} - \frac{z}{c} \right) + u \left(t - \frac{l}{c} + \frac{z}{c} \right) \right] \\ i(z,t) &= I_0 \left[u \left(t - \frac{l}{c} - \frac{z}{c} \right) - u \left(t - \frac{l}{c} + \frac{z}{c} \right) \right] \end{aligned} \quad (2)$$

where $V_0 = I_0 Z_c$.

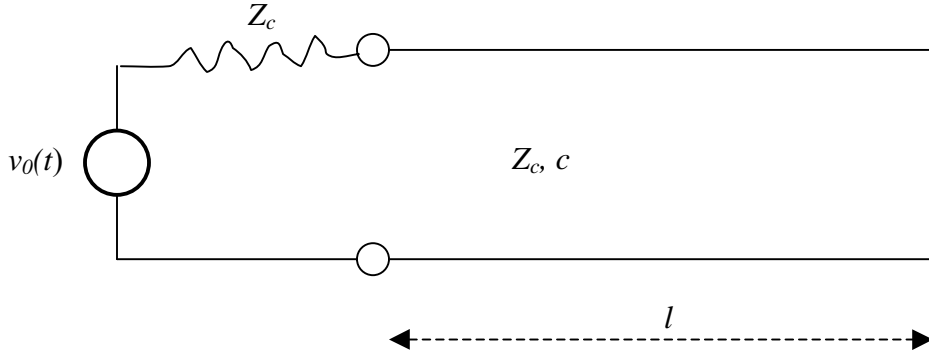


Figure 2. Equivalent transmission line excitation

For the subsequent analysis it is convenient to refer to charge density $q(z,t) = C' v(z,t)$ and magnetic flux density, $\Psi(z,t) = L' i(z,t)$, where C' and L' are the capacitance and inductance per unit length of transmission line respectively. Since,

$$cZ_c = 1/C' \quad \text{and} \quad c/Z_c = 1/L' \quad (3)$$

it follows that equation (2) becomes,

$$\begin{cases} q(z,t) = \frac{I_0}{c} \left[u\left(t - \frac{l}{c} - \frac{z}{c}\right) + u\left(t - \frac{l}{c} + \frac{z}{c}\right) \right] \\ \Psi(z,t) = \frac{Z_c I_0}{c} \left[u\left(t - \frac{l}{c} - \frac{z}{c}\right) - u\left(t - \frac{l}{c} + \frac{z}{c}\right) \right]. \end{cases} \quad (4)$$

The above charge and magnetic flux densities generate elementary electric \vec{p} and magnetic \vec{m} dipole moment densities along the TEM horn (see figure 3):

$$\begin{aligned} \vec{p}(z,t) &= q(z,t)h\vec{1}_y = 2q(l+z,t)\tan(\beta)\vec{1}_y \\ \vec{m}(z,t) &= \Psi(z,t)h\vec{1}_x = 2\Psi(l+z,t)\tan(\beta)\vec{1}_x \end{aligned} \quad (5)$$

where $\vec{1}_x$ and $\vec{1}_y$ are unit vectors along x and y coordinate axes, respectively.

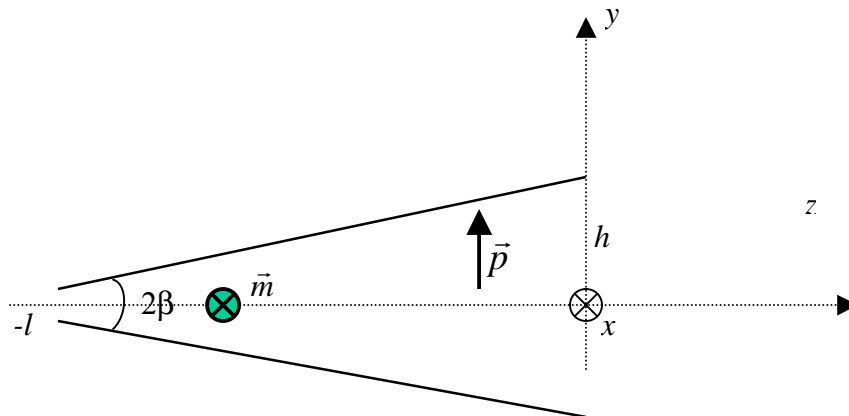


Figure 3. Electric and magnetic dipole moment densities along the TEM horn.

We model the radiation from the TEM horn in terms of these equivalent sources. It is explicitly noted that $m=Z_c p$ and that Z_c coincides with the free-space intrinsic impedance.

2.2 Elementary Sources in Transient Regime

Consider elementary electric and magnetic dipole moments, $p \Delta l \vec{1}_z$ and $m \Delta l \vec{1}_z$ ($\vec{1}_z$ is a unit vector along the z -coordinate), referred to a spherical coordinate system, see figure 4.

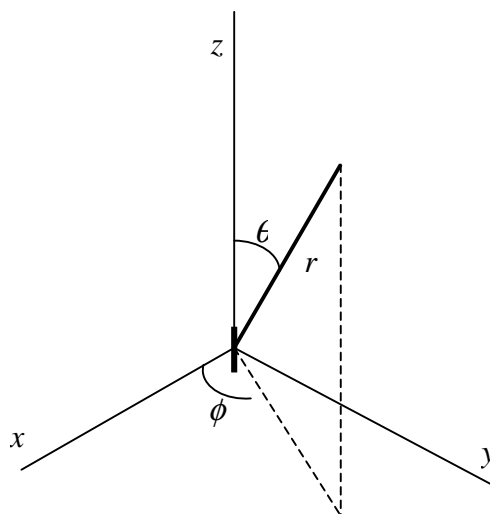


Figure 4. The spherical coordinate system

For the radiation from electric dipole we have,

$$\begin{cases} E_r^e = \frac{Z_c \Delta l}{2\pi} \left[\frac{\dot{p}(t^*)}{r^2} + \frac{cp(t^*)}{r^3} \right] \cos \theta \\ E_\theta^e = \frac{Z_c \Delta l}{2\pi} \left[\frac{\ddot{p}(t^*)}{cr} + \frac{\dot{p}(t^*)}{r^2} + \frac{cp(t^*)}{r^3} \right] \sin \theta \\ H_\phi^e = \frac{Z_c \Delta l}{2\pi} \left[\frac{\ddot{p}(t^*)}{cr} + \frac{\dot{p}(t^*)}{r} \right] \sin \theta. \end{cases} \quad (6)$$

where $t^* = t - r/c$ is the retarded time and a dot implies derivative with respect to time. Similarly, for the magnetic dipole we have,

$$\begin{cases} H_r^m = \frac{\Delta l}{2\pi Z_c} \left[\frac{\dot{m}(t^*)}{r^2} + \frac{cm(t^*)}{r^3} \right] \cos \theta \\ H_\theta^m = \frac{\Delta l}{4\pi Z_c} \left[\frac{\ddot{m}(t^*)}{cr} + \frac{\dot{m}(t^*)}{r^2} + \frac{cm(t^*)}{r^3} \right] \sin \theta \\ E_\phi^m = -\frac{\Delta l}{4\pi} \left[\frac{\ddot{m}(t^*)}{cr} + \frac{\dot{m}(t^*)}{r} \right] \sin \theta. \end{cases} \quad (7)$$

We first must present a suitable definition for the far field at large distances. When the excitation is sinusoidal it is related to the wavelength, but there is no unique value of wavelength here. Consider the pulse having Gaussian shape,

$$u(t) = \exp\left(-\frac{t^2}{T^2}\right) \quad (8)$$

which describes the time variation of the dipole moments, proportional to the voltage and the current for the electric and magnetic case (see equation 4). We have:

$$\dot{u}(t) = \frac{-2t}{T^2} \exp\left(-\frac{t^2}{2T^2}\right) \quad (9)$$

$$\ddot{u}(t) = -\frac{2}{T^2} \left(1 - \frac{t^2}{T^2}\right) \exp\left(-\frac{t^2}{2T^2}\right) \quad (10)$$

Clearly, for the order of magnitude we have

$$\left| \begin{array}{l} \frac{\ddot{p}}{\dot{p}} = \frac{\ddot{m}}{\dot{m}} = \frac{\ddot{u}}{\dot{u}} \sim \frac{r}{cT} \\ \frac{\dot{p}}{p} = \frac{\dot{m}}{m} = \frac{\dot{u}}{u} \sim \frac{r}{cT}, \end{array} \right. \quad (11)$$

We conclude that in the equations for the fields (equations 6 and 7) the terms containing the second time derivatives are dominant provided we are at the distances large compared to the effective spatial extension of the pulse, namely,

$$r \gg 2cT \quad (12)$$

Consequently, equations 6 and 7 can be simplified as follows, provided equation (12) is satisfied.

$$E_{\theta}^e = \frac{Z_c \Delta l}{4\pi} \frac{\ddot{p}(t^*)}{cr} \quad H_{\phi}^e = E_{\theta}^e / Z_c \quad (13)$$

$$E_{\phi}^e = -\frac{\Delta l}{4\pi} \frac{\ddot{m}(t^*)}{cr} \quad H_{\theta}^m = E_{\phi}^m / Z_c \quad (14)$$

Consider now the situation depicted in figure 3, wherein the electric dipole is oriented along the y -axis and the magnetic dipole along the x -axis. We are interested in the far field in the plane $y=0$. The previous results yield:

$$\vec{E} = \vec{E}^e + \vec{E}^m = E \vec{1}_y = -\frac{\Delta l}{4\pi cr} [Z_c \ddot{p}(t^*) - \ddot{m}(t^*) \cos \theta] \vec{1}_y \quad (15)$$

where θ is the azimuthal angle about the y -axis and measured from the positive z -axis. If the Huygens condition is satisfied, namely,

$$Z_c \ddot{p} = \ddot{m}, \quad (16)$$

then the electric field is

$$E = -\frac{\ddot{m}(t^*) \Delta l}{2\pi cr} \sin^2\left(\frac{\theta}{2}\right) \quad (17)$$

and the radiation pattern in the plane is represented by a cardioid, with its maximum at $\theta=180^\circ$. The generation of the cardioid pattern is shown in figure 5.

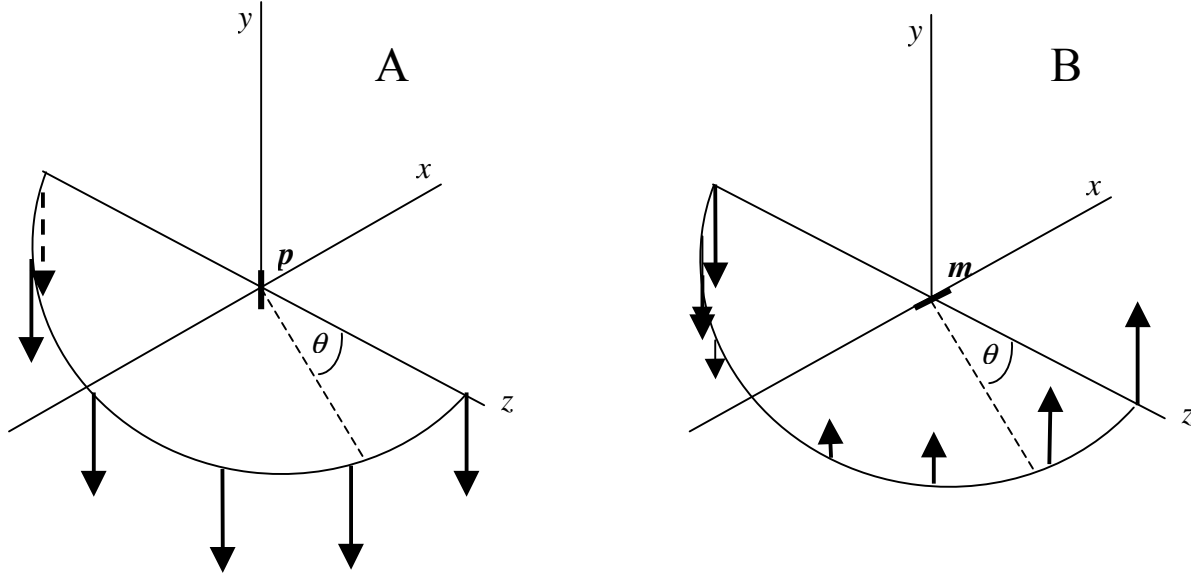


Figure 5. Electric field radiated over the plane $y=0$ by an electric (A) and magnetic (B) dipole.

Should the sense of the magnetic dipole be reversed, we would get

$$E = -\frac{\ddot{m}(t^*)\Delta l}{2\pi cr} \cos^2\left(\frac{\theta}{2}\right) \quad (18)$$

and the maximum radiation is at $\theta = 0^\circ$. Note that the patterns given by equations 16 and 17 are those typical of a Huygens source.

2.3 Radiation From the TEM Horn

Consider the open ended TEM horn with charge and flux densities given by equation (3). Clearly, the charge $q(z)dz$ at a point z generates an elementary electric dipole:

$$\vec{p} = 2q(z)dz(l+z)\tan(\beta)\vec{1}_y = Q\left[u\left(t-\frac{l}{c}-\frac{z}{c}\right)+u\left(t-\frac{l}{c}+\frac{z}{c}\right)\right](l+z)\vec{1}_y \quad (19)$$

with $Q = 2I_0 \tan(\beta/c)$ [Coulomb/m]. Similarly the magnetic flux $2\Psi(z)\tan\beta dz$ generates a magnetic moment:

$$\vec{m} = 2\Psi(z)dz(l+z)\tan(\beta)\vec{1}_x = Z_c Q \left[u\left(t - \frac{l}{c} - \frac{z}{c}\right) + u\left(t - \frac{l}{c} + \frac{z}{c}\right) \right] (l+z)\vec{1}_x \quad (20)$$

We now can proceed with computation of the far field at a point $P(0,0,r)$ on the z -axis (see figure 3) by evaluating separately the contributions from the direct and reflected wave. For the radiation due to the direct wave we have $\vec{p} = p\vec{1}_y$ and $\vec{m} = m\vec{1}_x$ with $m = Z_c p$, so that condition of equation (16) is verified. Accordingly, the field at point P is zero because result in equation (17) is obtained. This is at variance of the specular point P' with respect to the plane $z=0$, where the field reaches its maximum given by equation. (17) with $\theta=180^\circ$. We now compute the amplitude of the electric field in the far zone ignoring the cardioid pattern. Obviously, the magnetic field is proportional to the electric field via the intrinsic admittance of free space. Each field contribution is proportional to the retarded signal:

$$\ddot{u}\left(t - \frac{l+z}{c} - \frac{l}{c} - \frac{z}{c}\right), \quad (21)$$

(note that the origin of the coordinate system is set at the end of the TEM horn, and that the distance r is measured from there), and hence we have:

$$\begin{aligned} E &= -Z_c \frac{Q}{2\pi cr} \int_{-l}^0 \ddot{u}\left(t - \frac{r}{c} - \frac{l}{c} - \frac{2z}{c}\right)(l+z)dz \\ &= Z_c \frac{Q}{4\pi r} \left\{ \dot{u}\left(t - \frac{r}{c} - \frac{l}{c}\right) - \frac{c}{2l} \left[u\left(t - \frac{r}{c} + \frac{l}{c}\right) - u\left(t - \frac{r}{c} - \frac{l}{c}\right) \right] \right\} \\ &= Z_c \frac{Q}{4\pi r} \left\{ \dot{u}\left(t^* - \frac{2l}{c}\right) - \frac{c}{2l} \left[u\left(t^*\right) - u\left(t^* - \frac{2l}{c}\right) \right] \right\} \end{aligned} \quad (22)$$

where integration by parts has been implemented. In equation. (22) the retarded time is defined as:

$$t^* = t - \frac{r-l}{c}, \quad (23)$$

which implies shifting the origin of the coordinate system to the tip of the TEM horn.

For the computation of radiation due to the reflected wave, the situation is similar to the one just presented, with the only exception that the sign of the magnetic dipole is reversed. This implies that the field is maximum along the positive z -axis and it is suitable to use equation (18) for computing the radiation pattern. The retarded signal analogous to equation (21) is:

$$\ddot{u}\left(t - \frac{r-z}{c} - \frac{l}{c} + \frac{z}{c}\right); \quad (24)$$

and we have:

$$\begin{aligned} E &= -Z_c \frac{Q}{2\pi cr} \int_{-l}^0 \ddot{u}\left(t - \frac{r}{c} - \frac{l}{c} + \frac{2z}{c}\right)(l+z) dz \\ &= -Z_c \frac{Q}{4\pi r} \left\{ \dot{u}\left(t - \frac{r}{c} - \frac{l}{c}\right) - \frac{c}{2l} \left[u\left(t - \frac{r}{c} - \frac{l}{c}\right) - u\left(t - \frac{r}{c} - \frac{3l}{c}\right) \right] \right\} \\ &= -Z_c \frac{Q}{4\pi r} \left\{ \dot{u}(t^*) - \frac{c}{2l} \left[u(t^*) - u\left(t^* - \frac{2l}{c}\right) \right] \right\} \end{aligned} \quad (25)$$

where now the retarded time is defined as:

$$t^* = t - \frac{r+l}{c} \quad (26)$$

and again the origin of the coordinate system is at the tip of TEM horn.

A physical picture of the radiation properties of the horn is now in order. The two waves, direct and reflected one, generate identical patterns, each the specular reflection of the other. The radiation is in the opposite direction of the wave propagation; this is consistent with the impossibility of signals to propagate with speeds higher than the speed of light. As a matter of fact, the equivalent dipoles already move with such speed and no radiation can take place in the direction of propagation. Additional physical insight is obtained by assuming $u(t)=U(t)$, a unity

step function. Figure 6 presents direct and reflected waves (equations 22 and 25) as function of the retarded time t^* .

Let's first consider the direct wave radiation (figure 6A). The signal $u(t)=U(t)$ is applied at time $t=0$ and is received at times $t>(r-l)/c$. At the tip of the horn (at $r=l$), the signal is generated at time $t=0$, which is consistent with causality. The wave is launched at $t=0$ at the tip and terminates at $t=l/c$ at the end of the horn. One would expect the Dirac pulses to be present in the radiated field at the same times due to the excitation discontinuities. And, as a matter of fact, the Dirac pulses generated at the end of the horn at time $t=l/c$ correctly shows up at the retarded time $t^*=2l/c$ (see Fig.6A), but the other Dirac pulse is missing. The reason is that in the adopted model the horn extends up to the tip, where the equivalent radiating dipoles exhibit zero moment (because the distance between the two faces of the horn approaches zero), so that no radiation takes place. Should the horn start at the point $-(l+z_0)$ instead of $-l$, the extra Dirac pulse would be recovered. Note also that the area of the $\text{rect}(\bullet)$ function, shown in figure 6A, equals the area of the Dirac pulse and has an opposite sign.

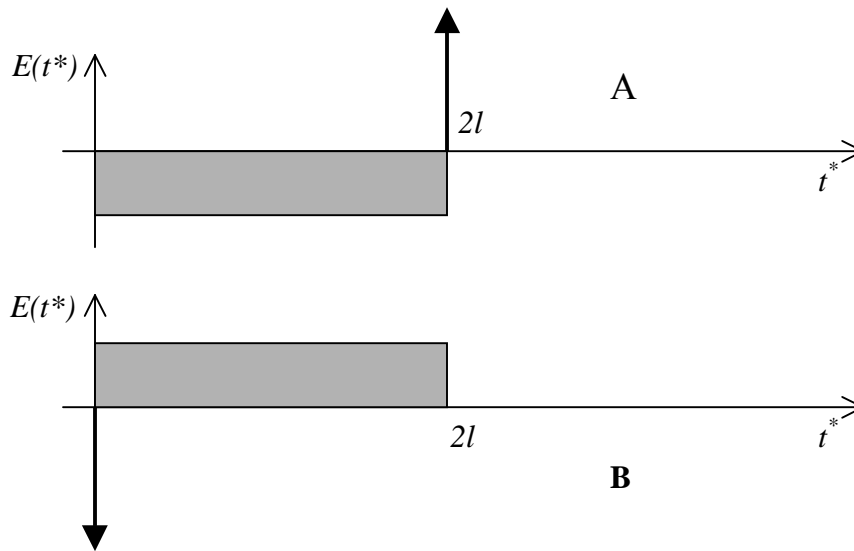


Figure 6. Far-field radiation patterns for the direct (A) and reflected (B) waves.

Similar concepts can be exploited for the reflected wave, figure 6B. The signal is received at $t>(r+l)/c>l/c$. Accordingly, the wave starts radiating when it reaches the end of the horn, which is again consistent with causality. The sudden discontinuity provided by the appearance of the

reflected wave generates the Dirac pulse, see figure 6B. No further Dirac pulse is generated when the reflected wave arrives at the tip of the horn, where it is fully absorbed by the equivalent dipole moments that smoothly disappear because the distance between the faces of the horn approaches zero. Also in this case the compensation between the areas of the $\text{rect}(\bullet)$ function and the Dirac spike has taken place.

2.4 Horn Edge Matching

For a number of reasons it is desirable to match the impedances at the very end of the horn. This can be accomplished by loading it with a resistance R_L equal to Z_c , the characteristic impedance of the TEM horn. However, in this case only the direct wave is present and no forward radiation is obtained (see Section 2.3). To circumvent this difficulty the horn can be “reversed” by closing it in a loop whose total resistance should match Z_c . For a half horn over a ground plane, the situation is depicted in figure 7, with a side view and two top views showing the horn closure with a wire or another superposed horn.

If matching is perfect, the reflected wave will be missing in the main horn, however, a forward wave moving along the z -axis is generated in the adjoined horn. The situation is not different from that examined in the previous section, namely the same two patterns, a forward (from the adjoined horn) and a backward (from the main horn) are generated.

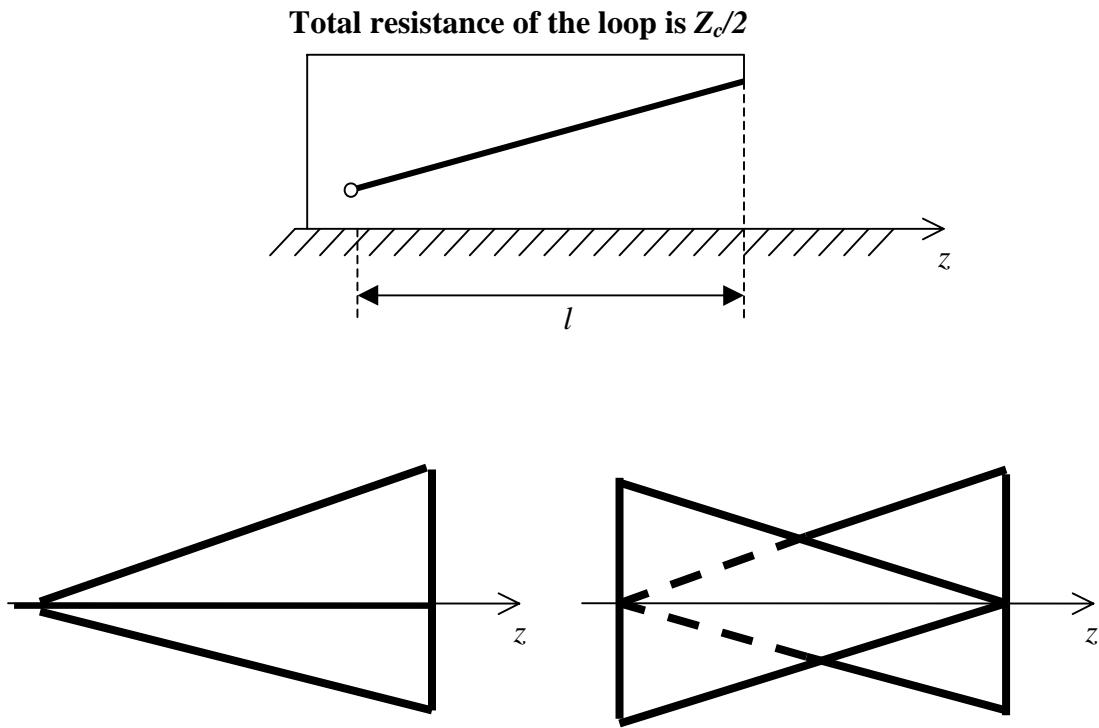


Figure 7. TEM horn matched configurations

2.5 The TEM Horn Radiation Pattern

The radiation pattern of the couple of elementary electric and magnetic dipoles has been examined in Section 2.2. The radiation pattern of the horn, however, is more complex, as it appears from the examination of figure 8.

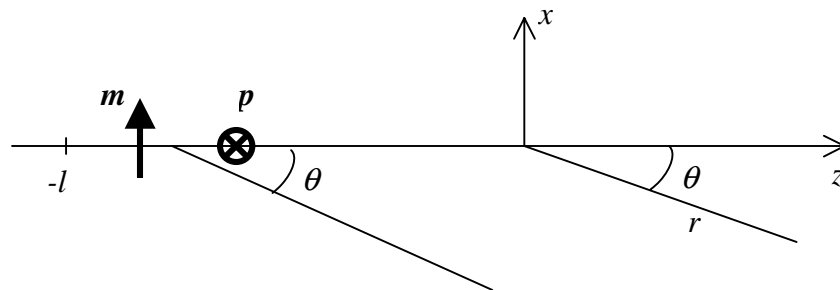


Figure 8. Diagram for computation of the horn radiation pattern in the $y=0$ plane.

Computations can be carried out along the same lines as described in Section 2.3; however, a new corrected version of the retarded time must be adopted, as suggested by figure 8. For the direct wave we have:

$$u\left(t - \frac{r + z \cos \theta}{c} - \frac{l}{c} - \frac{z}{c}\right), \quad (27)$$

while the expression for the reflected wave is

$$u\left(t - \frac{r - z \cos \theta}{c} - \frac{l}{c} + \frac{z}{c}\right). \quad (28)$$

It is recognized that the horn behaves as a small timed array or, more precisely, as a timed aperture. All arguments presented in Section 2.3 support the fact that the horn is essentially a combination of timed end-fire and back-fire antennas.

2.6 “Timed Array” in Comparison to “Phased Array” Antennas

2.6.1 Phased Array Analysis in Time Domain

Consider a linear array of N elements, with a constant spacing d between the elements,

each one radiating the same waveform $f(t)$.

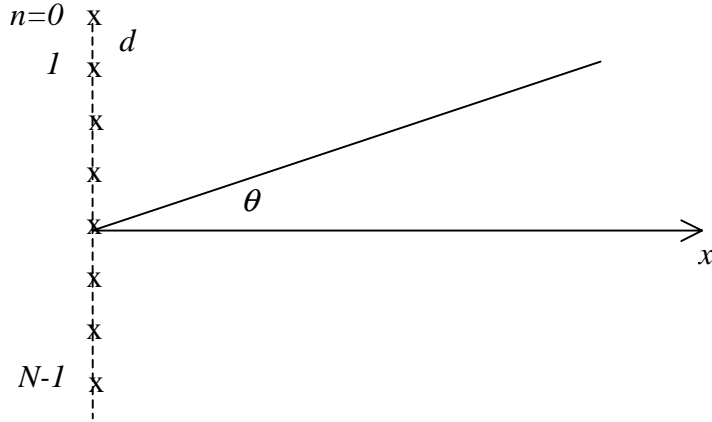


Figure 9. A linear array of N equally-spaced elements

The array factor (in a non-normalized form) describing the angular dependence of the radiated field is

$$F(t, \theta) = \sum_0^{N-1} f(t - n\Delta t), \quad \Delta t = d \sin \theta / c \quad (29)$$

where c is the speed of light in vacuum. It is important to recognize that this factor not only depends on the angle θ , and the distance from the array, but also on the shape of the radiated waveform. If we assume the waveform to be sinusoidal:

$$f(t) = A \cos \omega t \quad (30)$$

then equation (29) becomes

$$\begin{aligned} 4\pi r F(t, \theta) &\sim \sum_0^{N-1} \cos[\omega(t - n\Delta t)] = \frac{1}{2} \sum_0^{N-1} \exp[i\omega(t - n\Delta t)] + cc \\ &= \frac{\exp(i\omega t)}{2} \sum_0^{N-1} \exp(-i\frac{\omega}{c} nd \sin \theta) + cc \end{aligned} \quad (31)$$

where cc is complex conjugate of the term it follows.

First of all, we immediately recognize the usual expression for the phased array. However, since the follow-on derivation is in time domain, from now on we'll use the term "timed array" instead of the "phased array". Furthermore, we'll refer to time delays Δt instead of phase shifts $(\omega \sin \theta)/c$. Let

$$\begin{aligned}
 \sum_0^{N-1} \exp(-i \frac{\omega}{c} nd \sin \theta) &= \sum_0^{N-1} \exp(-i \beta nd \sin \theta) \\
 &= \exp(-i \frac{N-1}{2} \beta d \sin \theta) \frac{\sin(\frac{N}{2} \beta d \sin \theta)}{\sin(\frac{\beta d}{2} \sin \theta)} \\
 &= Q(\theta) \exp[i \psi(\theta)],
 \end{aligned} \tag{32}$$

where $\beta = \omega/c = 2\pi/\lambda$, λ being the wavelength associated with a sinusoidal signal. Then,

$$4\pi r F(\theta) \sim Q(\theta) \cos[\omega t + \psi(\theta)], \tag{33}$$

which shows that, for the particular case of sinusoidal signal, the shape of the radiation waveform does not change with the angle: only its amplitude and phase are modulated by the two angle-dependent factors $Q(\theta)$ and $\psi(\theta)$, respectively. Note that the phased modulation is usually ignored in the conventional phased array analysis, because this is done directly in the transformed (frequency) Fourier domain and its time domain counterpart usually is not used.

If for now we neglect the phase modulation, we conclude that this particular sinusoidal waveform is only amplitude-scaled, when the observation angle θ changes.

It is therefore natural to assess the effective angular width $\Delta\theta_0$ within which this down-scaling can be tolerated. Assuming $\Delta\theta_0 = 2\theta_0$ with $Q(\theta_0) = 0.707$, as usual, we have

$$\frac{N\beta d}{2} \sin \theta \approx \frac{\pi}{2} \tag{34}$$

and for large arrays we get

$$\frac{Nd}{2}\theta_0 \approx \frac{1}{2} \quad \Delta\theta_0 = \frac{\lambda}{Nd} \quad (35)$$

A more general approach, not restricted to a particular sinusoidal waveform, could be implemented. Consider the radiated signal along the broadside. Ignoring a non-essential constant factor, the signal is given by $\cos\omega t$ and its value along the direction θ is equal to $Q(\theta)\cos[\omega t + \psi(\theta)]$. We can enforce the following alternative definition for the effective angular width:

$$[1 - Q(\theta_0)]^2 = \xi \quad (36)$$

wherein $0 < \xi < 1$ is the “similarity factor”: it serves as a measure of the “distance” (or deviation) between the envelopes of the radiated field along the broadside and θ_0 direction using quadratic norm. Accordingly, the value of ξ close to zero implies that the envelopes of the radiated waveforms inside the angular width $\pm\theta_0$ are “similar” in the sense described above. By enforcing the condition $Q(\theta_0) = 0.707$ we get $\xi = 0.085 \sim 0.1$. This particular value of the “similarity” factor enforces the same condition for $\Delta\theta_0$ as the one given by equation (35).

2.6.2 The Transient Regime

Let us remove the restriction that the radiated waveform is sinusoidal. In this case we are not concerned about the radiated field envelopes, but rather the radiated fields themselves. For this reason the definition given by equation (36) is modified as follows:

$$\int_{-\infty}^{+\infty} dt [F(t, \theta) - F(t, \theta_0)]^2 = \xi \int_{-\infty}^{+\infty} dt F^2(t, 0) \quad (37)$$

which represents the mean square deviation between the signals along the broadside and θ_0 directions; or, more precisely, between the energies of the two signals, because integration with respect to time is implemented. Assume now that the radiated waveform is a rectangular pulse of duration T . Furthermore, we define

$$\Delta t_0 = \frac{d \sin \theta_0}{c} \quad (38)$$

the time delay between signals received along the direction θ_0 from adjacent radiating elements. Let $N\Delta t < T$. The shape of the received signal is shown in figure 10 for the case $N=4$ and pulses of unit amplitude.

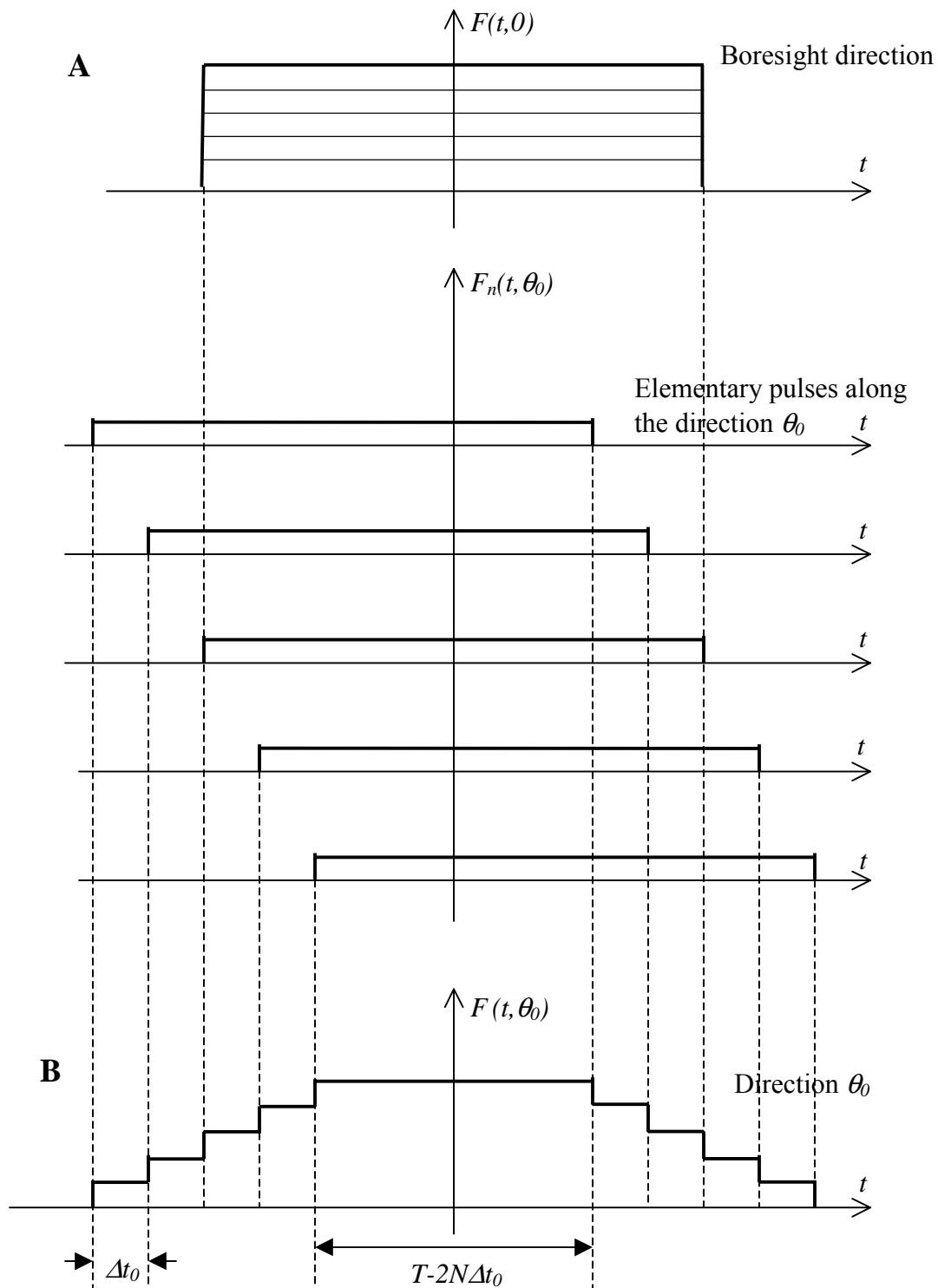


Figure 10. Received signal along $\theta = 0^\circ$ (A) and $\theta = \theta_0$ (B) from a 5-element linear array, where each element radiates a rectangular pulse of duration T

Inspection of figure 10 allows evaluation of the difference inside the brackets of equation (37). As a matter of fact, when we subtract $F(t, \theta_0)$ from $F(t, 0)$ we obtain the result depicted in figure 11.

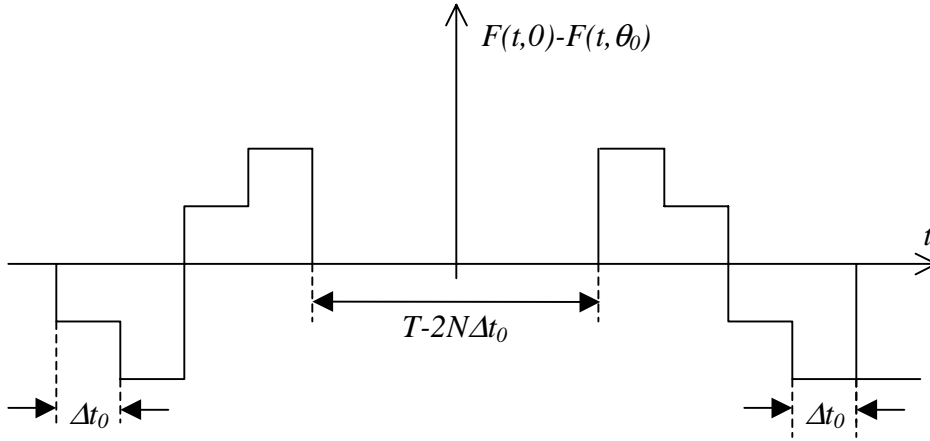


Figure 11. Graphical presentation of the difference $F(t, 0) - F(t, \theta_0)$

And now it is evident that square of this difference is given by

$$4[F(t, 0) - F(t, \theta_0)]^2 = 4 \sum_1^N n^2 = 4 \frac{N(N+1)(2N+1)}{6} \quad (39)$$

By enforcing equation (37) we get

$$4\Delta t_0 \sum_1^{N1} n^2 = \Delta t_0 \frac{2(N+1)N(2N+1)}{3} = \xi(2N+1)^2 T \quad (40)$$

i.e.,

$$\frac{1}{6} \left(2N+1 - \frac{1}{2N+1} \right) \Delta t_0 = \xi T \quad (41)$$

Making use of equation (38) for Δt , we conclude that for large arrays

$$\theta_0 \approx \frac{cT}{(2N+1)a} 6\xi \quad (42)$$

so that the effective angular width of the array radiating system is proportional to the ratio of the spatial width of the pulse, cT , to the total length of the array $(2N+1)a$.

It is interesting to note that for $\xi=0.085$, (see the end of Sect.1), we get $12\xi=1.02\sim 1$ and

$$\Delta\theta_0 = \frac{cT}{(2N+1)a}. \quad (43)$$

We claim that the above conclusion represents a general result when the effective spatial width T_e of the radiated waveform is defined according to

$$\int_{-\infty}^{+\infty} dt f^2(t) = T_e f^2(0). \quad (44)$$

We stress the fact that the definition (equation 37) leading to equation (42) is particularly appropriate in the transient regime, because the message is usually encoded in the shape of the radiated signal.

As was mentioned before, the spatial extension of the pulse plays a fundamental role in the definition of far-field: the ratio of the spatial pulsewidth to the range at the point of observation should be small. This is different compared to the sinusoidal signal case, where the wavelength plays the role similar to the spatial pulsewidth. This is exactly what happens also for the effective angular width of the array as is evident by comparing equations 35 and 42. In other words, it seems reasonable that the results in frequency domain for sinusoidal signals may have a

dual counterpart in the case of pulsed excitations in the time domain, when the wavelength is substituted by the effective spatial pulsewidth.

2.6.3. Additional Considerations

Let's discuss some additional considerations associated with the "timed" arrays. First of all let us address the ability to steer the array. If identical waveforms are applied to the array elements with a progressive time delay τ , the radiated field exhibits the pattern

$$F(t, \theta) = \sum_1^N f(t + n\tau - n\Delta t), \quad \Delta t = \frac{d}{c} \sin \theta, \quad (45)$$

with its maximum satisfying

$$\frac{d}{c} \sin \theta_m = \tau. \quad (46)$$

As a matter of fact, the radiated waveforms sum up all "coherently" along θ_m . For $\tau=0$ we recover the broadside array; for $\tau=d/c$ we obtain the end-fire array and this is a limiting case. In this case a pulse whose spatial extent is N times the length of a single pulse at broadside (N being the total number of array elements) is obtained. When $\tau > d/c$ the pulses become dispersed (pulses broaden) in an angular region that, starting from the broadside, becomes wider with increasing τ , and marginal end-fire radiation efficiency is obtained.

"Timed" arrays are not concerned with the grating lobes provided that the radiation waveform does not exhibit any periodicity. If this is not the case, and the waveform repeats itself after a time T_p such that $cT_p < d$, then the grating lobes appear at angles satisfying

$$\frac{d}{c} \sin \theta_p = T_p. \quad (47)$$

Equation (47) implies that for reasonable values of d the grating lobes will exist at extremely high PRFs (GHz), which are not practical.

Finally, in order to assess the effect of tapering on the array's effective radiation lobe $\Delta\theta_0$, we present a “numerical” experiment, which suggests that tapering, from the center of the array to the edges has the effect of broadening of $\Delta\theta_0$, while the tapering from the array's edges inward towards the center has focusing effect. From the results presented in Sec.2-2, it follows that

$$\Delta\theta_0 \sim \frac{F^2(0)}{\sum_{n=1}^N [F(t,0) - F_n(t,\theta_0)]^2}, \quad (48)$$

where $(2N+1)$ is the number of array elements.

In the case of uniform excitation and $N=2$ (five radiating elements), see figures 9 and 10, we have

$$F^2(t,0) = 25, \quad \sum_{n=1}^N [F(t,0) - F_n(t,\theta_0)]^2 = 4(1+4) = 20 \quad (49)$$

and

$$\Delta\theta_0 \sim 1.25 \quad (50)$$

For a linear tapering toward the edges of the array we get

$$F^2(t,0) = \left(1 + 2\frac{1}{2} + 2\frac{1}{4}\right)^2 = \frac{25}{4}$$

$$\sum_{n=1}^N [F(t,0) - F_n(t,\theta_0)]^2 = 2\left(\frac{1}{16} + \frac{9}{16} + \frac{9}{16} + \frac{1}{16}\right) = \frac{5}{2} \quad (51)$$

and

$$\Delta\theta_0 \sim 2.5 \quad (52)$$

which shows a substantial increase (broadening) compared to the uniform excitation case.

When the tapering is still linear, but is in the direction towards the array's center (inverse tapering), we get

$$F^2(t,0) = [2(1) + 2(\frac{1}{2}) + (\frac{1}{4})]^2 = \frac{169}{16}$$

$$\sum_{n=1}^N [F(t,0) - F_n(t,\theta_0)]^2 = 2(\frac{16}{16} + \frac{36}{16} + \frac{36}{16} + \frac{16}{16}) = 13 \quad (53)$$

yielding

$$\Delta\theta_0 \sim 0.81 \quad (54)$$

The obtained result means focusing effect when array taper is applied from the edges inward toward its center. More analyses are needed to fully assess the effect of tapering.

3. EXPERIMENTAL SETUP AND EQUIPMENT

3.1 Pulsar

Antennas were driven by the signal from a 2.5kV solid-state pulser, manufactured by Grant Applied Physics in California. The output signal from the pulser resembles a step function with rise time $t_{10-90} \sim 169$ ps (measured) and $t_{mr} \sim V_{peak} / \dot{V}_{peak} = 2500 / (1.18 \times 10^{13}) = 211$ ps. The measured voltage profile during the first 700 ps only is depicted in figure 12 (top).

3.2 Source Voltage Characteristics

In order to predict the performance of the array system and to compare it to the measured results, the source voltage was modeled using the following analytic expression:

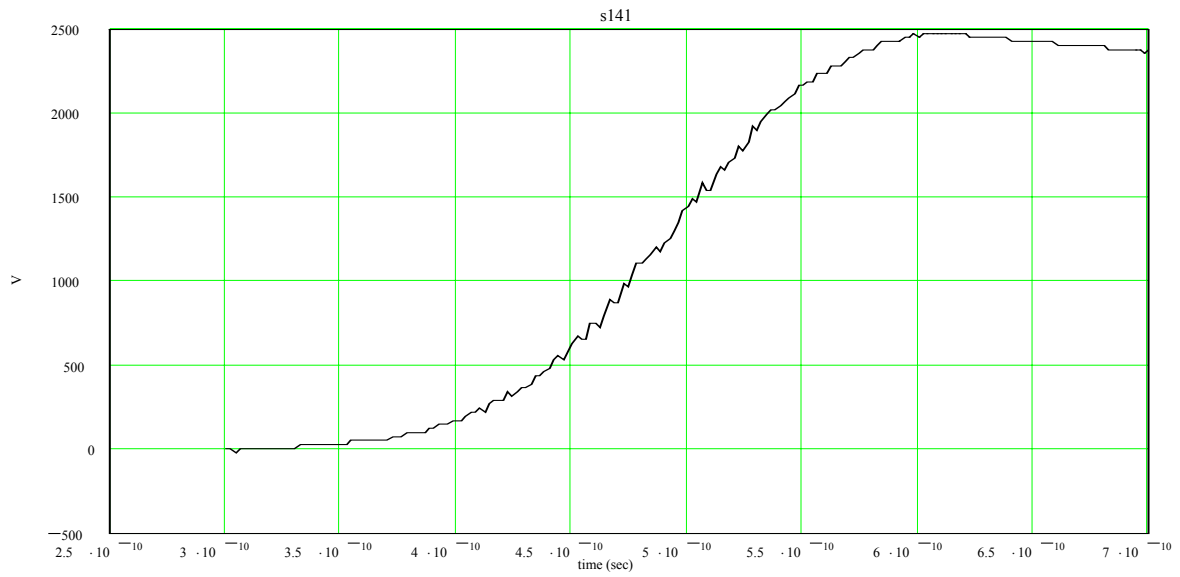
$$v(t) = [v_n(a, t) + v_p(a, t)](1 + \varepsilon) + v_d(t), \quad (55)$$

where,

$$\begin{aligned} v_n(a, t) &= 0.5v_0 \Phi(-t) \exp(-a \frac{t}{t_d}) [1 - \operatorname{erf}(-\sqrt{\pi} \frac{t}{t_d})], \\ v_p(a, t) &= v_0 \Phi(t) \exp(-a \frac{t}{t_d}) [1 - 0.5(\operatorname{erf}(-\sqrt{\pi} \frac{t}{t_d}))], \text{ and} \\ v_d(t) &= v_0 \{ \exp[-\frac{(t - 5 \times 10^{-9})}{b}] - 1 \} \Phi(t - 5 \times 10^{-9}) \end{aligned} \quad (56)$$

where $V_o=2500$ Volts, is the peak value of transient voltage applied to the antenna, $a=0.33$, $\varepsilon = 0.001$, $b = 10 \times 10^{-9}$, and $t_d = 220 \times 10^{-12}$, and $\Phi(t)$ is the Heaviside step function. Figure 12 presents side-by-side measured and modeled rise-time portion of the source voltage profiles.

HYPS Pulsar ~169 ns rise time (flipped)
Antenna drive signal
.78 ns RG214
Barth Six Way Splitter
5:1, 10:1, 10:1



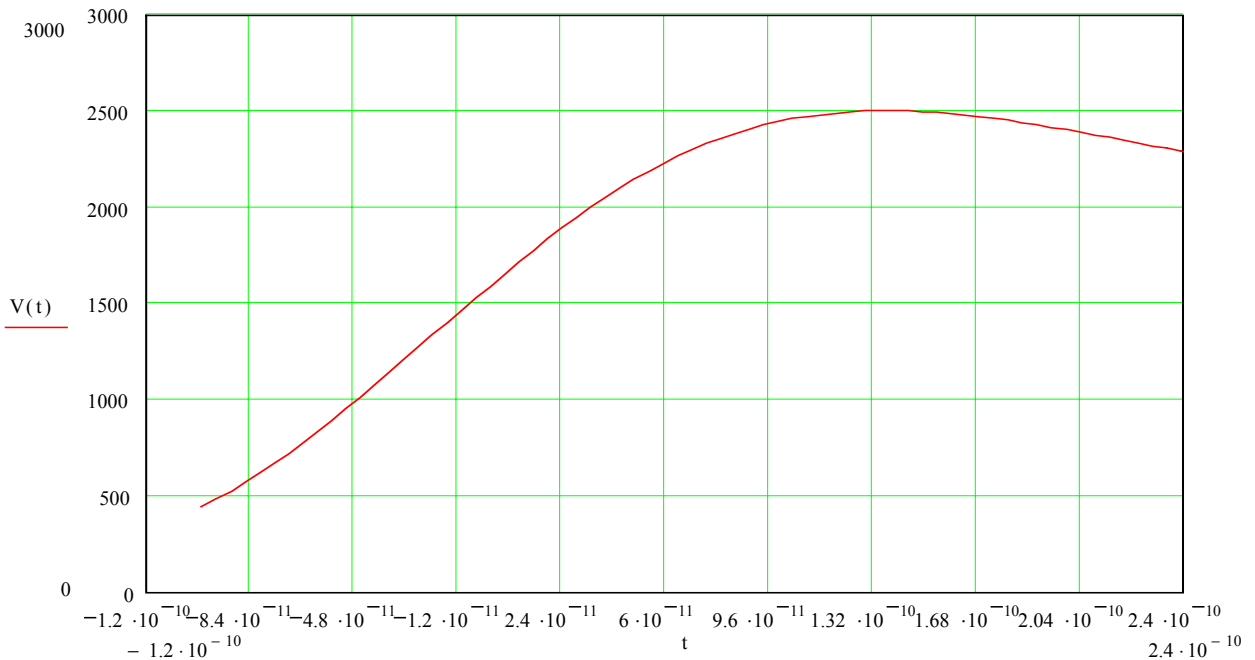


Figure 12. Measured (top) and modeled (bottom) rise portion of the source voltage

3.3 Ground Plane B-dot Sensor

MODEL B-80

The PROLYN Model B-80 Sensor is a B-Dot loop equivalent to the AFWL MODEL MGL-8. This sensor is the smallest of the B-Dot series of sensors developed by the Air Force Weapons Laboratory. Although this sensor was designed for use in a laboratory environment, it has been upgraded to include a weather cover for some protection. The sensor can be used as a B-Dot sensor, or it can be used to measure the time rate-of-change of surface current density since the magnetic field over a conductive sheet is related to surface current density. The sensor consists of a half-cylinder loop on a base plate that when mounted to a conducting surface produces a voltage output in response to a time variant B field. The B-80 is basically identical to the Model B-S80. The B-80 version has the connector located below the ground plate while the B-S80 has the connector located on top of the ground plate.

This sensor has a parallel-series wiring configuration that cancels the electric field induced signals and makes the sensor's output signal the result of only the magnetic field. The equation pertinent to this device is:

$$V_s = A_{eq} \frac{dB}{dt} \tag{57}$$

where A_{eq} = sensor equivalent area (m^2) and B = magnetic flux density vector (teslas).

This sensor is a passive device; therefore, an external power source is not required. The sensor output is a radial configuration, Model B-80(R).

ELECTRICAL SPECIFICATIONS

- Equivalent Area (A_{eq}) $1 \times 10^{-5} m^2$
- Frequency Response (3 db point) $\approx 7.5 GHz$
- Risetime (t_r 10-90) $\approx 0.045 ns$
- Maximum Output (peak) $\pm 100v$
- Output Connector Female SSMA

PHYSICAL SPECIFICATIONS

Mass: 15 grams

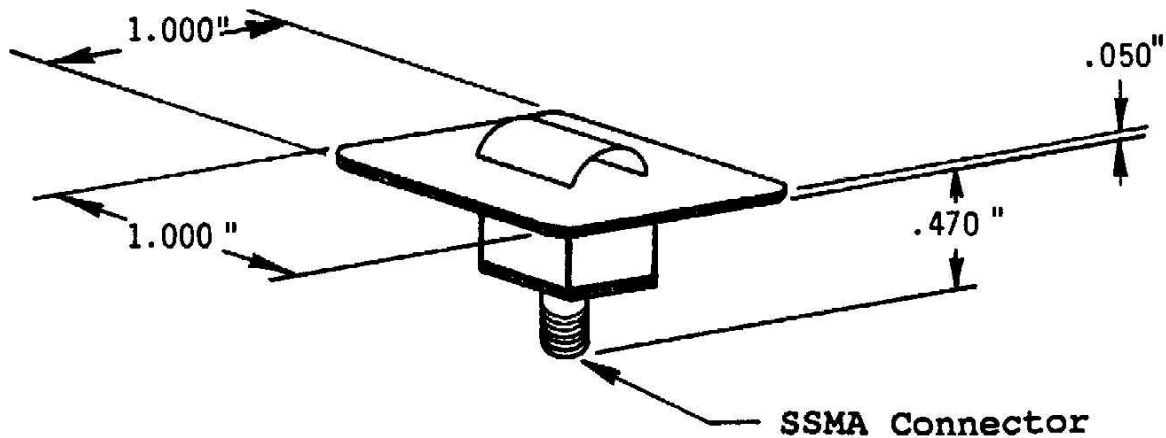


Figure 13. Prodyn Model B-80 ® ground plane B-dot sensor

3.4 Experimental Setup

All experiments were carried out in a 45'x 35" room. Three TEM horn radiators were placed on top of a 24'x12' table covered completely by a metal sheet to simulate a ground plane (see figure 14). Two sets of holes, one along the OQ axis (boresight direction) and the other along the OP axis (26.57° off the boresight), were drilled for placing B -dot sensors (denoted by the red ovals) right at surface of the ground plane, where the rates of change of magnetic field

$(\partial B/\partial t)$ were measured. Furthermore, extra B-dot sensors were placed along the PQ arc (arc between P and Q . axis, 300 cm away from the center of the central horn) to perform the measurements of the field as the function of the angle θ off the boresight axis OQ . Appendix A contains photographs depicting various details/features associated with the experimental setup (see Figures A-1 through A-12).

Geometry of individual TEM horn along with its radiometric and geometric parameters is presented in figure 15.

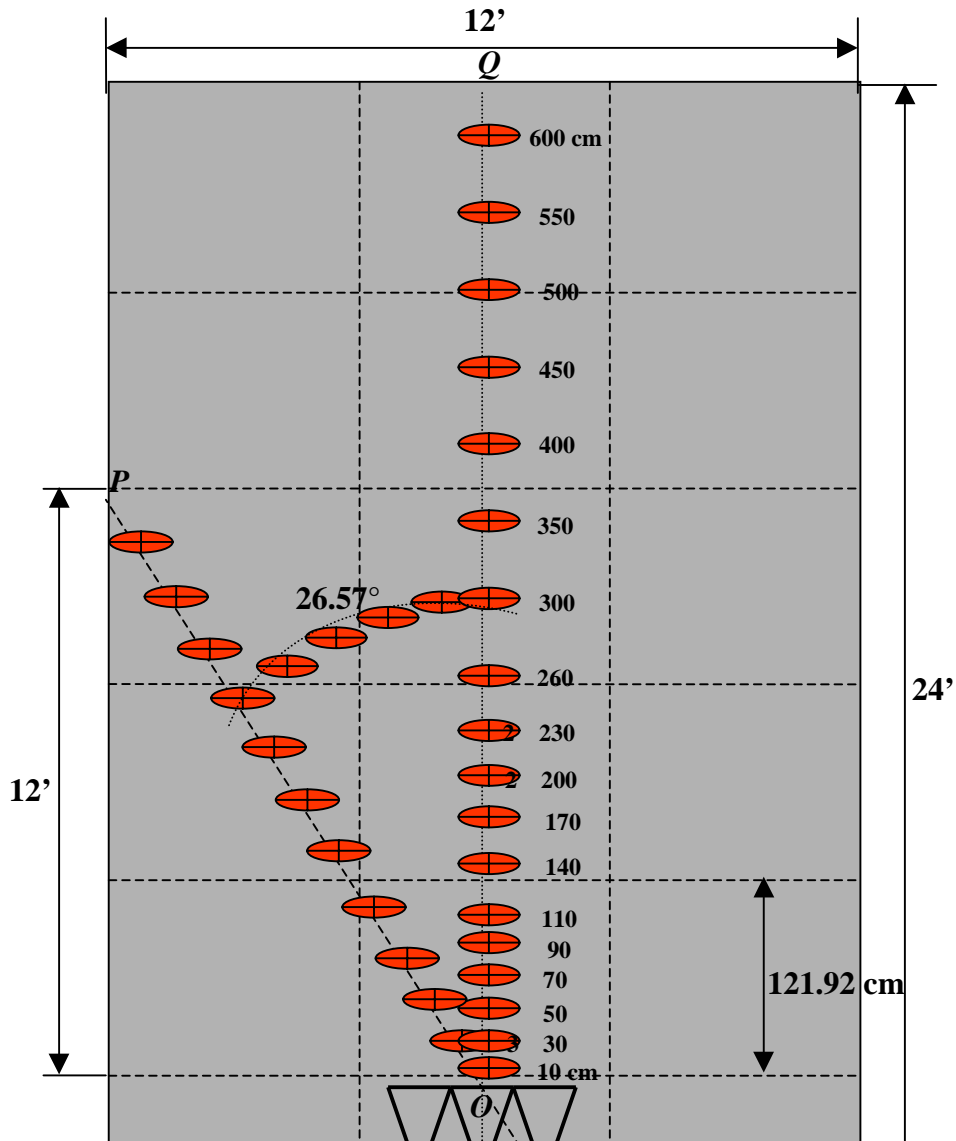


Figure 14. Geometry of the experimental setup

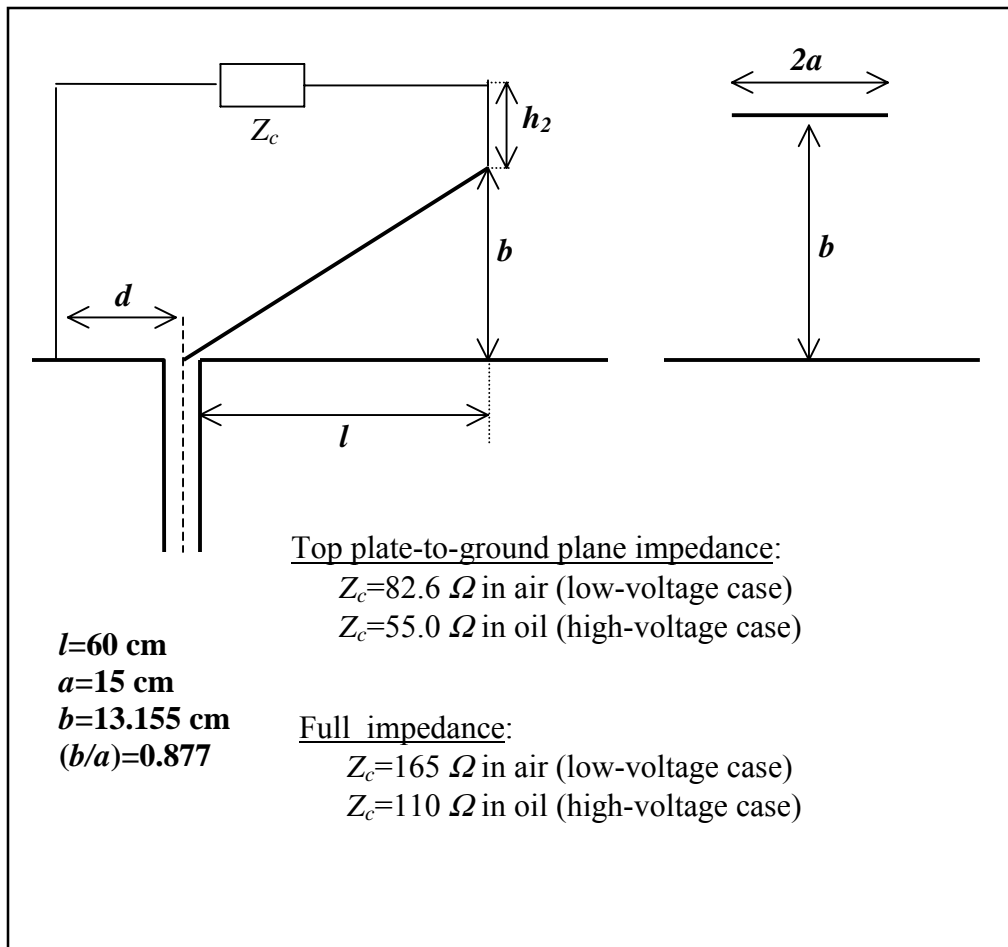


Figure 15. TEM horn geometry.

Parameters h_2 and d were varied during the measurements; their typical values were $h_2=5$ cm and $d=20$ cm. The low-voltage case utilized 2.5 kV pulser, while the high-voltage case used 300 kV pulser and the entire horn was fully submerged in oil to avoid high-voltage arcing and breakdown. Since the low-voltage source used 50- Ω cable, the mismatch with the horn impedance implied that the reflection coefficient is

$$\rho_a = \frac{82.6\Omega - 50\Omega}{82.6\Omega + 50\Omega} = 0.24 \quad (58)$$

resulting in 24% voltage increase from 2.5 kV to 3.1 kV.

Conversion of Measured $\frac{\partial B}{\partial t}$ to Electric Field E : All the measured values of $\frac{\partial B}{\partial t}$ were converted to the values of the electric field using the following method. The value of voltage at the sensor output relates to the value of $\frac{\partial B}{\partial t}$ by:

$$V_s(t) = A_{eq} \frac{\partial B}{\partial t}, \quad (59)$$

where A_{eq} is the sensor's equivalent area. Since the measured voltage, V_m , is proportional to the sensor voltage, V_s , we have,

$$V_m(t) = kA_{eq} \frac{\partial B}{\partial t} = k \frac{A_{eq}}{c} \frac{\partial E}{\partial t}, \quad (60)$$

where k is a constant of proportionality (due to sensor attenuator value), $c=3 \times 10^8$ m/sec is the speed of light in vacuum, and we used the fact that $E=cB$. It follows from equation (60) that,

$$E(t) = \frac{c}{kA_{eq}} \int_0^t V_m(t') dt'. \quad (61)$$

Taking the values $A_{eq}=10^{-5}$ and $k=1$ (no attenuator) it follows that,

$$E(t) = 3 \times 10^{13} \int_0^t V_m(t') dt'. \quad (62)$$

To validate the theoretical models, the measured electric field was compared to the one calculated using a model for the TEM horn-radiated electric field on boresight (see Farr and Baum, 1992)

$$E(r,t) = -\frac{h}{4\pi r c f_g} \left[\frac{dv(t)}{dt} - \frac{c}{2l} \left[v(t) - v\left(t - \frac{2l}{c}\right) \right] \right], \quad (63)$$

where h and l are the height and length of the horn's aperture, respectively, r is the range to the observation point, f_g is the feed impedance normalized to the impedance of free space, and $v(t)$ is the input voltage. Expression given by equation (63) has a convenient form for practical use in computing the radiated electric field along boresight.

4. TERMINATION CONSIDERATIONS

Three different types of load/termination variation were implemented:

1. Low-inductance load
2. Medium-inductance load
3. High-inductance load.

Low-inductance load was realized by using a copper sheet in the path of the termination as seen in figure 16. Medium-inductance load was realized by two chains of resistors stretched apart as seen in figure 17. High inductance load was realized by bringing the two chains of resistors close together as seen in figure 18.



Figure 16. Low-Inductance Load

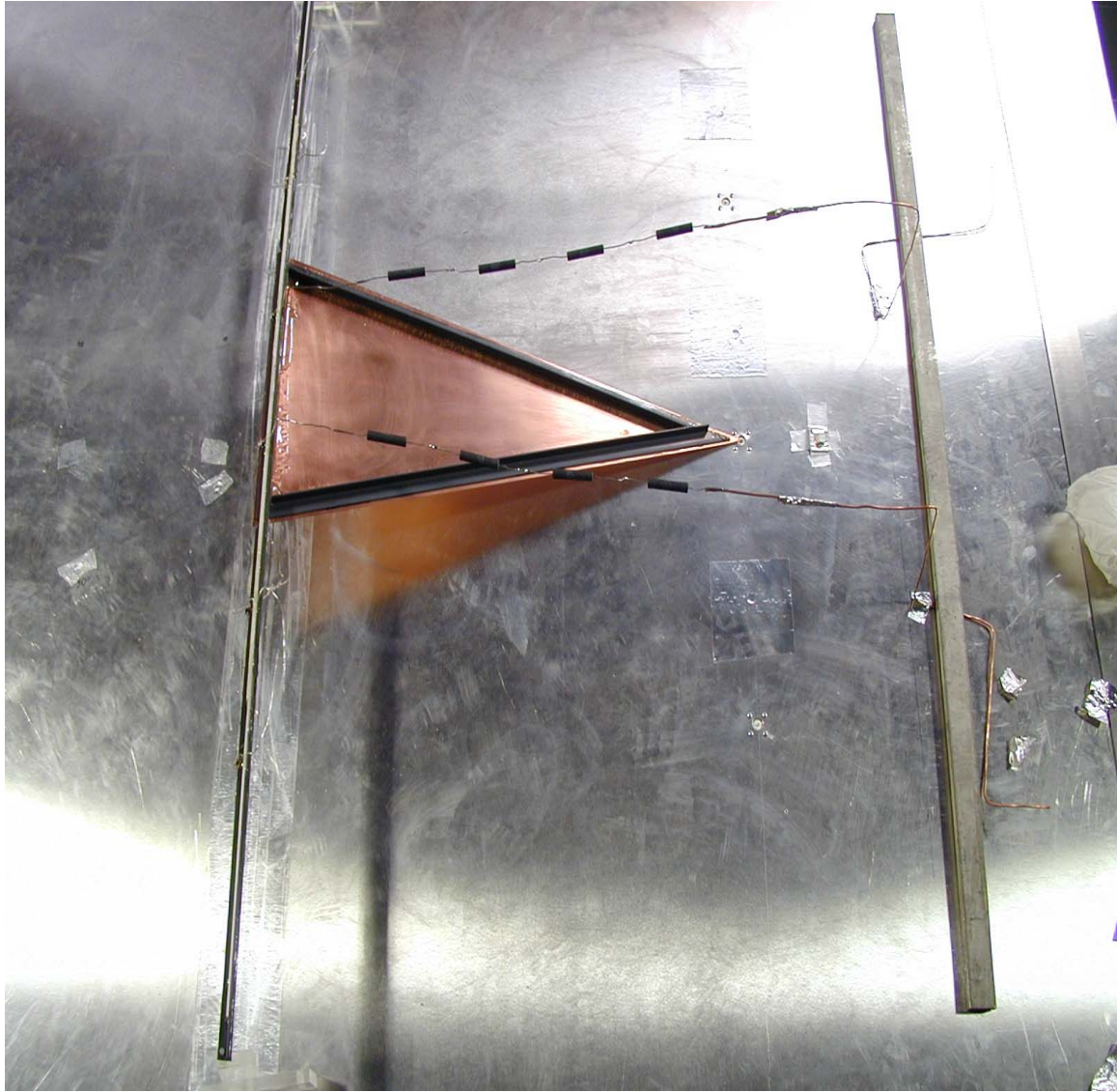


Figure 17. Medium-Inductance Load

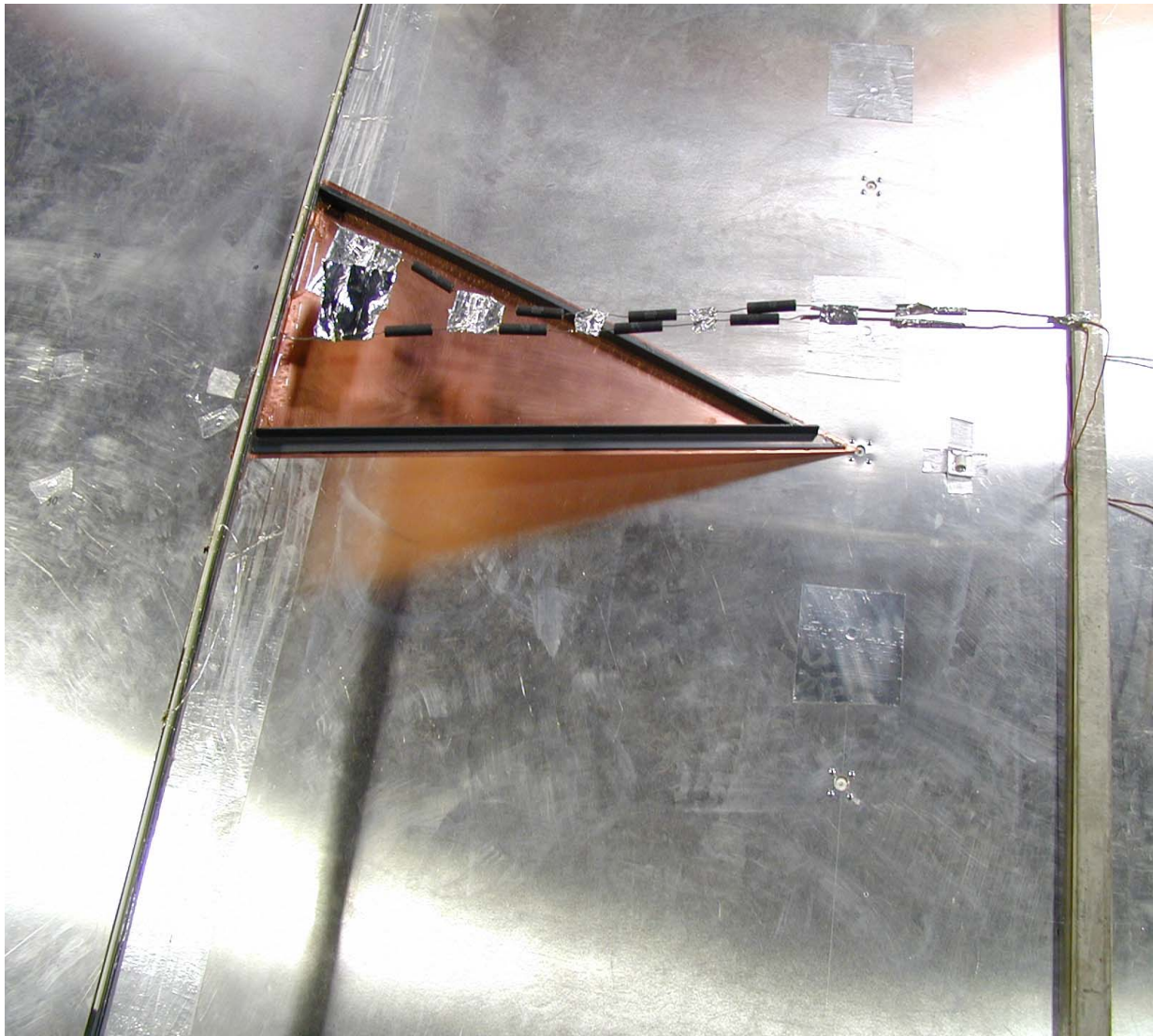


Figure 18. High-Inductance Load.

The electric field measurements associated with the load/termination variations (bias variations) were made at the distance of 70 cm in the direction opposite to OQ , (behind the horn), and the results are shown in Appendix C, Datatakes 142-146.

5. TEM HORN ARRAY STEERING CONSIDERATION

In order to steer the TEM horn array in a particular direction, a progressive true time delays is implemented to adjacent elements, resulting in “tilting” of the wavefront in the direction normal to the desired steering angle. In our experiments, the desired steering angle was 26.5° off the boresight. Using horn #3 as a reference, it can be shown that in this case the excitations of horn #1 and horn #2 should be delayed by $\Delta t_1=447.3$ ps and $\Delta t_2=894.6$ ps respectively. Figure 19 presents the geometry associated with 26.5° three-horn array steering, including the excitation time sequence and respective time delays.

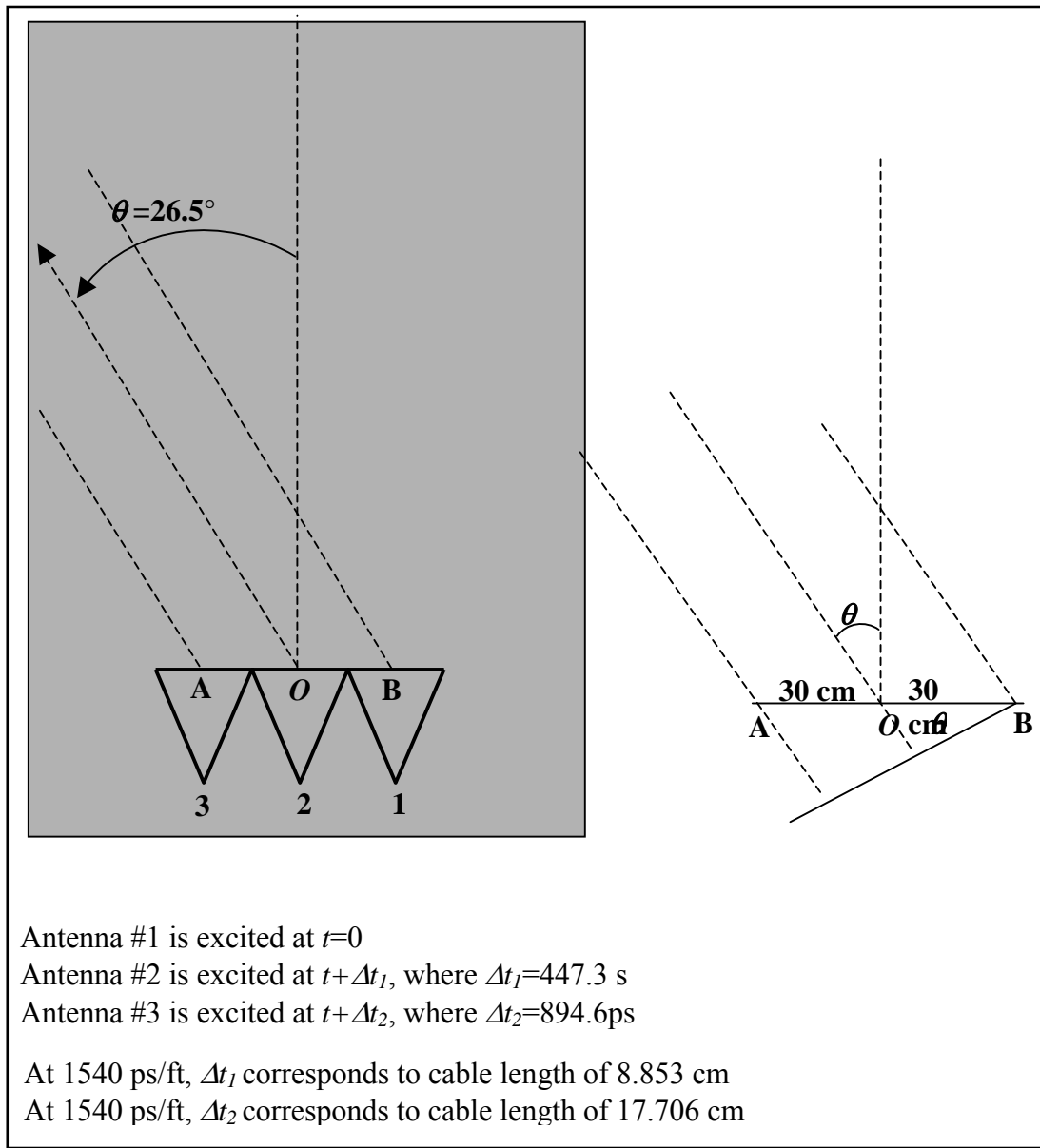


Figure 19. The array steering geometry

6. LOW-VOLTAGE DATA-TAKE MEASUREMENT LOG (SUMMARY)

The total of 146 low-voltage measurements were made during May 2000 and May 2001, including the measurements associated with one-horn excitation. Table 1 shows the entire log of all measurements, including data formatting/location of the points of observation and remarks.

Data-take #	# of antennas	Simultaneous measurements	Time sequence	Data format observ. pt.	Remarks
1-30	3	x		printouts	No waveforms
31-38	3	x		<i>OQ</i> axis	10 cm-600 cm
39-43	3	x		<i>PQ</i> axis	At R=300 cm
44	3	x		<i>OP</i> axis ¹	
45-47	3	x		<i>OQ</i> axis	
48-54	3	x		<i>OP</i> axis	
55-62	3		x	<i>OP</i> axis	10 cm-300 cm
63-71	3		x	<i>arc PQ</i>	R=300 cm
72	2		x	<i>arc PQ</i>	R=300 cm
73	1			<i>arc PQ</i>	R=300 cm
74-90	3		x	<i>OQ</i> axis	30 cm-300 cm
91	3		x	<i>OP</i> axis ¹	R=350 cm
92-106	3	x		<i>OQ</i> axis	10 cm-600 cm
107-113					Cable test
114-116	1			<i>OQ</i> axis ²	Resistor variat.
117-118	1			<i>OQ</i> axis ³	Load / No load
119					Bad data
120-123	1			<i>arc PQ</i>	R=300 cm
124-140	1			<i>OQ</i> axis	Off axis ³
141					Ant feed signal
142-146	1			<i>OQ</i> axis ²	Load variation

¹)350 cm from point O. ²) 70 cm from point O. ³) 300 cm from point O

Table 1. Log of all low-voltage data-takes

Explanations:

Column 1. Column 1 lists datatake numbers. Each datatake corresponds to separate measurement(s).

Column 2. This column shows the number of antennas (TEM horns) energized during the measurements. One implies only one (central) TEM horn was used; two implies two horns (number 1 and 2, see Fig. 3-1) were used, and three implies all three horns were used.

Column 3. The marking (x) of the column indicates that all three horns were energized at the same time implying no time delay between them.

Column 4. The marking (x) of the column indicates a progressive illumination of the horns (sequential excitation of the horns to achieve a desired time delay).

Column 5. The fifth column indicates the axes or arc along which the measurements were made, except for datatakes 1-30, where printouts are available only.

Column 6. The entries of this column show some specific elements (e.g. range(s) at which data was collected, the presence or absence of the resistor load etc., associated with the measurements.

7. LOW-VOLTAGE SIMULTANEOUS MEASUREMENTS

7.1 On Axis

Table 2 presents values of the electric field (E) for wide range of distances (10cm-600cm) measured along the center (OQ) axis in both the one-horn and three-horn configurations, where three antennas were driven simultaneously. For comparison, column three shows the values of E computed using theoretical model (equation 63) which is strictly applicable in the far field.

Simultaneous excitation of three antennas was achieved by using equal length cables connecting antennas to the same pulser, each antenna energized by $2.5 \text{ kV}/3 = 0.833 \text{ kV}$. It is interesting to note that the ratios between three-horn and one-horn fields noticeably increase with distance up to approximately 300 cm, beyond which the ratios appear to level off at about 2.63. The theoretical maximum for this ratio in the far field is 3. The behavior of this ratio is as one would expect.

Distance (cm)	E- Field (V/m)	E-Field(V/m) [Model]	E- Field (V/m)	Ratio (3ant/1ant)
	1 antenna	1 antenna	3 antennas	
10	2925	Model n/a	3735	1.28
30	2070	Model n/a	2910	1.41
50	1548	Model n/a	2385	1.54
70	1206	Model n/a	2130	1.77
90	1002	1125	1980	1.98
110	807	921	1716	2.13
140	687	723	1536	2.24
170	573	596	1368	2.39
200	471	506	1218	2.59
230	428.4	440	1092	2.55
260	384	389	972	2.53
300	344.4	338	898	2.61
350	297.6	289	773	2.60
400	265.2	253	710	2.68
450	231	225	622	2.69
500	200.4	202	576	2.87
550	193.8	184	510	2.63
600	172.2	169	453	2.63

Table 2. The dependence of the electric field (E) on distance with one-horn and three-horn excitations measured boresight along the OQ axis. The last column shows the ratio between the respective values of E .

When the observation point on the OQ axis is very close to the aperture plane, it essentially “sees” horn #2 only. As the point of observation moves along OQ axis away from the aperture plane, the contributions from the other two horns (horn #1 and horn #2) become appreciable, which in turn results in increase of the ratio between electric fields associated with three-horn and one-horn configuration. As the observation point moves further away towards “far zone”, we see saturation of the ratio, because all three horns collectively appear as one point source.

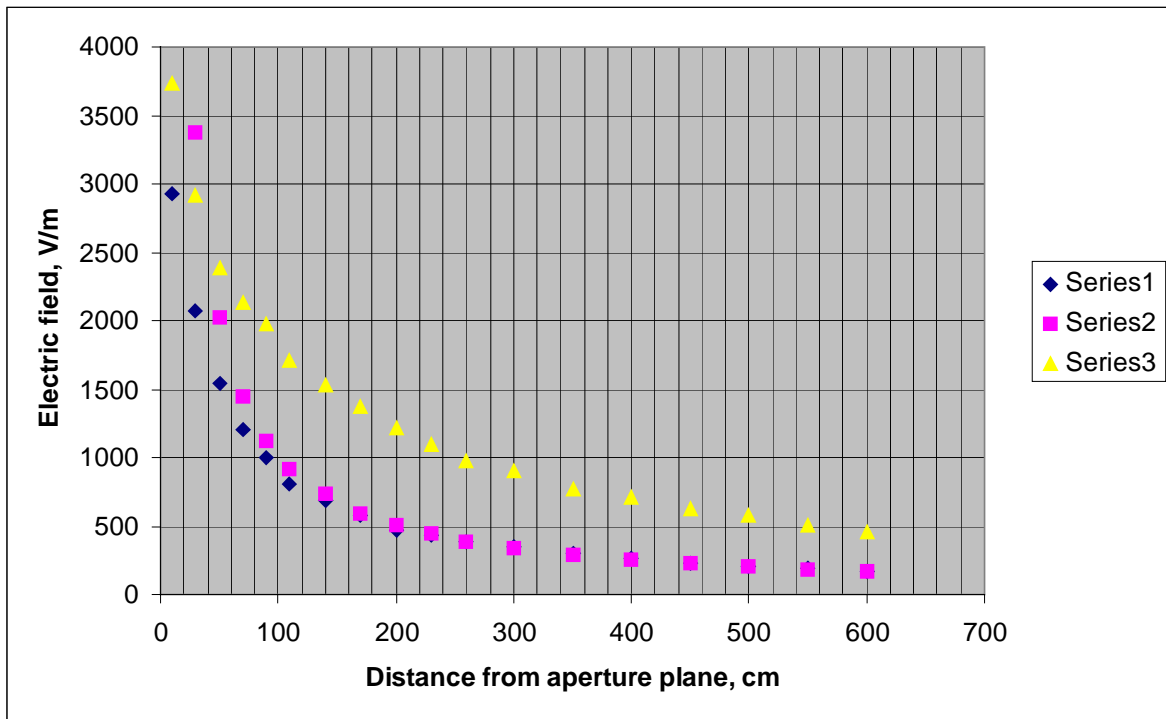


Figure 20. Comparison of electric field due to excitation of one (central) horn (blue marks) vs. excitation of three horns, measured boresight along the OQ axis (yellow marks).

The comparison between the measured (blue marks) and theoretically computed (red marks) electric field along boresight (equation 63) are presented in figure 20, along with the measured electric field along boresight due to simultaneous three-horn excitation (yellow marks). Observe the outstanding agreement between the measured and computed far-field values of E (values coalesce at distances exceeding 150 cm). The values of E shown in Table 2 and figure 20 were obtained using the measured electric field time profiles associated with datatakes 31-38, 45-47, 114-116, 117-118, 124-140 and 142-146 (see Appendix C).

We have also estimated the radiated field on boresight for a single TEM horn at distances of 110cm, 260 cm and 600 cm, using the simple model of equation (63). The corresponding measurements are in data-takes 135, 130 and 129. The comparisons as shown in figures 21, 22 and 23 are seen to be fair for the main pulse. The deviations after the main pulse between the calculations and measurements come from many reasons such as idealizations in the theory and imperfect termination and other scatterings due to objects in the measurement configuration etc.

7.2 Horizontal Radiation Pattern

Figure 24 presents the electric field measurements results associated with excitation of the central horn (horn number 2) only, measured at six distinct points along the PQ arc, 300 cm from the horn. As expected, the maximum electric field ($E_{max}=344.4$ V/m) is measured at the $\theta=0^\circ$, where θ is measured off the boresight direction. The figure implies that the half-power (344.4×0.707) is at 244.4 V/m, which corresponds to approximately $\pm 24^\circ$.

HYPs pulser/TDS820 6GHz sampling scope
 # of Antenna 1
 in phase
 normal resistive bias and shield
 axis o-q
 radius 110 (cm)
 angle (degrees) 0
 Sensor Prodyne Bdot
 Aeff 10^5 m^2

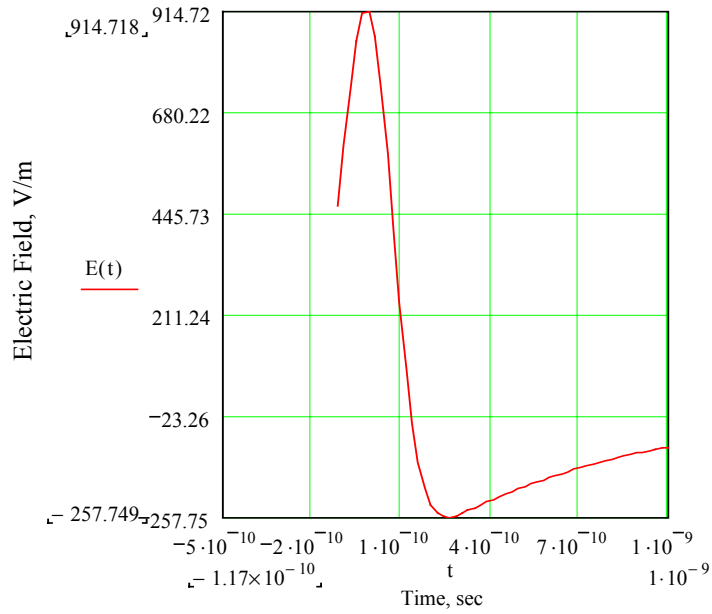
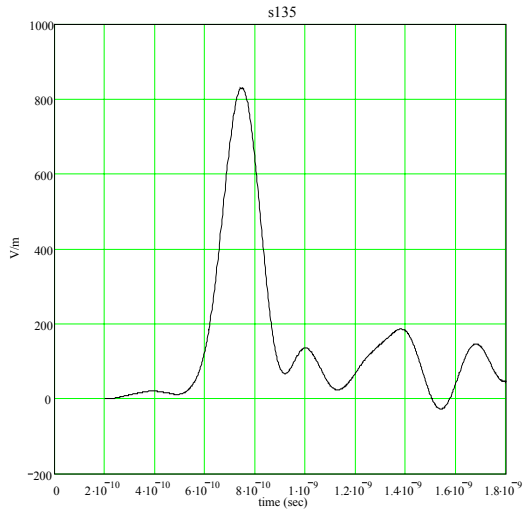


Figure 21. Measured vs. calculated electric field on boresight, $r=110$ cm.

HYPs pulser/TDS820 6GHz sampling scope
 # of Antenna 1
 in phase
 normal resistive bias and shield
 axis o-q
 radius 260 (cm)
 angle (degrees) 0
 Sensor Prodyne Bdot
 Aeff 10^6m^2

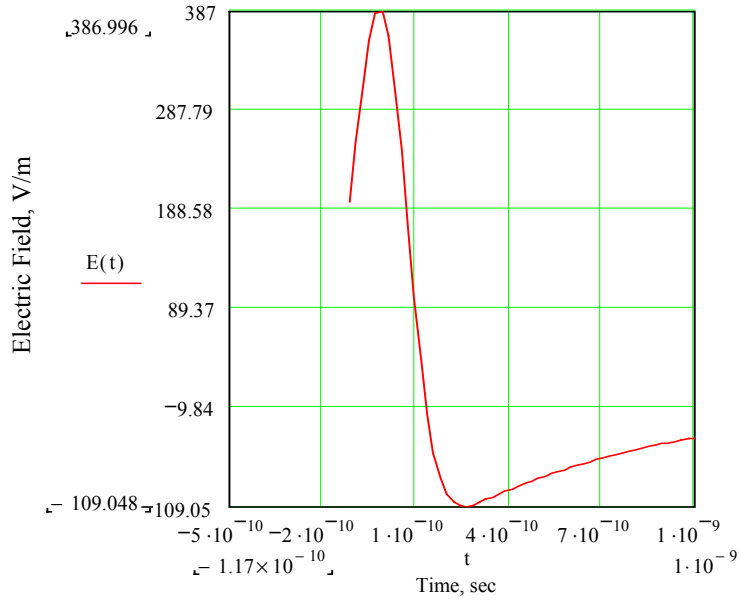
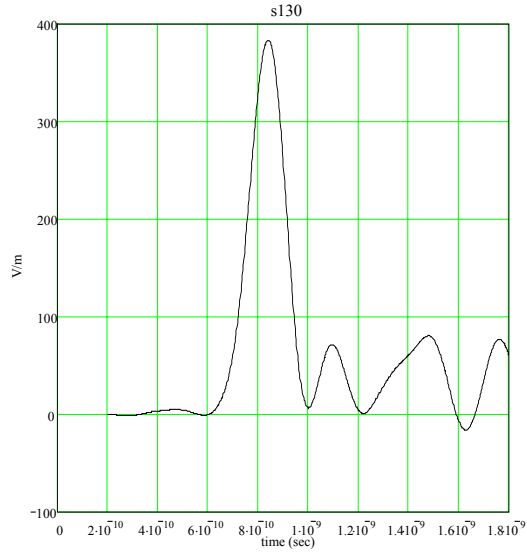


Figure 22. Measured vs. calculated electric field on boresight, $r=260$ cm.

HYPs pulser/TDS820 6GHz sampling scope
 # of Antenna 1
 in phase
 normal resistive bias and shield
 axis o-q
 radius 600 (cm)
 angle (degrees) 0
 Sensor Prodyne Bdot
 Aeff 10^{-5} m^2

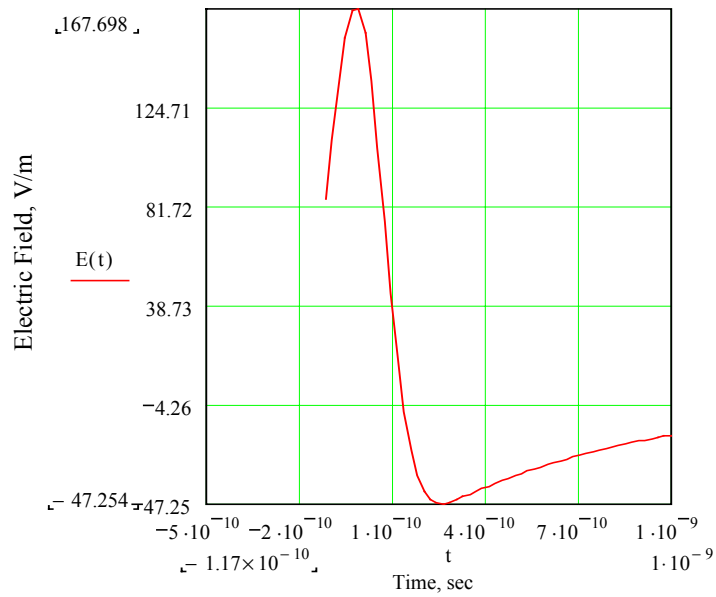
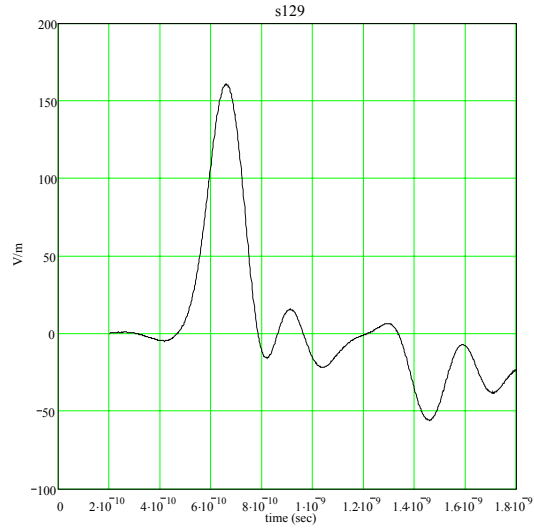


Figure 23. Measured vs. calculated electric field on boresight, $r=600$ cm.

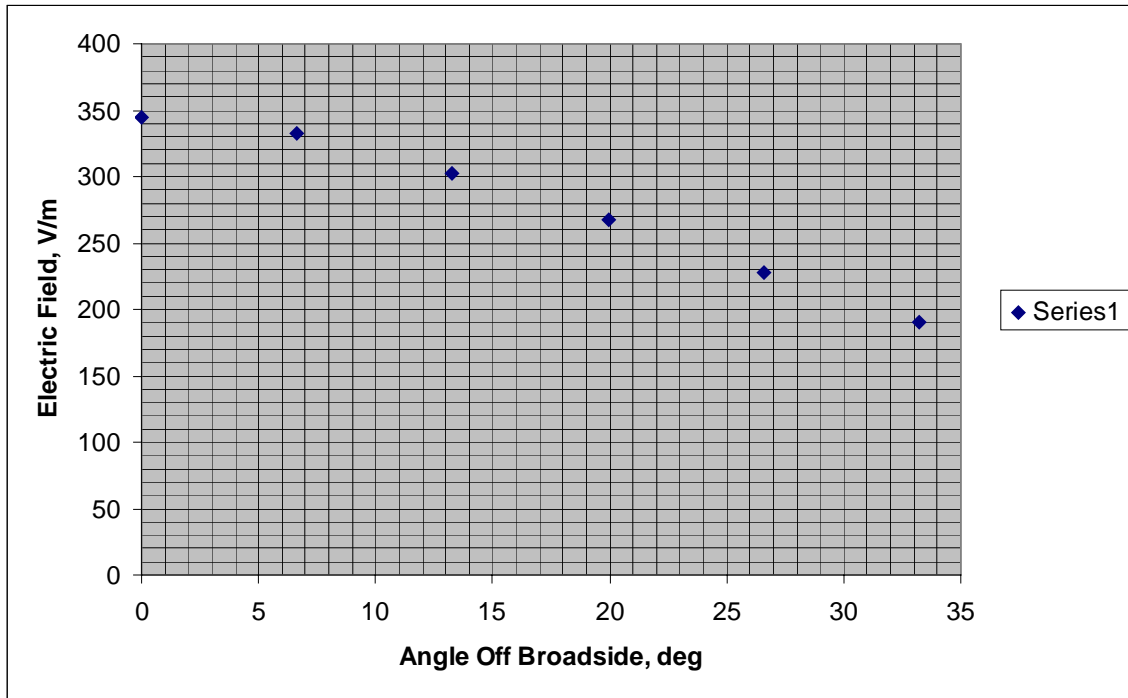


Figure 24. Measured electric field along PQ axis; radiation from a single horn (#2).

All the measured electric field profiles used to generate figure 24 are shown in Appendix C, Datasets 73, and 120-123.

8. LOW-VOLTAGE “TIMED ARRAY” MEASUREMENTS

8.1 On Axis.

The series of measurements (see field profiles in datatakes 74-91, Appendix C) along the OQ axis when the horns are energized with the same time delays as before (namely 447.3 ps and 894.6 ps between horns #1 and #2, and horns #1 and #3), show, as expected, that pulses do not add-up “coherently” with increase of the electric field.

8.2 Horizontal Radiation Pattern.

Figure 25 presents the results of three-horn array E -field measurements along the PQ arc. All horns were driven by the same voltage (833 V), equal a third of pulser output of 2.5 kV. True time delays of 447.3 ps and 894.6 ps between horns #1 and #2, and horns #1 and #3, respectively, were implemented in the horn excitation time sequence to achieve desired 26.57° array beam steering (see figure 19). True time delays were accomplished by adding extra cable length, corresponding to desired time delays.

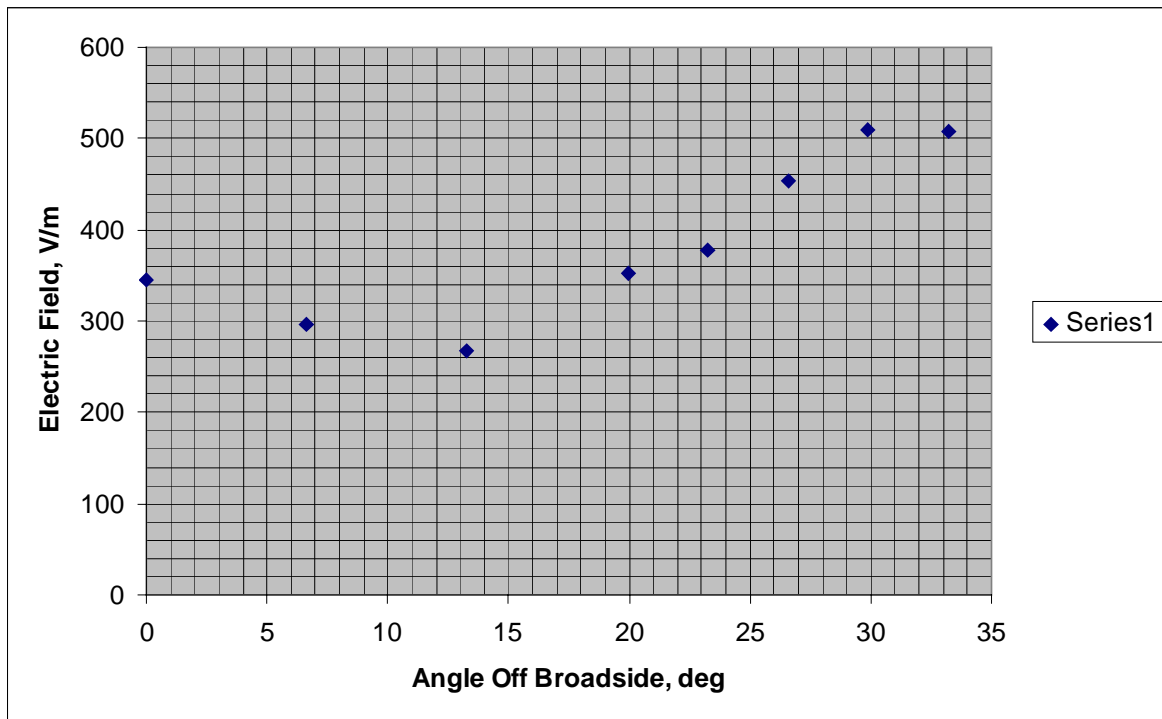


Figure 25. Three TEM horn array steering

Figure 25 shows the peak value for the electric field $E=510$ V/m at $\theta_{\text{peak}}=29.89^\circ$. The desired value of θ_{peak} is 26.57° . We believe that the discrepancy between the measured and theoretical value of θ is due to errors in cable cuts. It should be noted that 1 mm error in cable cut would correspond to 4 ps error in true time delay. All measured electric field profiles associated with radiation pattern in horizontal plane from sequential excitation of the horns are depicted in Appendix A, datatakes 63-71 and 91.

Thus the results of TEM horn steering with impulse-like waveforms closely resemble the steering associated with a narrow-band CW phased array antennas.

9. HIGH-VOLTAGE MEASUREMENTS

A series of limited high-voltage (HV) measurements were carried out to demonstrate the scalability of the low-voltage experiments. In all HV measurements, a single antenna (antenna #2), was placed in an oil bath and it was driven by the 300-kV voltage source (pulser). Schematics of charging/discharging process is shown in figure 26.

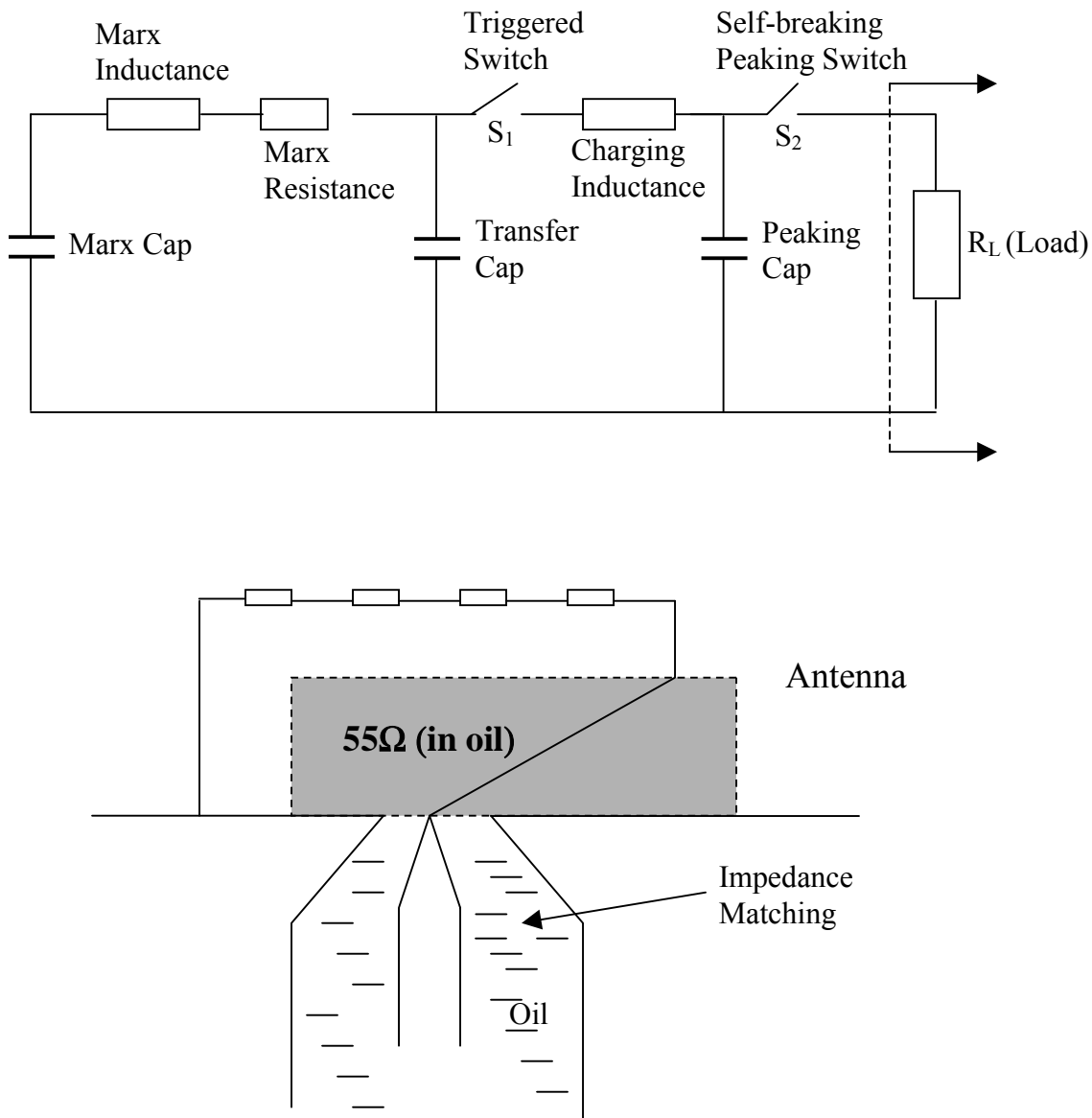


Figure 26. Schematics of high-voltage experimental setup

Acrylic sheets on both sides of the antenna were placed to delay the signals propagating laterally (sideways) towards the point of observation. Acrylic material was used since its dielectric constant matches the dielectric constant of the oil, implying no “media” discontinuity and thus no backscattering.

Figure 27 presents the electric field measurements on boresight (OQ axis) with and without acrylic.

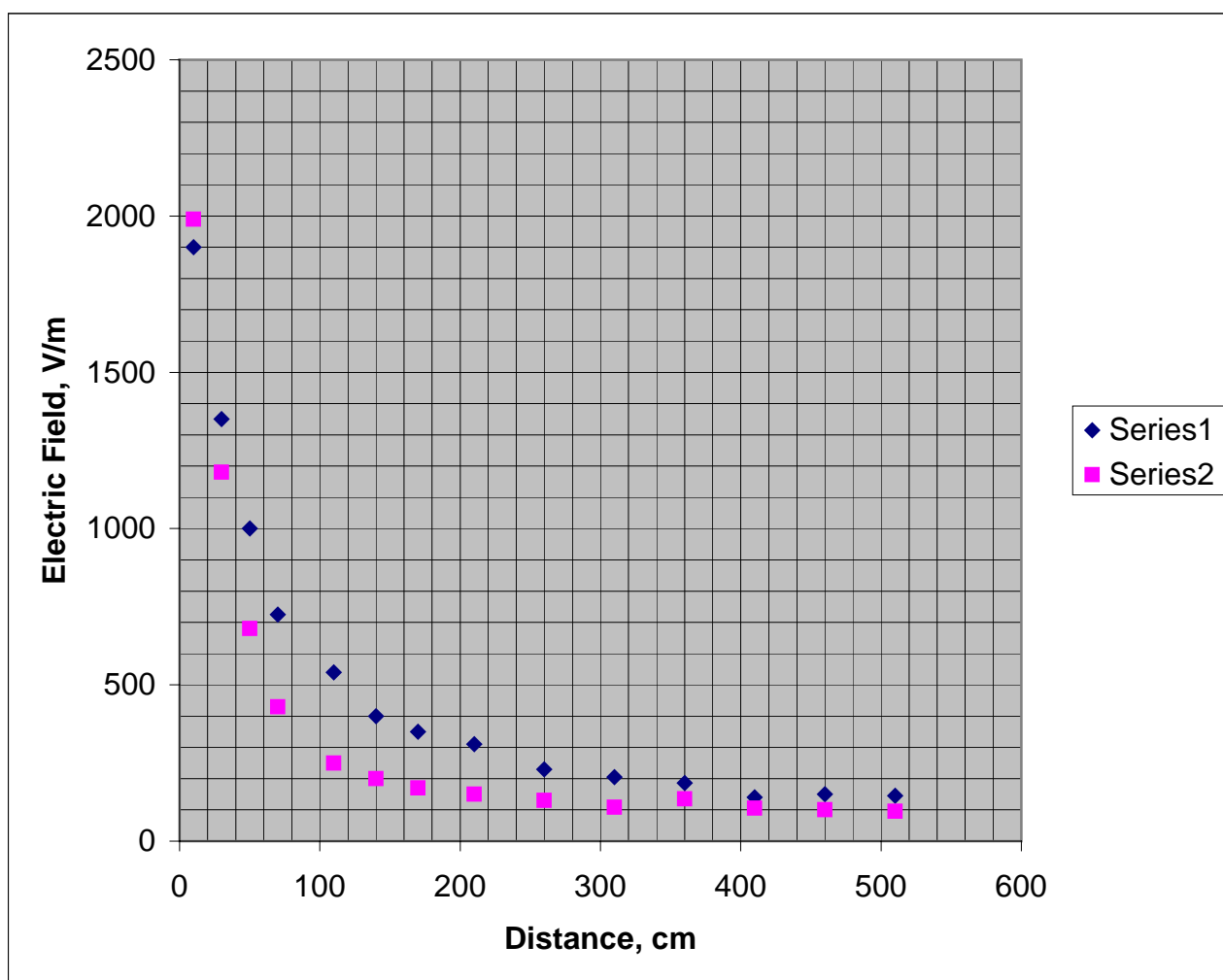


Figure 27. High-voltage experiments. Electric field measurements along OQ axis with (blue marks) and without acrylic.

The measurements with the acrylic (same dielectric constant as the oil) are more reliable than without it.

It must also be noted that 28.5 ns spiral foam-flex cable line was utilized in the signal path, for all these experimental data.

10. SUMMARY

The focus of this study was to experimentally demonstrate the concept of “timed array” antennas. We have worked with three TEM horn elements in a linear array. Single horn performance has been measured in terms of its boresight temporal fields and horizontal radiation patterns. Simple analytical model is used in computing the boresight far fields. We have not made any attempts to optimize the horn design. However, we did study the low – frequency performance of the single horn by varying the termination configurations.

In the context of the 3-element array, we have initially studied the performance of the array when all elements are excited simultaneously. As expected the peak radiation occurs on boresight axis. When suitable true time delays are introduced in the time sequence of excitation, the radiated peak occurs at a certain angle off the boresight. This has been clearly demonstrated. We have not steered the beam in the vertical plane, but only in the horizontal plane. This is a beginning in the area of being able to steer transient arrays. With the advent of triggered switches with ultra-low jitters, this type of beam steering is expected to result in large transient arrays for various applications in the future!

References:

Baum CE, Low-Frequency-Compensated TEM Horn. Sensor and Simulation Notes, Note 377, 28 January 1992.

Farr EG and Baum CE. 1992. A Simple Model of Small-Angle TEM Horn. Sensor and Simulations Notes, Note 340, Phillips Laboratory, Albuquerque, NM, May 1992.

Farr EG. 1992. Simple Models of Antennas Useful in Ultra-Wideband Applications, Transient Radiating Antenna Memos (Memo 2 , NM, July 1992.

Kanda M. 1980. Transients in a Relatively Loaded Linear Antenna Compared with Those in a Conical Antenna and TEM Horn. IEEE Trans. Antennas and Propagation, Vol. AP-28, No.1, January 1980.

Mikheev OV, Podosenov SA et al. 2001. Approximate Calculation Methods for Pulse Radiation of TEM-Horn Array. IEEE Trans. Electromagnetic Compatibility, Vol.43, No.1, 67-74, February 2001.

Vogel MH, 1996. Design of the Low-Frequency Compensation of an Extreme-bandwidth TEM Horn and Lens IRA. Sensor and Simulation Notes, Note 391, 19 April 1996.

Vogel MH, 1996. Intermediate-Frequency Behavior of an Extreme-Bandwidth TEM Horn and Lens IRA. Transient Radiating Antenna Memos. Memo 3, August 1996.

Appendix A.

Details of Experimental Setup.



Figure A-1. Experimental table used as a ground or image plane



Figure A-2. Staircase for an easy access to the surface of the image plane

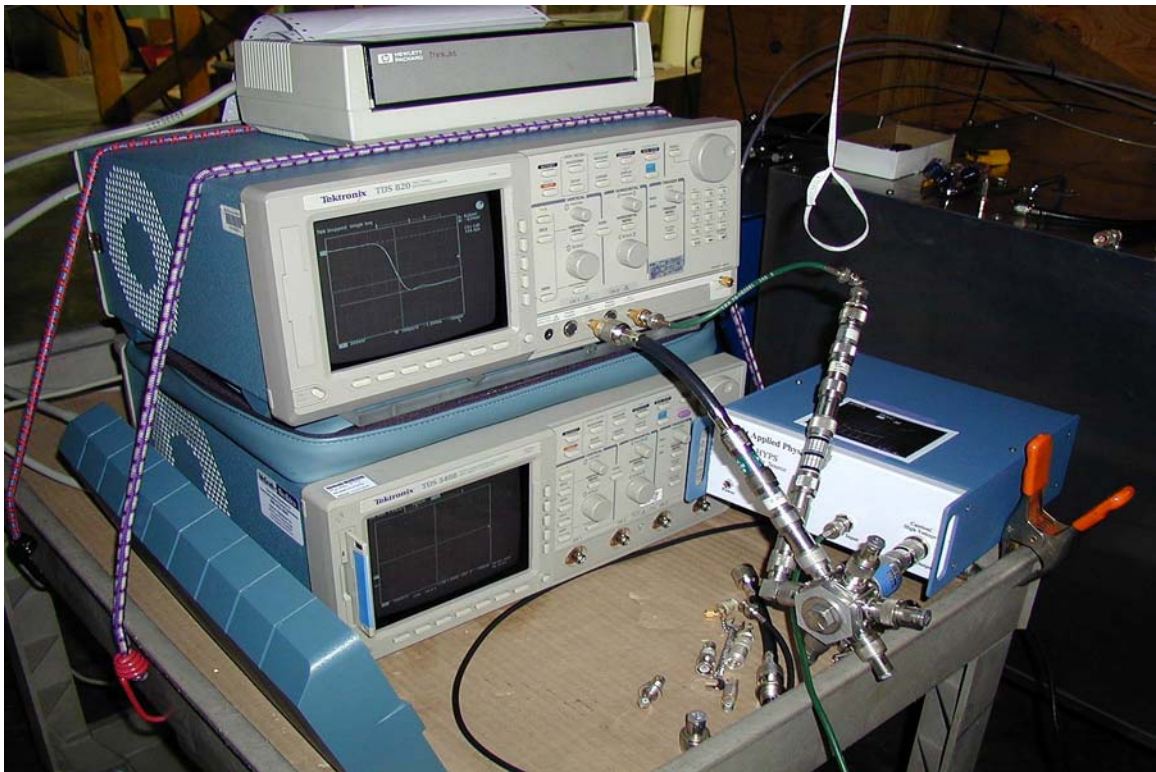


Figure A-3 Techtronics' Sampling Oscilloscope TDS 820.

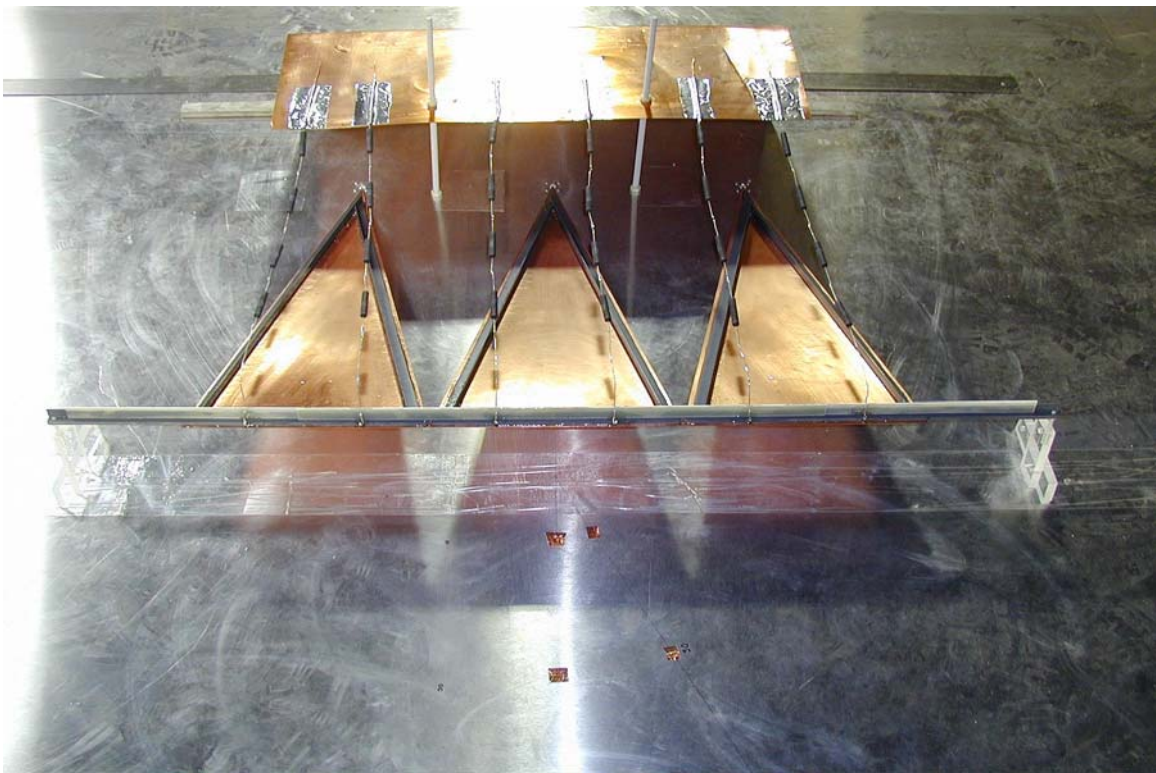


Figure A-4 The geometry associated with three TEM horn array with low-inductance load (front view).



Figure A-5 The geometry associated with three TEM horn array (side view).



Figure A-6. The geometry associated with three TEM horn array with high-inductance load (front view).



Figure A-7. View of apex of the horn.



Figure A-8. The ground plane B-dot sensor

Appendix B

Cable Tests With Tunnel Diode Pulser

Table B-1 presents log of all datatakes associated with cable tests, including cables such as spiral line, RG-223, RG-214, and Foamflex-all of different lengths.

Datatake	Cable length, T_c (ns)	Cable type/connection
113	28.5	Spiral line
112	19.63	RG-223 into TDS 820
111	14	RG-214 into TDS 820
110	6.54	RG-214 into TDS 820
109	55	Foam flex into TDS 820
108	5.15	RG-214 into TDS 820
107		Tunnel Diode Pulser into TDS 820

Table B-1. Cable tests.

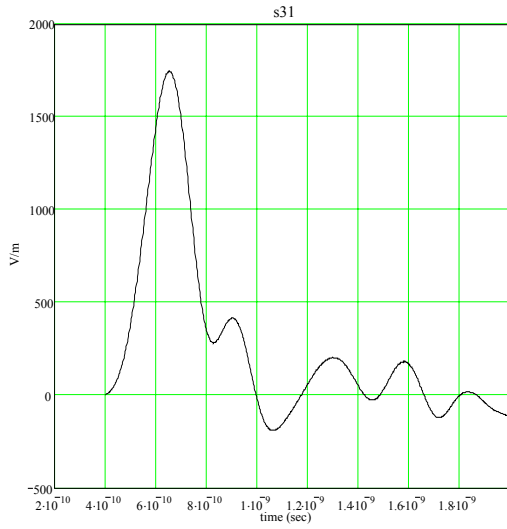
Cable lengths, T_c , are calculated using the following expression:

$$T_c = \frac{l}{v} = \frac{l\sqrt{\epsilon_r}}{c}$$

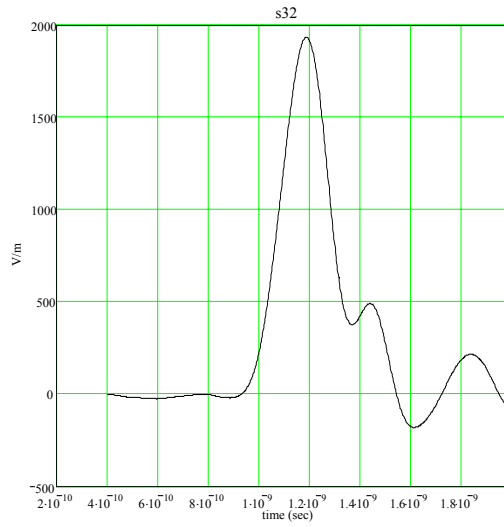
where l and v are the physical length of the cable and speed of light inside the dielectric respectively, ϵ_r is the relative dielectric constant of the cable and c is the speed of light in the vacuum.

Appendix C. Datatakes 31-38.

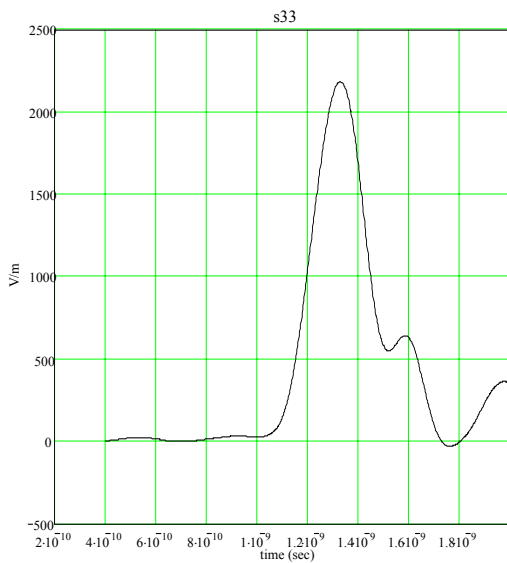
HYPS pulser/TDS820 6GHz sampling scope
 # of Antenna 3
 axis o-q
 radius 110 (cm)
 Sensor Prodyne Bdot
 Aeff 10^5m^2



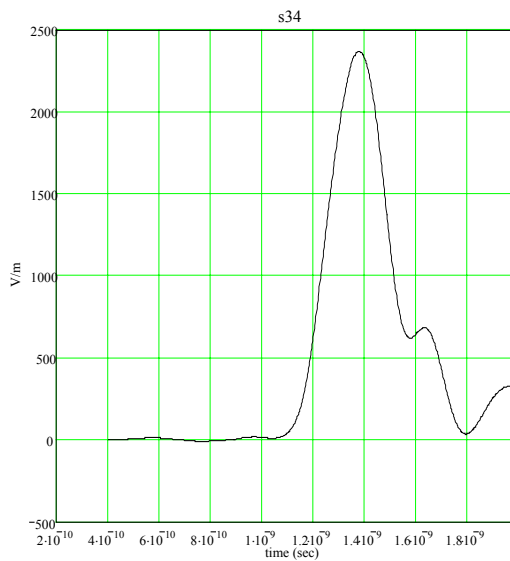
HYPS pulser/TDS820 6GHz sampling scope
 # of Antenna 3
 axis o-q
 radius 90 (cm)
 Sensor Prodyne Bdot
 Aeff 10^5m^2



HYPS pulser/TDS820 6GHz sampling scope
 # of Antenna 3
 axis o-q
 radius 70 (cm)
 Sensor Prodyne Bdot
 Aeff 10^5m^2

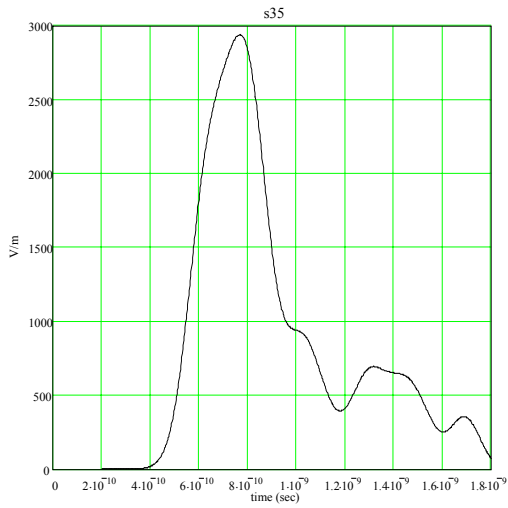


HYPS pulser/TDS820 6GHz sampling scope
 # of Antenna 3
 axis o-q
 radius 50 (cm)
 Sensor Prodyne Bdot
 Aeff 10^5m^2

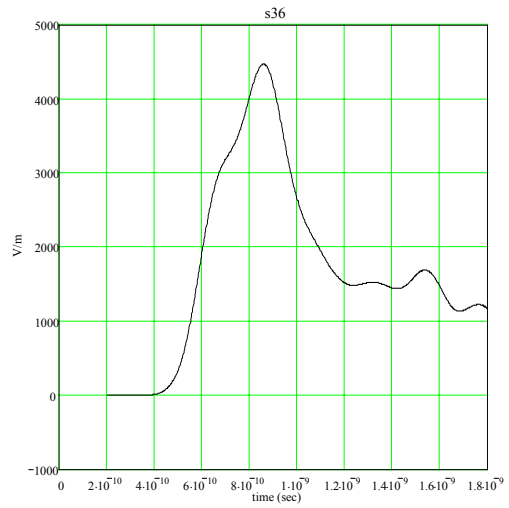


Appendix C. Datatakes 31-38 (Cont.)

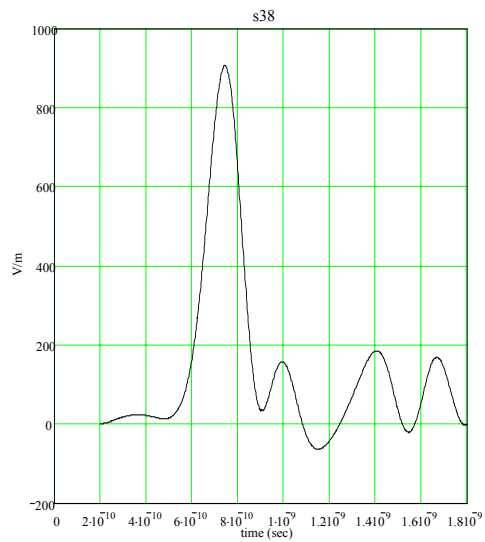
HYPs pulser/TDS820 6GHz sampling scope
 # of Antenna 3
 axis o-q
 radius 30 (cm)
 Sensor Prodyne Bdot
 Aeff 10^{-6}m^2



HYPs pulser/TDS820 6GHz sampling scope
 # of Antenna 3
 axis o-q
 radius 10 (cm)
 Sensor Prodyne Bdot
 Aeff 10^{-5}m^2

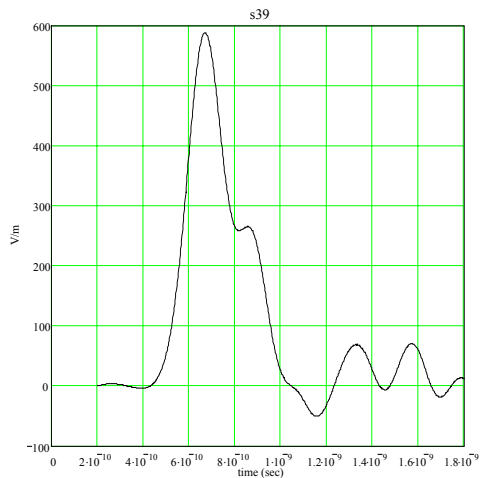


HYPs pulser/TDS820 6GHz sampling scope
 # of Antenna 3
 axis o-q
 radius 300 (cm)
 Sensor Prodyne Bdot
 Aeff 10^5m^2

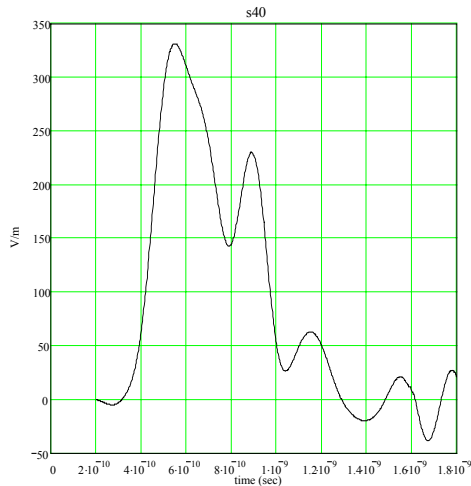


Appendix C. Datatakes 39-43.

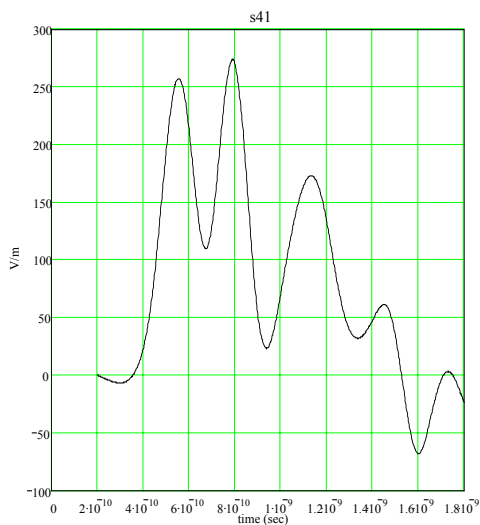
HYPS pulser/TDS820 6GHz sampling scope
 # of Antenna 3
 axis p-q
 radius 300 (cm)
 angle (degrees) 6.64
 Sensor Prodyne Bdot
 Aeff $10^5 m^2$



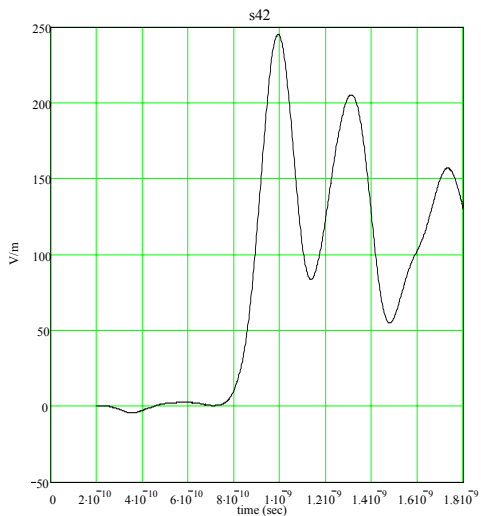
HYPS pulser/TDS820 6GHz sampling scope
 # of Antenna 3
 axis p-q
 radius 300 (cm)
 angle (degrees) 13.285
 Sensor Prodyne Bdot
 Aeff $10^5 m^2$



HYPS pulser/TDS820 6GHz sampling scope
 # of Antenna 3
 axis p-q
 radius 300 (cm)
 angle (degrees) 19.92
 Sensor Prodyne Bdot
 Aeff $10^5 m^2$

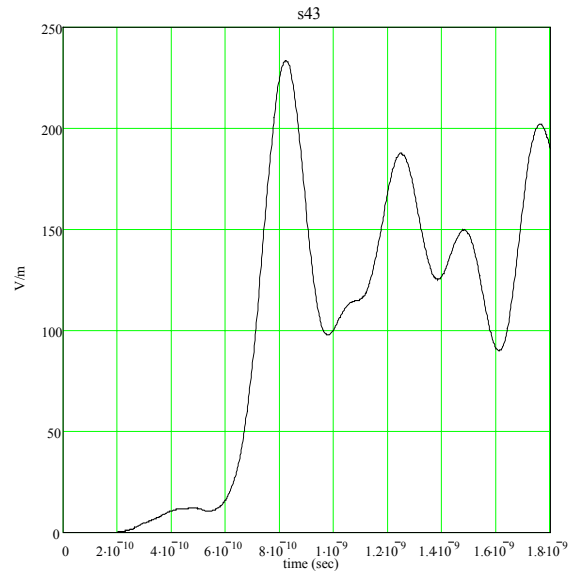


HYPS pulser/TDS820 6GHz sampling scope
 # of Antenna 3
 axis p-q
 radius 300 (cm)
 angle (degrees) 26.57
 Sensor Prodyne Bdot
 Aeff $10^5 m^2$



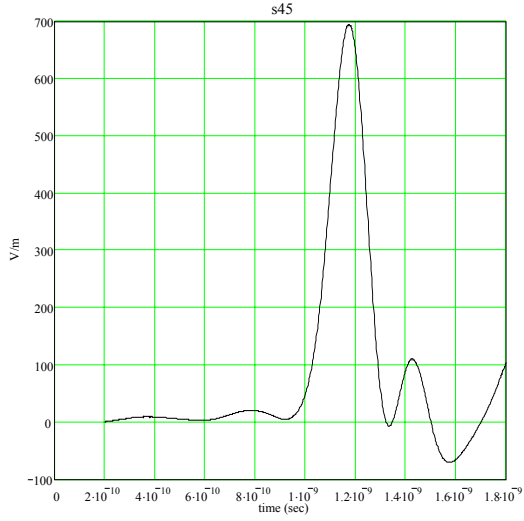
Appendix C. Datatakes 39-43 (Cont.)

HYPS pulser/TDS820 6GHz sampling scope
of Antenna 3
axis p-q
radius 300 (cm)
angle (degrees) 33.21
Sensor Prodyne Bdot
Aeff 10^{-6}m^2

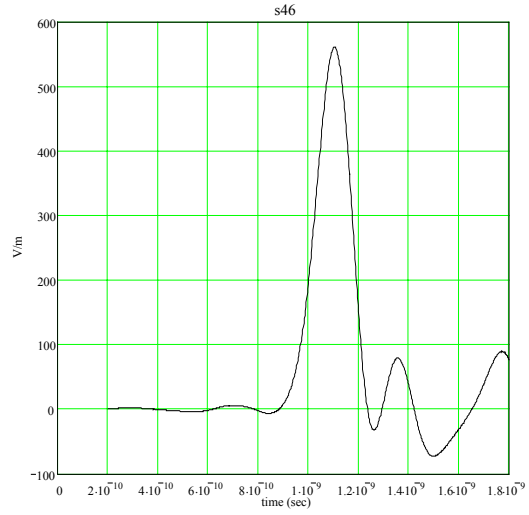


Appendix C. Datatakes 45-47.

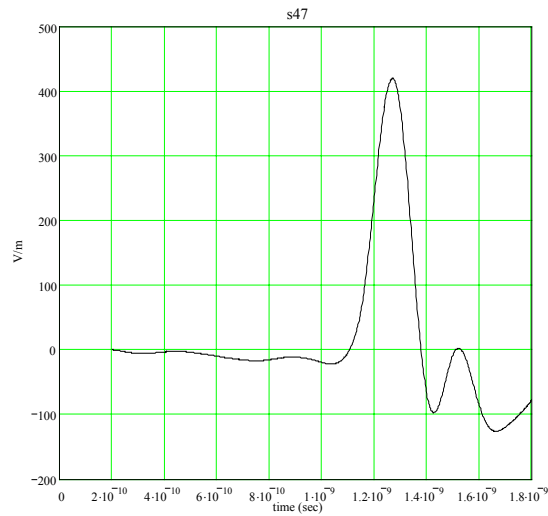
HYPS pulser/TDS820 6GHz sampling scope
 # of Antenna 3
 axis o-q
 radius 400 (cm)
 angle (degrees) 0
 Sensor Prodyne Bdot
 Aeff 10^{-5}m^2



HYPS pulser/TDS820 6GHz sampling scope
 # of Antenna 3
 axis o-q
 radius 500 (cm)
 angle (degrees) 0
 Sensor Prodyne Bdot
 Aeff 10^{-5}m^2

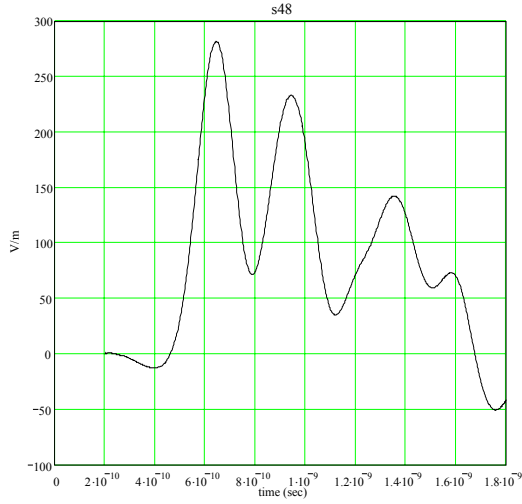


HYPS pulser/TDS820 6GHz sampling scope
 # of Antenna 3
 axis o-q
 radius 600 (cm)
 angle (degrees) 0
 Sensor Prodyne Bdot
 Aeff 10^{-5}m^2

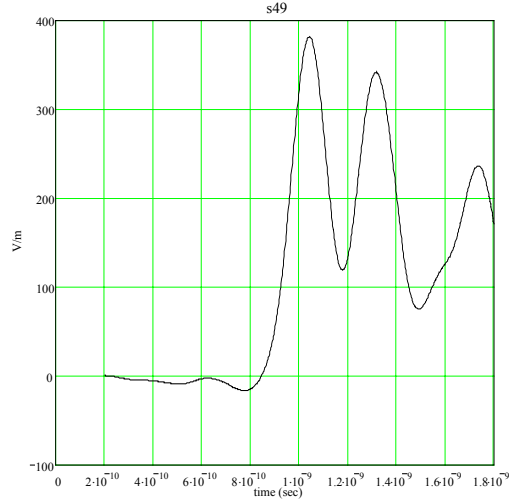


Appendix C. Datatakes 48-54.

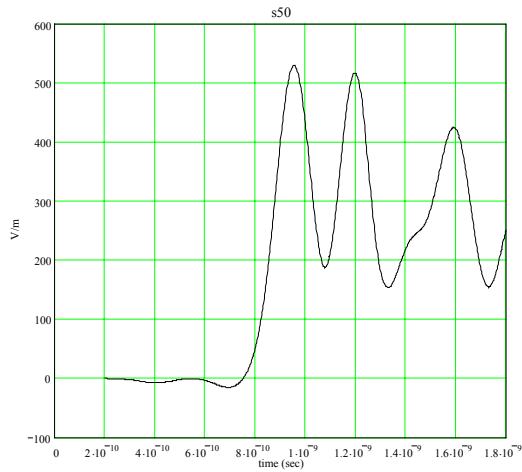
HYPS pulser/TDS820 6GHz sampling scope
 # of Antenna 3
 axis o-p
 radius 250 (cm)
 angle (degrees) 0
 Sensor Prodyne Bdot
 Aeff 10^{-5} m^2



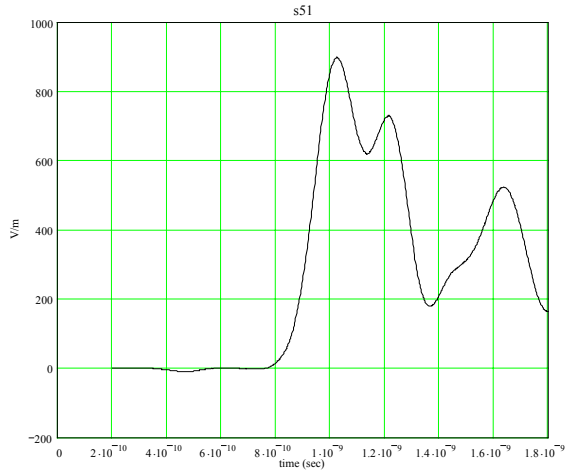
HYPS pulser/TDS820 6GHz sampling scope
 # of Antenna 3
 axis o-p
 radius 200 (cm)
 angle (degrees) 0
 Sensor Prodyne Bdot
 Aeff 10^{-5} m^2



HYPS pulser/TDS820 6GHz sampling scope
 # of Antenna 3
 axis o-p
 radius 150 (cm)
 angle (degrees) 0
 Sensor Prodyne Bdot
 Aeff 10^{-5} m^2

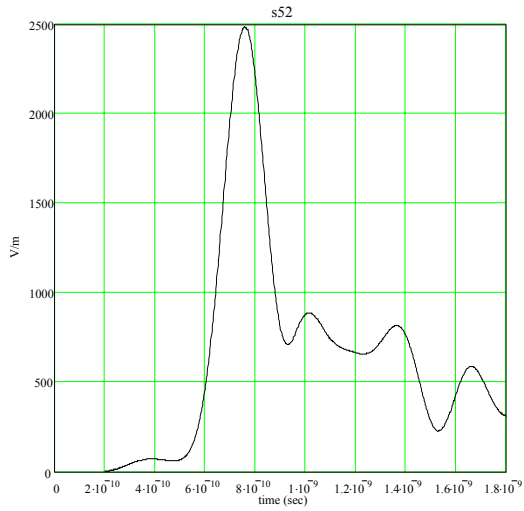


HYPS pulser/TDS820 6GHz sampling scope
 # of Antenna 3
 axis o-p
 radius 100 (cm)
 angle (degrees) 0
 Sensor Prodyne Bdot
 Aeff 10^{-5} m^2

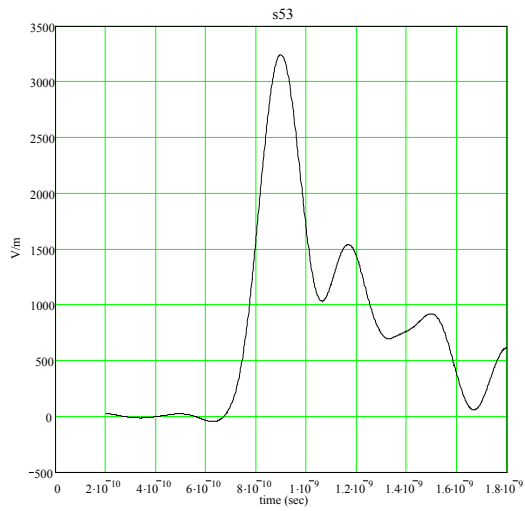


Appendix C. Datatakes 48-54 (Cont.)

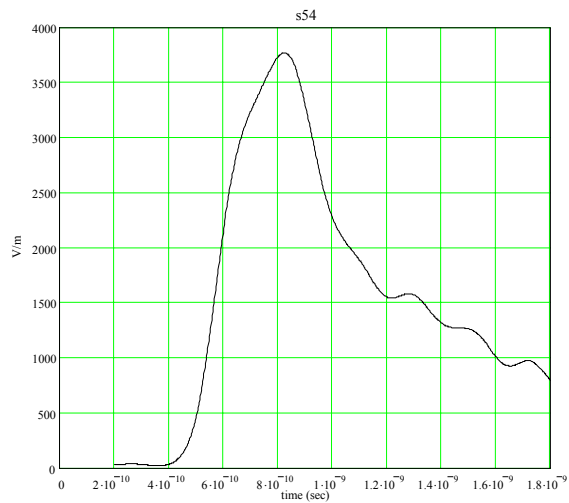
HYPS pulser/TDS820 6GHz sampling scope
 # of Antenna 3
 axis o-p
 radius 50 (cm)
 angle (degrees) 0
 Sensor Prodyne Bdot
 Aeff 10^{-5} m^2



HYPS pulser/TDS820 6GHz sampling scope
 # of Antenna 3
 axis o-p
 radius 30 (cm)
 angle (degrees) 0
 Sensor Prodyne Bdot
 Aeff 10^{-5} m^2

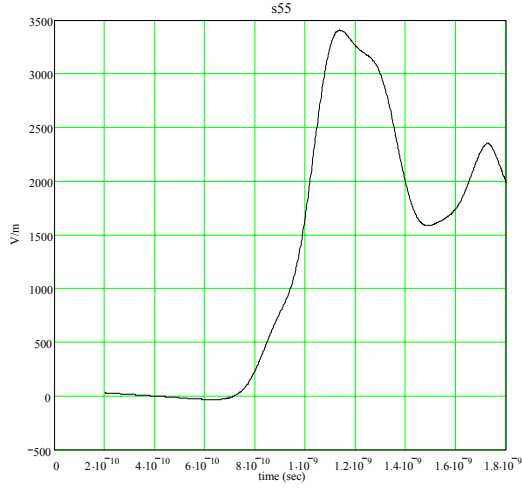


HYPS pulser/TDS820 6GHz sampling scope
 # of Antenna 3
 axis o-p
 radius 10 (cm)
 angle (degrees) 0
 Sensor Prodyne Bdot
 Aeff 10^{-5} m^2

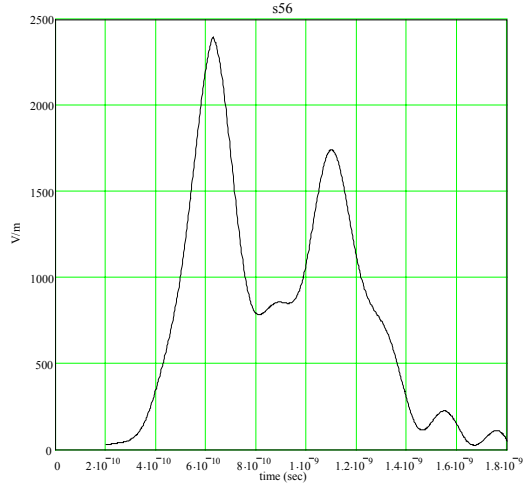


Appendix C. Datatakes 55-62.

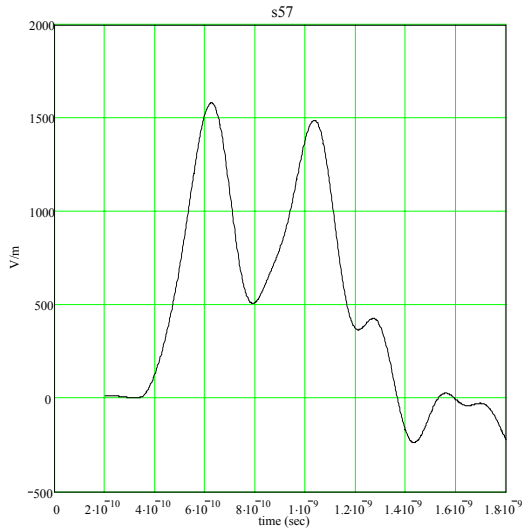
HYPS pulser/TDS820 6GHz sampling scope
 # of Antenna 3
 time sequence (nominal 26.57 deg. phase shift)
 axis o-p
 radius 10 (cm)
 angle (degrees) 0
 Sensor Prodyne Bdot
 Aeff 10^{-5} m^2



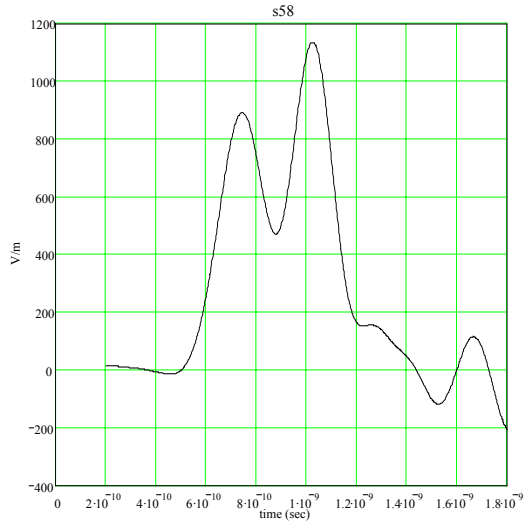
HYPS pulser/TDS820 6GHz sampling scope
 # of Antenna 3
 time sequence (nominal 26.57 deg. phase shift)
 axis o-p
 radius 30 (cm)
 angle (degrees) 0
 Sensor Prodyne Bdot
 Aeff 10^{-5} m^2



HYPS pulser/TDS820 6GHz sampling scope
 # of Antenna 3
 time sequence (nominal 26.57 deg. phase shift)
 axis o-p
 radius 50 (cm)
 angle (degrees) 0
 Sensor Prodyne Bdot
 Aeff 10^{-5} m^2

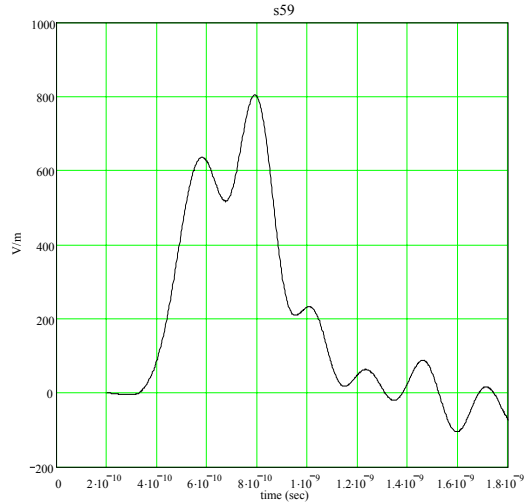


HYPS pulser/TDS820 6GHz sampling scope
 # of Antenna 3
 time sequence (nominal 26.57 deg. phase shift)
 axis o-p
 radius 100 (cm)
 angle (degrees) 0
 Sensor Prodyne Bdot
 Aeff 10^{-5} m^2

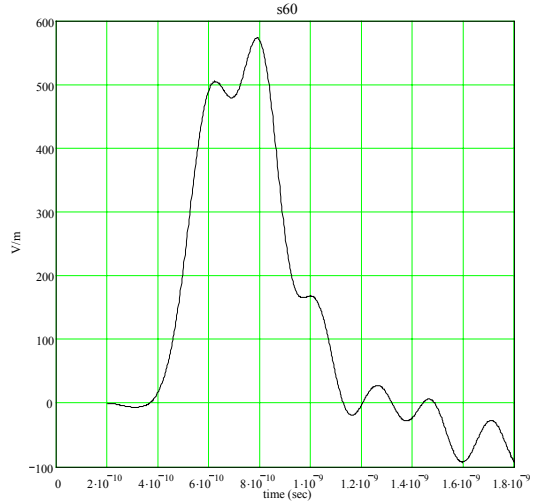


Appendix C. Datatakes 55-62 (Cont.)

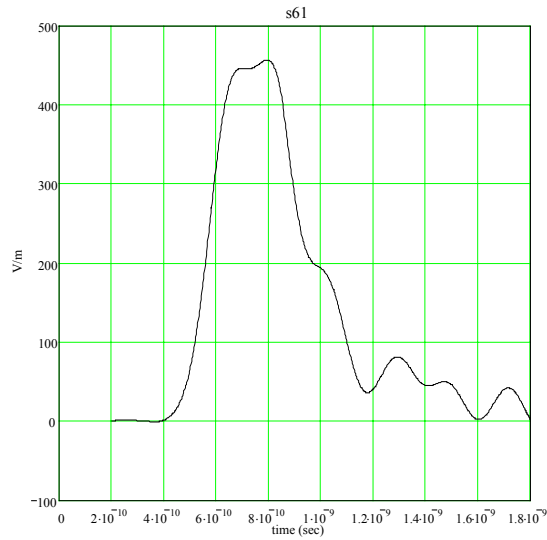
HYPS pulser/TDS820 6GHz sampling scope
 # of Antenna 3
 time sequence (nominal 26.57 deg. phase shift)
 axis o-p
 radius 150 (cm)
 angle (degrees) 0
 Sensor Prodyne Bdot
 Aeff 10^{-5}m^2



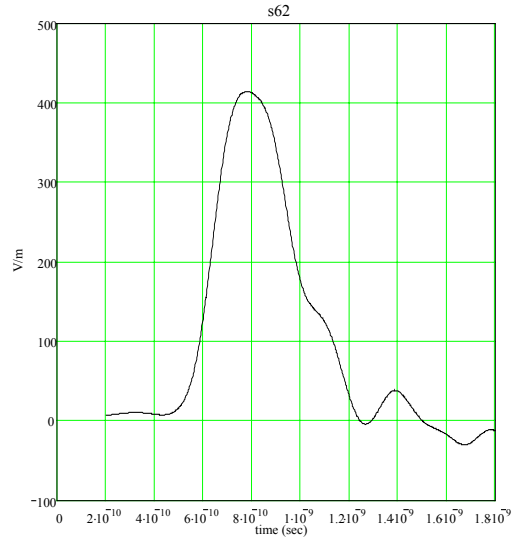
HYPS pulser/TDS820 6GHz sampling scope
 # of Antenna 3
 time sequence (nominal 26.57 deg. phase shift)
 axis o-p
 radius 200 (cm)
 angle (degrees) 0
 Sensor Prodyne Bdot
 Aeff 10^{-5}m^2



HYPS pulser/TDS820 6GHz sampling scope
 # of Antenna 3
 time sequence (nominal 26.57 deg. phase shift)
 axis o-p
 radius 250 (cm)
 angle (degrees) 0
 Sensor Prodyne Bdot
 Aeff 10^{-5}m^2

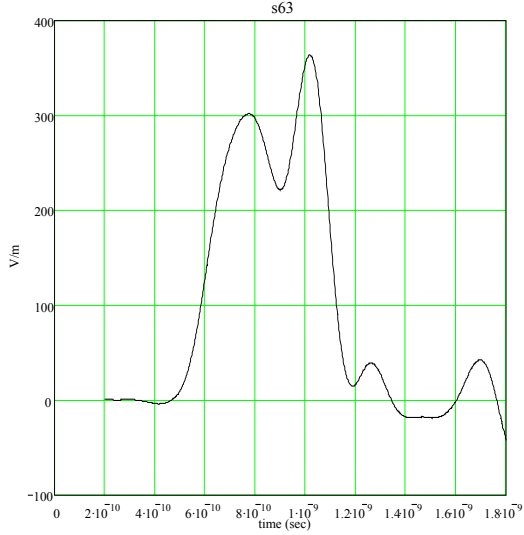


HYPS pulser/TDS820 6GHz sampling scope
 # of Antenna 3
 time sequence (nominal 26.57 deg. phase shift)
 axis o-p
 radius 300 (cm)
 angle (degrees) 0
 Sensor Prodyne Bdot
 Aeff 10^{-5}m^2

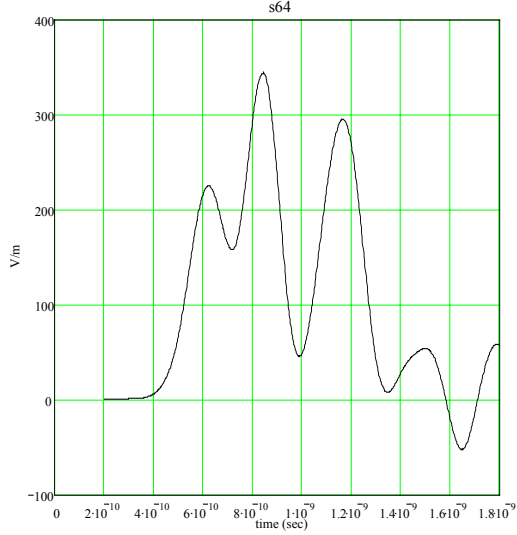


Appendix C. Datatakes 63-71.

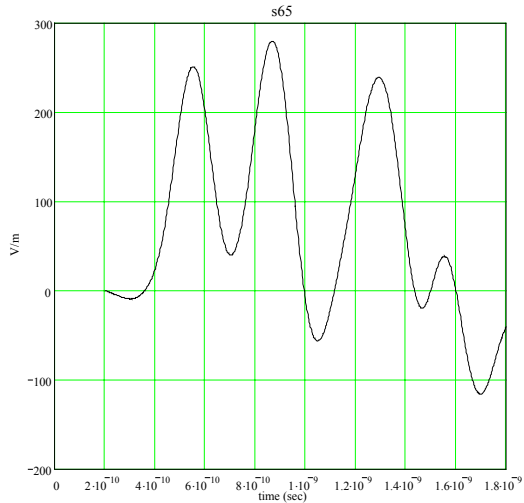
HYPs pulser/TDS820 6GHz sampling scope
 # of Antenna 3
 time sequence (nominal 26.57 deg. phase shift)
 arc p-q
 radius 300 (cm)
 angle (degrees) 19.93
 Sensor Prodyne Bdot
 Aeff 10^5m^2



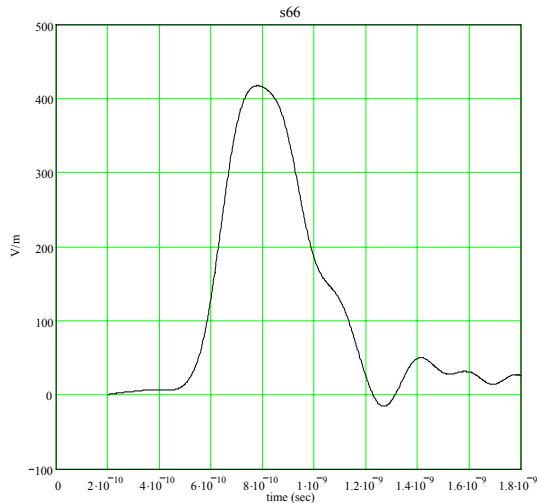
HYPs pulser/TDS820 6GHz sampling scope
 # of Antenna 3
 time sequence (nominal 26.57 deg. phase shift)
 arc p-q
 radius 300 (cm)
 angle (degrees) 13.285
 Sensor Prodyne Bdot
 Aeff 10^5m^2



HYPs pulser/TDS820 6GHz sampling scope
 # of Antenna 3
 time sequence (nominal 26.57 deg. phase shift)
 arc p-q
 radius 300 (cm)
 angle (degrees) 6.64
 Sensor Prodyne Bdot
 Aeff 10^5m^2



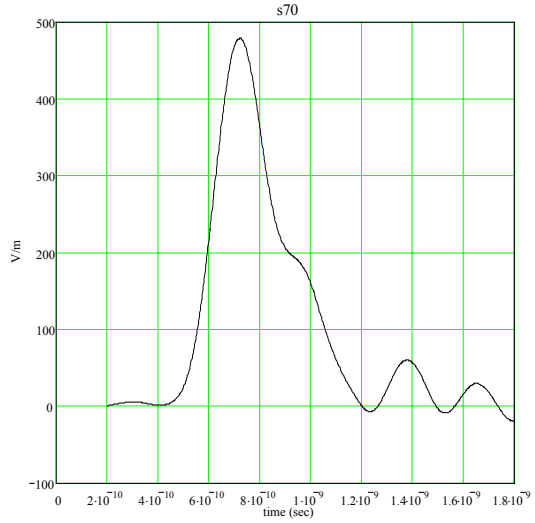
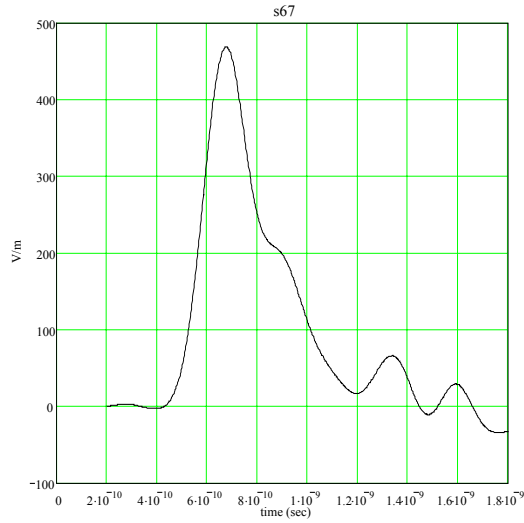
HYPs pulser/TDS820 6GHz sampling scope
 # of Antenna 3
 time sequence (nominal 26.57 deg. phase shift)
 arc p-q
 radius 300 (cm)
 angle (degrees) 26.57
 Sensor Prodyne Bdot
 Aeff 10^5m^2



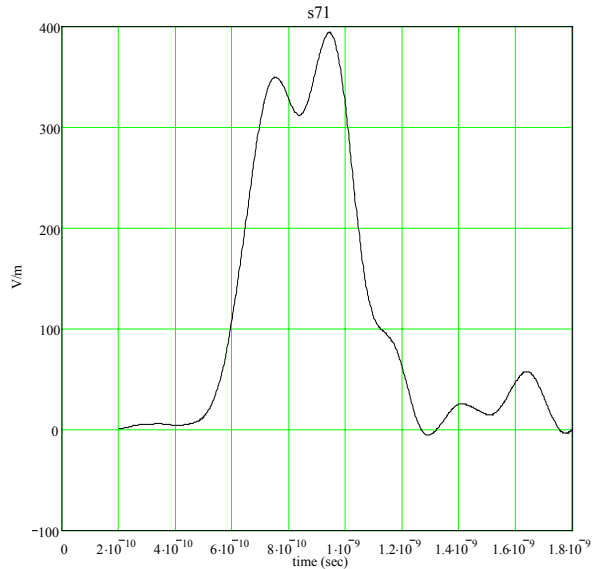
Appendix C. Datatakes 63-71(Cont.)

HYPs pulser/TDS820 6GHz sampling scope
 # of Antenna 3
 time sequence (nominal 26.57 deg. phase shift)
 arc p-q
 radius 300 (cm)
 angle (degrees) 33.213
 Sensor Prodyne Bdot
 Aeff 10^{-9}m^2

HYPs pulser/TDS820 6GHz sampling scope
 # of Antenna 3
 time sequence (nominal 26.57 deg. phase shift)
 arc p-q
 radius 300 (cm)
 angle (degrees) 29.89
 Sensor Prodyne Bdot
 Aeff 10^{-9}m^2

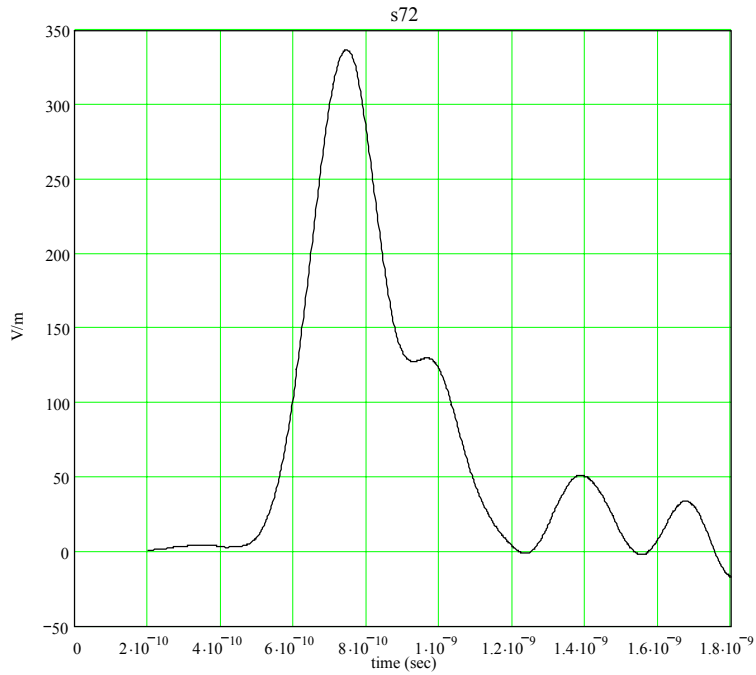


HYPs pulser/TDS820 6GHz sampling scope
 # of Antenna 3
 time sequence (nominal 26.57 deg. phase shift)
 arc p-q
 radius 300 (cm)
 angle (degrees) 23.25
 Sensor Prodyne Bdot
 Aeff 10^{-9}m^2



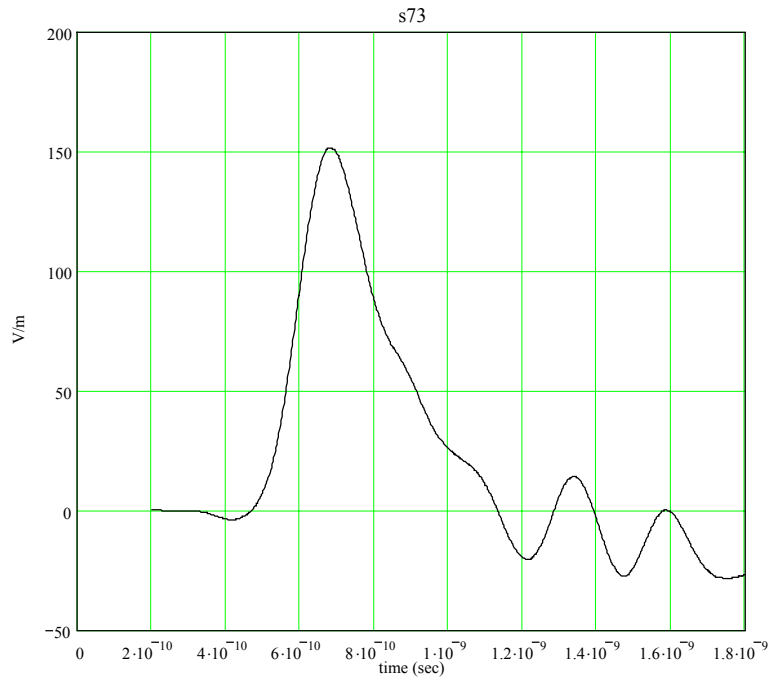
Appendix C. Datatake 72.

HYPs pulser/TDS820 6GHz sampling scope
of Antenna 2 (no A2)
time sequence (nominal 26.57 deg. phase shift)
arc p-q
radius 300 (cm)
angle (degrees) 29.89
Sensor Prodyne Bdot
Aeff 10^{-5} m^2



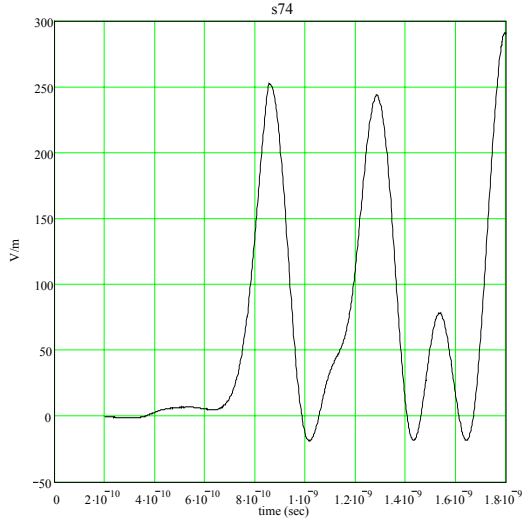
Appendix C. Datatake 73.

HYPs pulser/TDS820 6GHz sampling scope
of Antenna 1 (A2 only)
time sequence (nominal 26.57 deg. phase shift)
arc p-q
radius 300 (cm)
angle (degrees) 29.89
Sensor Prodyne Bdot
Aeff 10^{-5} m^2

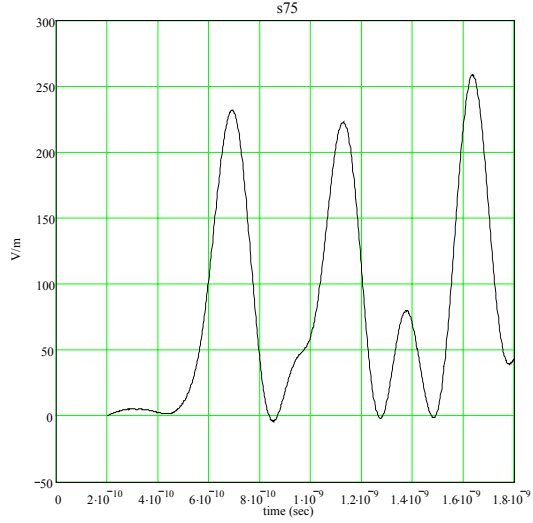


Appendix C. Datatakes 74-90.

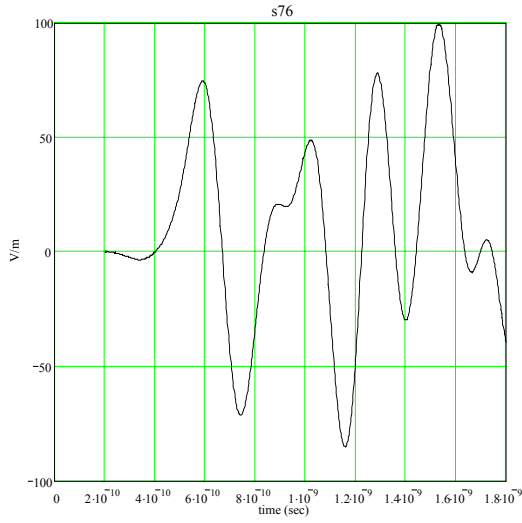
HYPS pulser/TDS820 6GHz sampling scope
 # of Antenna 3
 time sequence (nominal 26.57 deg. phase shift)
 axis o-q
 radius 350 (cm)
 angle (degrees) 0
 Sensor Prodyne Bdot
 Aeff 10^5m^2



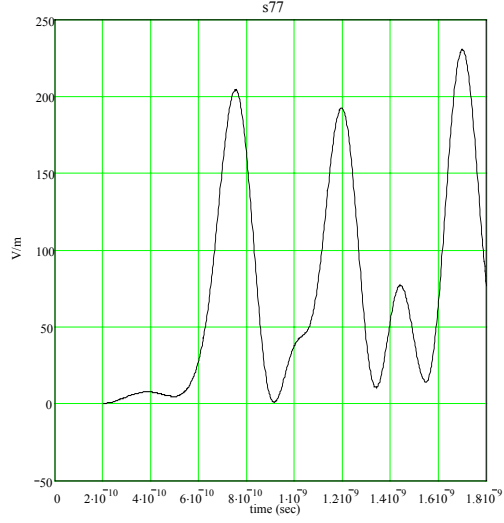
HYPS pulser/TDS820 6GHz sampling scope
 # of Antenna 3
 time sequence (nominal 26.57 deg. phase shift)
 axis o-q
 radius 400 (cm)
 angle (degrees) 0
 Sensor Prodyne Bdot
 Aeff 10^5m^2



HYPS pulser/TDS820 6GHz sampling scope
 # of Antenna 3
 time sequence (nominal 26.57 deg. phase shift)
 axis o-q
 radius 450 (cm)
 angle (degrees) 0
 Sensor Prodyne Bdot
 Aeff 10^5m^2

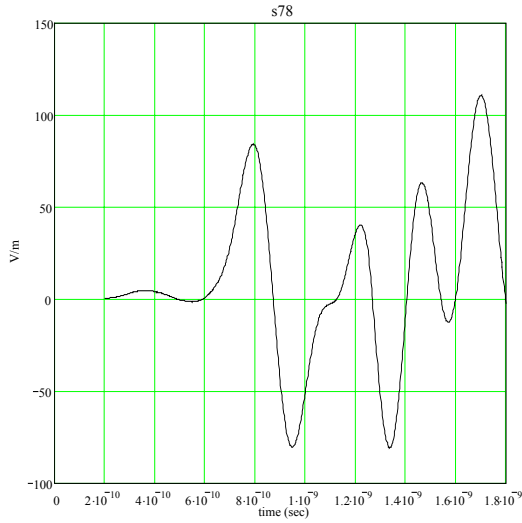


HYPS pulser/TDS820 6GHz sampling scope
 # of Antenna 3
 time sequence (nominal 26.57 deg. phase shift)
 axis o-q
 radius 500 (cm)
 angle (degrees) 0
 Sensor Prodyne Bdot
 Aeff 10^5m^2

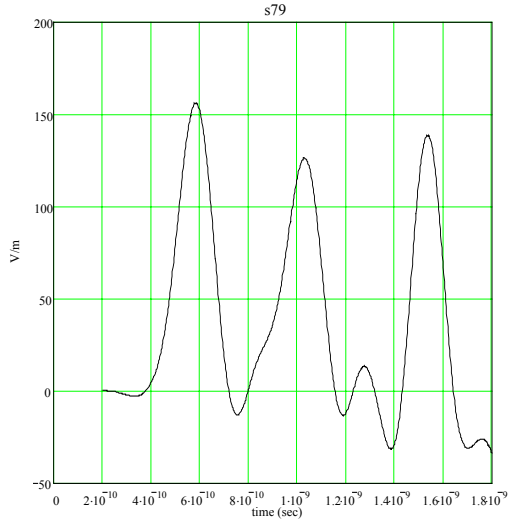


Appendix C. Datatakes 74-90(Cont.)

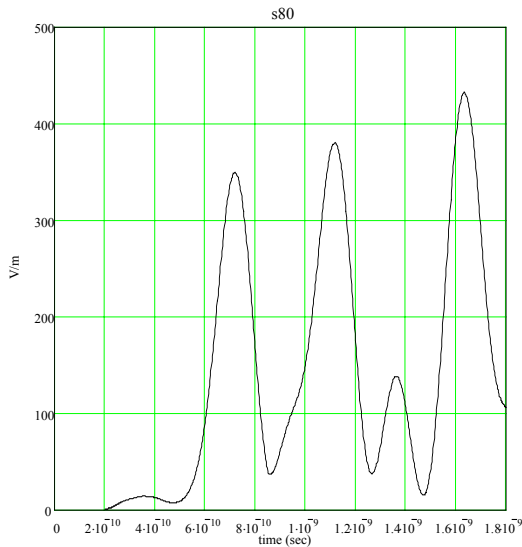
HYPS pulser/TDS820 6GHz sampling scope
 # of Antenna 3
 time sequence (nominal 26.57 deg. phase shift)
 axis o-q
 radius 550 (cm)
 angle (degrees) 0
 Sensor Prodyne Bdot
 Aeff 10^5m^2



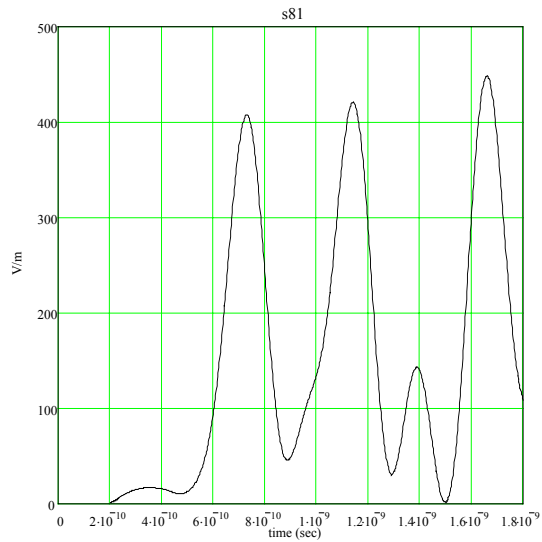
HYPS pulser/TDS820 6GHz sampling scope
 # of Antenna 3
 time sequence (nominal 26.57 deg. phase shift)
 axis o-q
 radius 600 (cm)
 angle (degrees) 0
 Sensor Prodyne Bdot
 Aeff 10^5m^2



HYPS pulser/TDS820 6GHz sampling scope
 # of Antenna 3
 time sequence (nominal 26.57 deg. phase shift)
 axis o-q
 radius 260 (cm)
 angle (degrees) 0
 Sensor Prodyne Bdot
 Aeff 10^5m^2

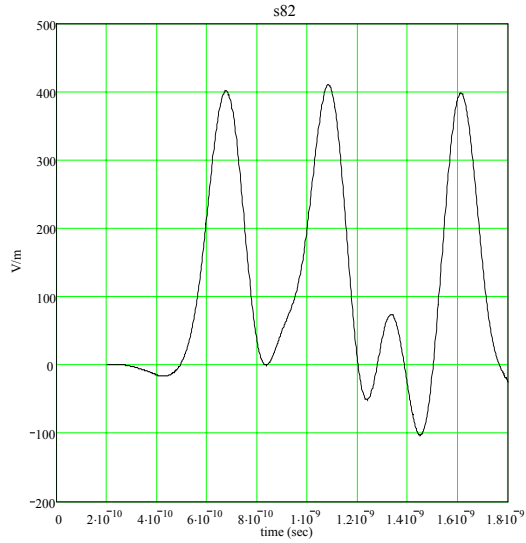


HYPS pulser/TDS820 6GHz sampling scope
 # of Antenna 3
 time sequence (nominal 26.57 deg. phase shift)
 axis o-q
 radius 230 (cm)
 angle (degrees) 0
 Sensor Prodyne Bdot
 Aeff 10^5m^2

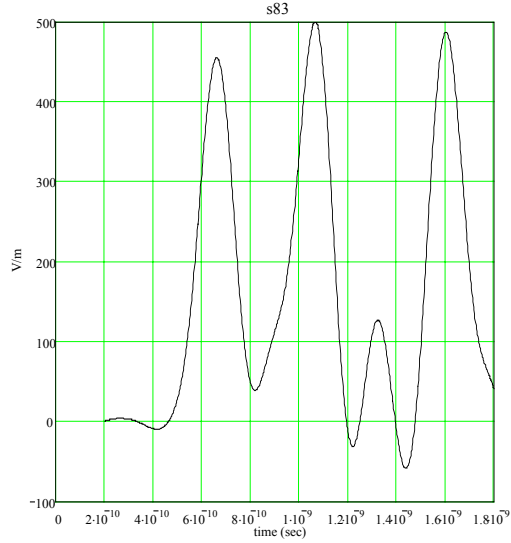


Appendix C. Datatakes 74-90(Cont.)

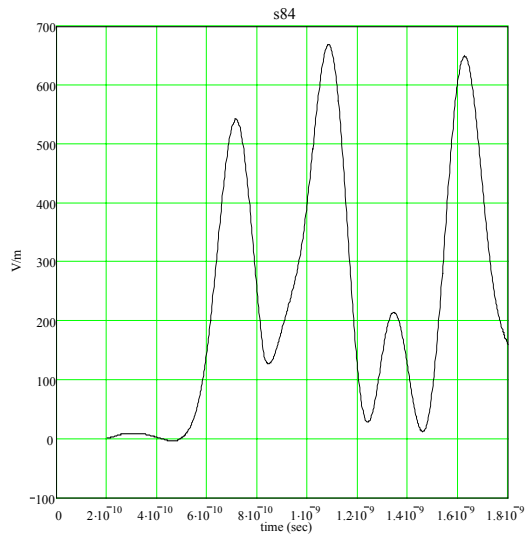
HYPs pulser/TDS820 6GHz sampling scope
 # of Antenna 3
 time sequence (nominal 26.57 deg. phase shift)
 axis o-q
 radius 200 (cm)
 angle (degrees) 0
 Sensor Prodyne Bdot
 Aeff 10^5m^2



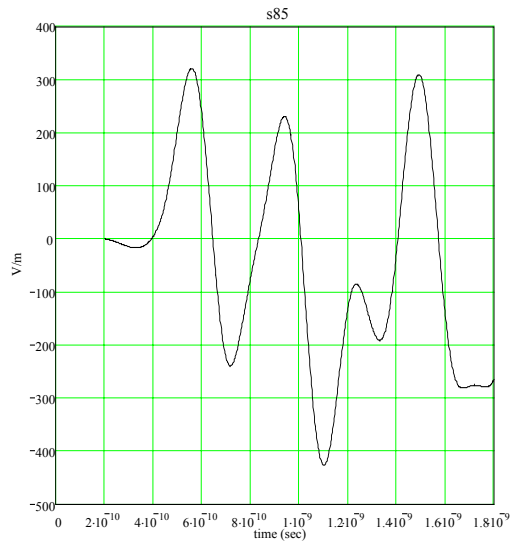
HYPs pulser/TDS820 6GHz sampling scope
 # of Antenna 3
 time sequence (nominal 26.57 deg. phase shift)
 axis o-q
 radius 170 (cm)
 angle (degrees) 0
 Sensor Prodyne Bdot
 Aeff 10^5m^2



HYPs pulser/TDS820 6GHz sampling scope
 # of Antenna 3
 time sequence (nominal 26.57 deg. phase shift)
 axis o-q
 radius 140 (cm)
 angle (degrees) 0
 Sensor Prodyne Bdot
 Aeff 10^5m^2

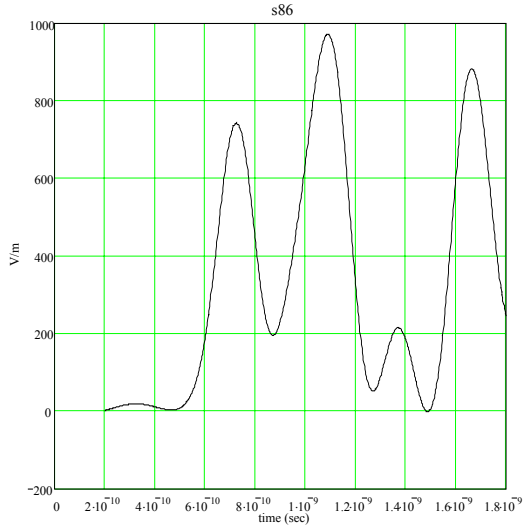


HYPs pulser/TDS820 6GHz sampling scope
 # of Antenna 3
 time sequence (nominal 26.57 deg. phase shift)
 axis o-q
 radius 110 (cm)
 angle (degrees) 0
 Sensor Prodyne Bdot
 Aeff 10^5m^2

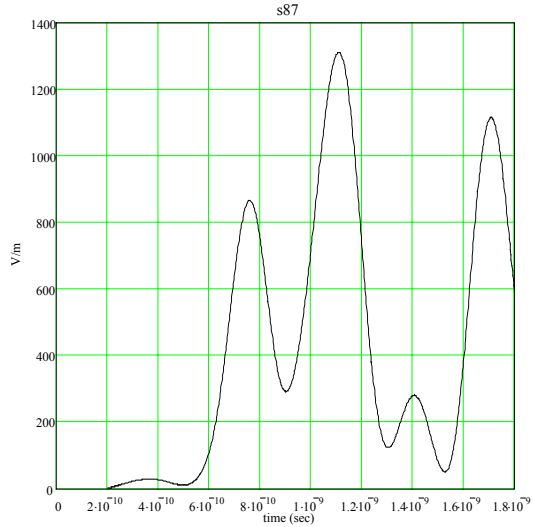


Appendix C. Datatakes 74-90(Cont.)

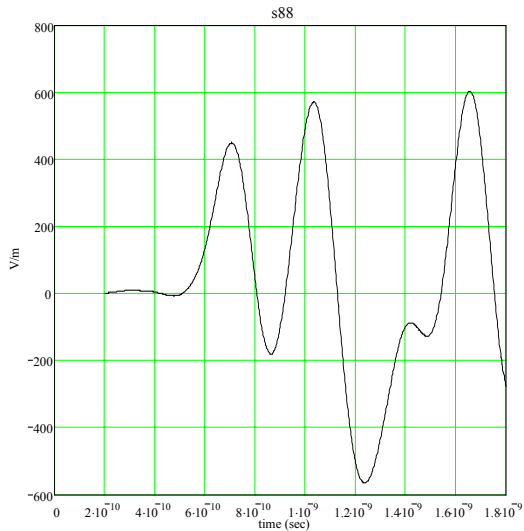
HYPs pulser/TDS820 6GHz sampling scope
 # of Antenna 3
 time sequence (nominal 26.57 deg. phase shift)
 axis o-q
 radius 90 (cm)
 angle (degrees) 0
 Sensor Prodyne Bdot
 Aeff 10^5m^2



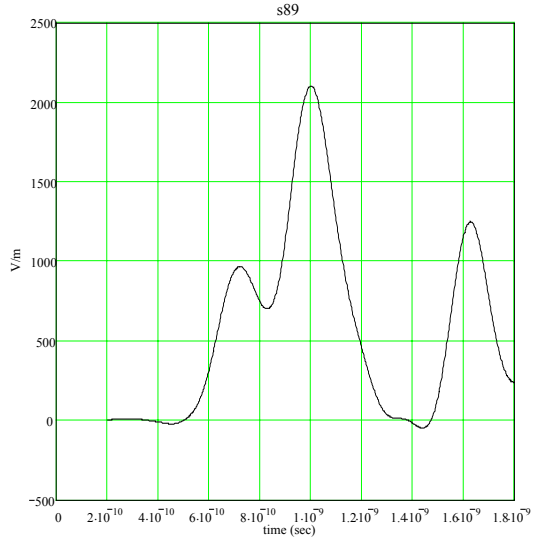
HYPs pulser/TDS820 6GHz sampling scope
 # of Antenna 3
 time sequence (nominal 26.57 deg. phase shift)
 axis o-q
 radius 70 (cm)
 angle (degrees) 0
 Sensor Prodyne Bdot
 Aeff 10^5m^2



HYPs pulser/TDS820 6GHz sampling scope
 # of Antenna 3
 time sequence (nominal 26.57 deg. phase shift)
 axis o-q
 radius 50 (cm)
 angle (degrees) 0
 Sensor Prodyne Bdot
 Aeff 10^5m^2

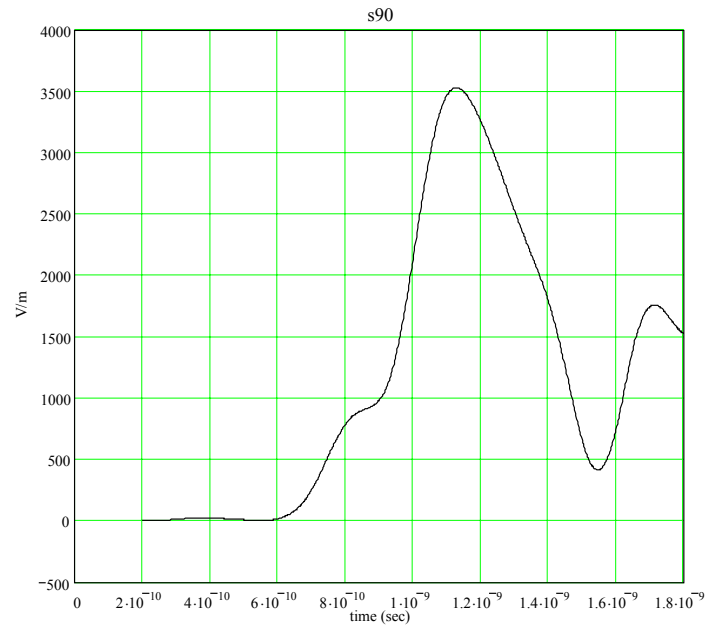


HYPs pulser/TDS820 6GHz sampling scope
 # of Antenna 3
 time sequence (nominal 26.57 deg. phase shift)
 axis o-q
 radius 30 (cm)
 angle (degrees) 0
 Sensor Prodyne Bdot
 Aeff 10^5m^2



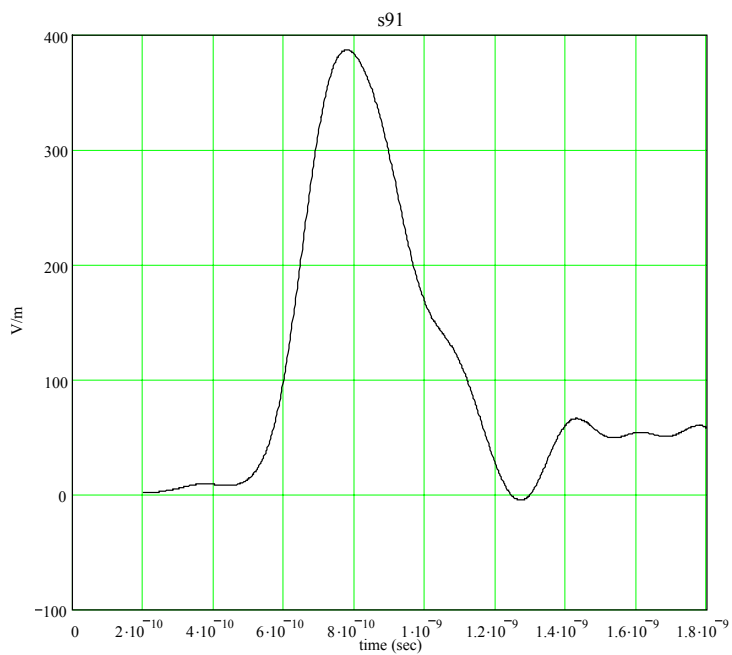
Appendix C. Datatakes 74-90(Cont.)

HYPs pulser/TDS820 6GHz sampling scope
of Antenna 3
time sequence (nominal 26.57 deg. phase shift)
axis o-q
radius 10 (cm)
angle (degrees) 0
Sensor Prodyne Bdot
Aeff 10^{-5} m^2



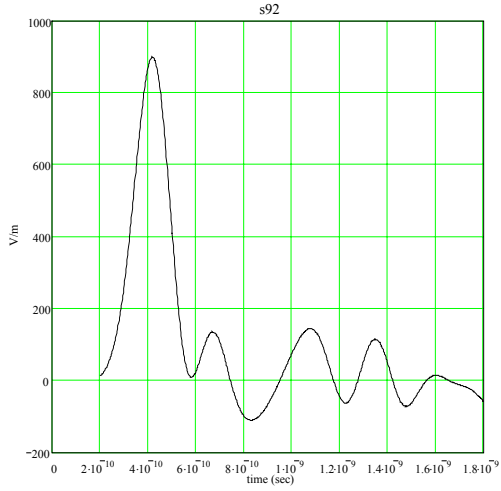
Appendix C. Datatake 91.

HYPs pulser/TDS820 6GHz sampling scope
of Antenna 3
time sequence (nominal 26.57 deg. phase shift)
axis 0-p
radius 350 (cm)
angle (degrees) 26.57
Sensor Prodyne Bdot
Aeff 10^{-5} m^2



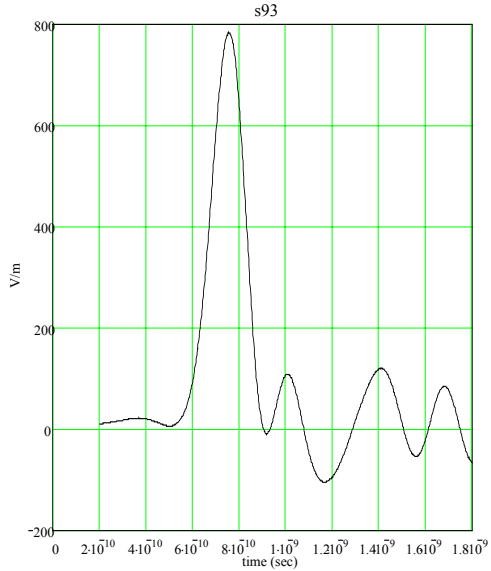
Appendix C. Datatakes 92-106.

HYPS pulser/TDS820 6GHz sampling scope
 # of Antenna 3
 in phase
 axis o-q
 radius 300 (cm)
 angle (degrees) 0
 Sensor Prodyne Bdot
 Aeff 10^5m^2

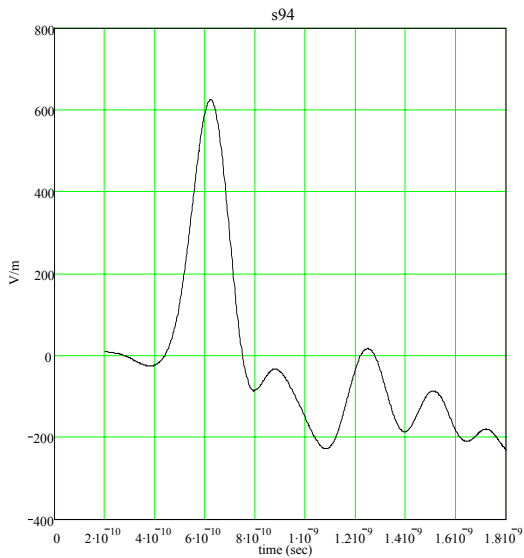


repeat of s38

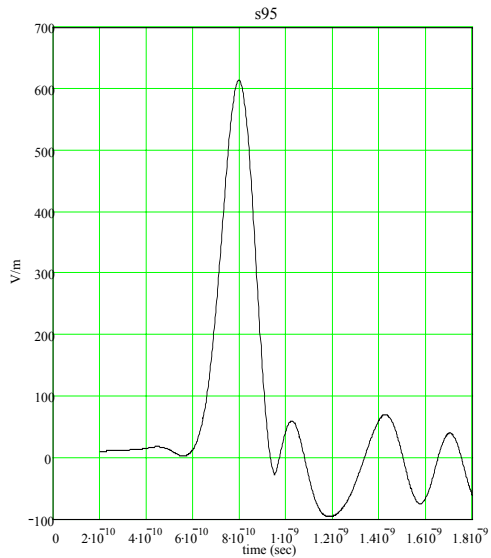
HYPS pulser/TDS820 6GHz sampling scope
 # of Antenna 3
 in phase
 axis o-q
 radius 350 (cm)
 angle (degrees) 0
 Sensor Prodyne Bdot
 Aeff 10^5m^2



HYPS pulser/TDS820 6GHz sampling scope
 # of Antenna 3
 in phase
 axis o-q
 radius 400 (cm)
 angle (degrees) 0
 Sensor Prodyne Bdot
 Aeff 10^5m^2

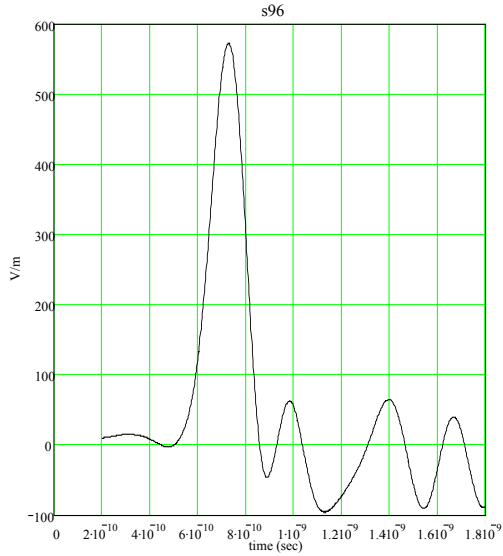


HYPS pulser/TDS820 6GHz sampling scope
 # of Antenna 3
 in phase
 axis o-q
 radius 450 (cm)
 angle (degrees) 0
 Sensor Prodyne Bdot
 Aeff 10^5m^2

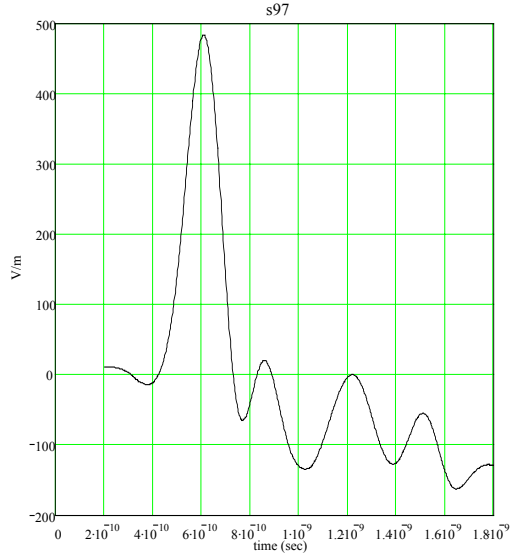


Appendix C. Datatakes 92-106(Cont.)

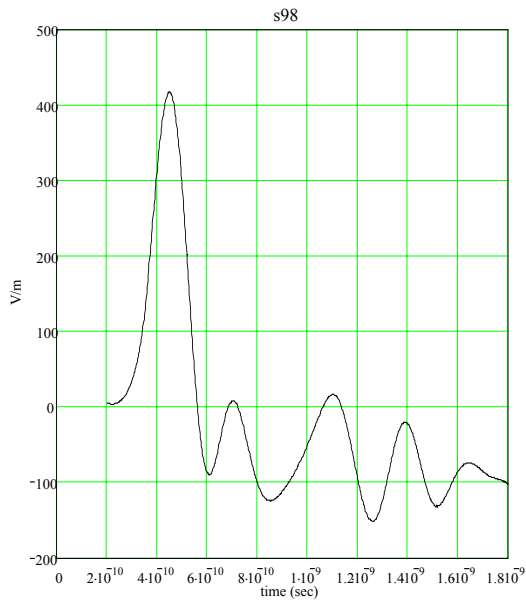
HYPS pulser/TDS820 6GHz sampling scope
 # of Antenna 3
 in phase
 axis o-q
 radius 500 (cm)
 angle (degrees) 0
 Sensor Prodyne Bdot
 Aeff 10^5m^2



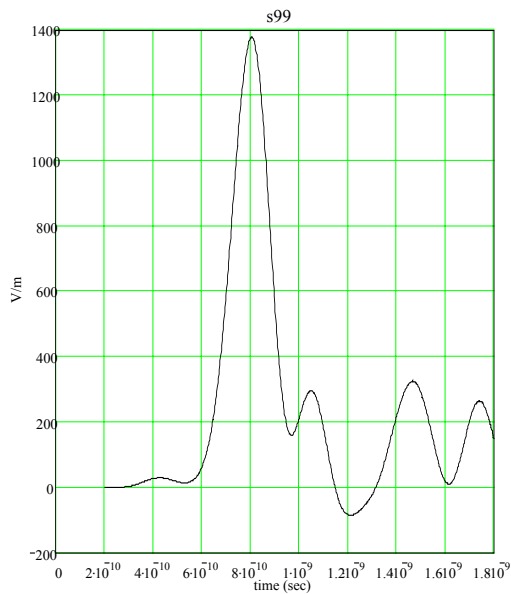
HYPS pulser/TDS820 6GHz sampling scope
 # of Antenna 3
 in phase
 axis o-q
 radius 550 (cm)
 angle (degrees) 0
 Sensor Prodyne Bdot
 Aeff 10^5m^2



HYPS pulser/TDS820 6GHz sampling scope
 # of Antenna 3
 in phase
 axis o-q
 radius 600 (cm)
 angle (degrees) 0
 Sensor Prodyne Bdot
 Aeff 10^5m^2

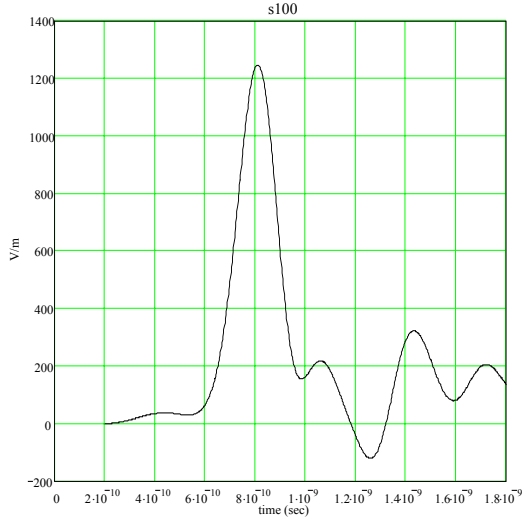


HYPS pulser/TDS820 6GHz sampling scope
 # of Antenna 3
 in phase
 axis o-q
 radius 170 (cm)
 angle (degrees) 0
 Sensor Prodyne Bdot
 Aeff 10^5m^2

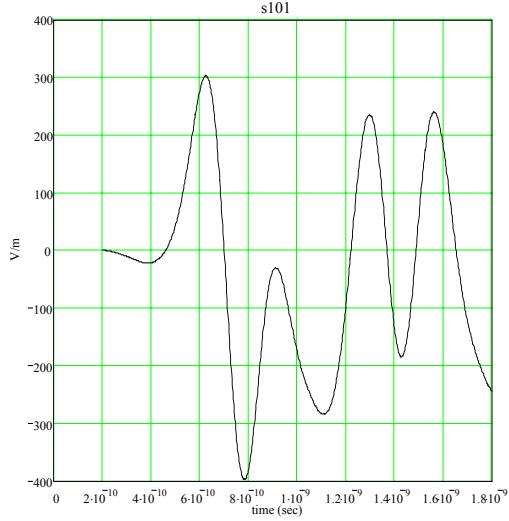


Appendix C. Datatakes 92-106(Cont.)

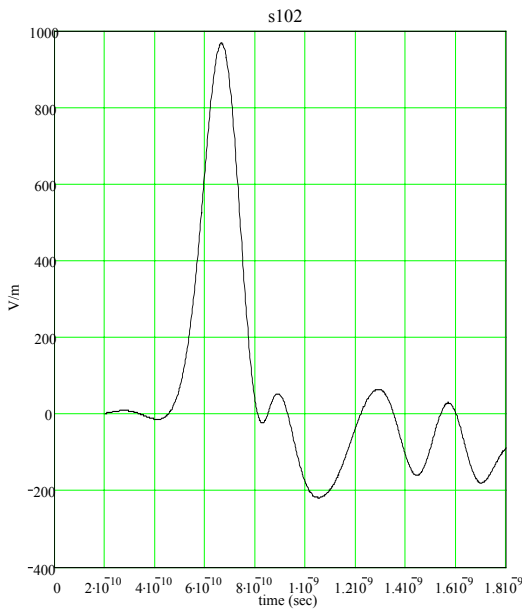
HYPS pulser/TDS820 6GHz sampling scope
 # of Antenna 3
 in phase
 axis o-q
 radius 200 (cm)
 angle (degrees) 0
 Sensor Prodyne Bdot
 Aeff 10^5m^2



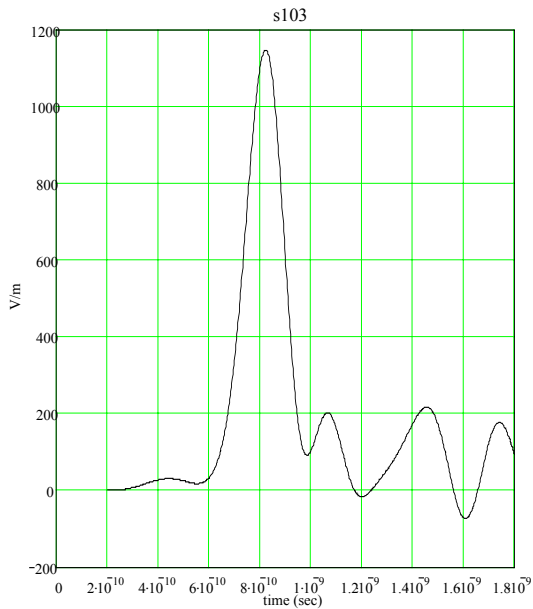
HYPS pulser/TDS820 6GHz sampling scope
 # of Antenna 3
 in phase
 axis o-q
 radius 230 (cm)
 angle (degrees) 0
 Sensor Prodyne Bdot
 Aeff 10^5m^2



HYPS pulser/TDS820 6GHz sampling scope
 # of Antenna 3
 in phase
 axis o-q
 radius 260 (cm)
 angle (degrees) 0
 Sensor Prodyne Bdot
 Aeff 10^5m^2

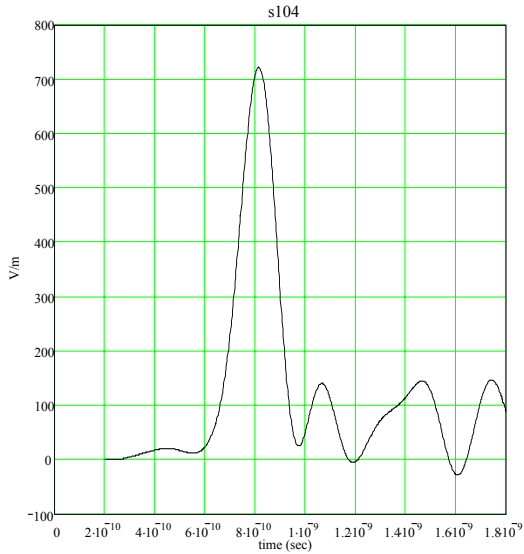


HYPS pulser/TDS820 6GHz sampling scope
 # of Antenna 3
 in phase
 axis o-q
 radius 230 (cm)
 angle (degrees) 0
 Sensor Prodyne Bdot
 Aeff 10^5m^2

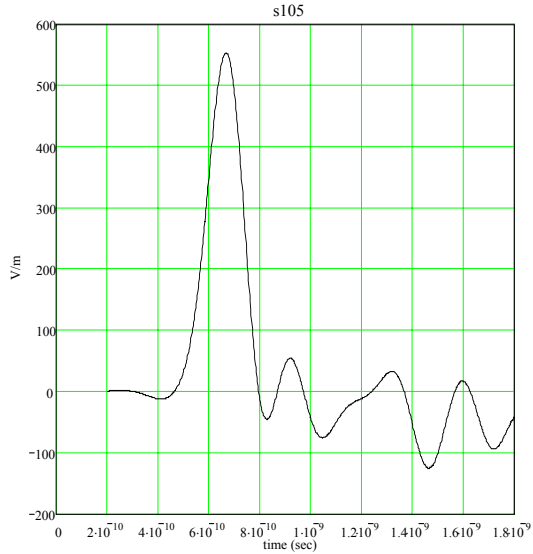


Appendix C. Datatakes 92-106(Cont.)

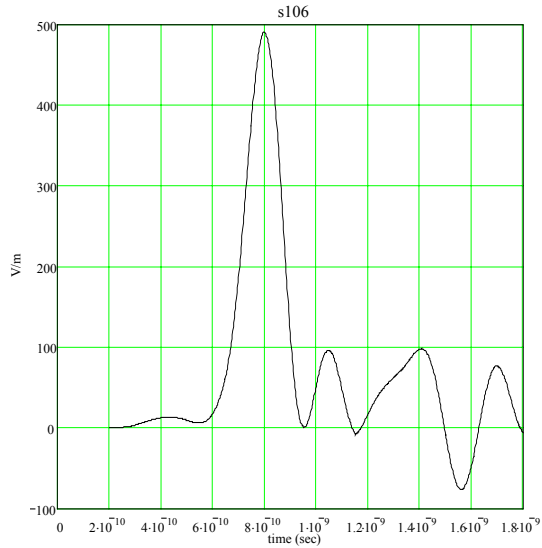
HYPS pulser/TDS820 6GHz sampling scope
 # of Antenna 3
 in phase
 axis o-q
 radius 400 (cm)
 angle (degrees) 0
 Sensor Prodyne Bdot
 Aeff 10^5m^2



HYPS pulser/TDS820 6GHz sampling scope
 # of Antenna 3
 in phase
 axis o-q
 radius 500 (cm)
 angle (degrees) 0
 Sensor Prodyne Bdot
 Aeff 10^5m^2

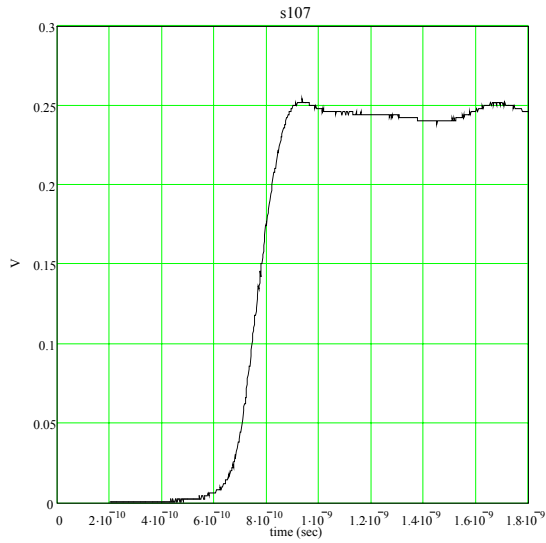


HYPS pulser/TDS820 6GHz sampling scope
 # of Antenna 3
 in phase
 axis o-q
 radius 600 (cm)
 angle (degrees) 0
 Sensor Prodyne Bdot
 Aeff 10^5m^2

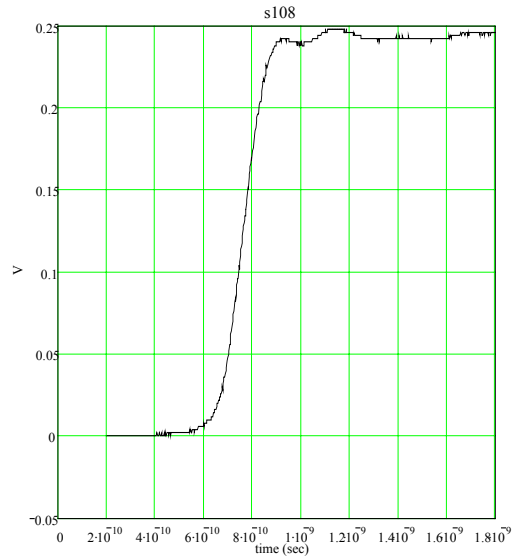


Appendix C. Datatakes 107-113.

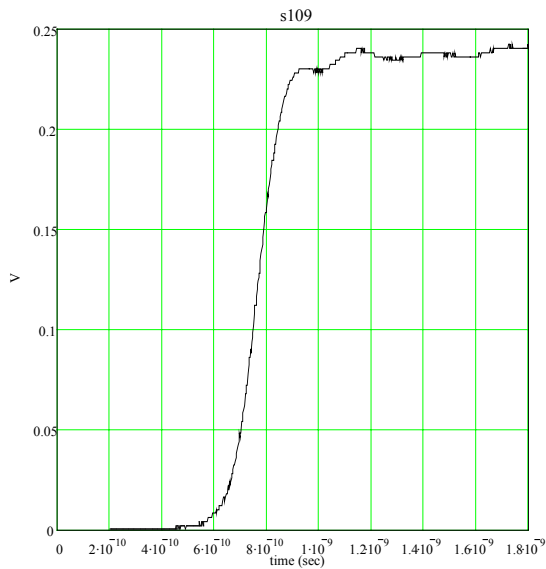
Tunnel diode pulser direct into TDS 820



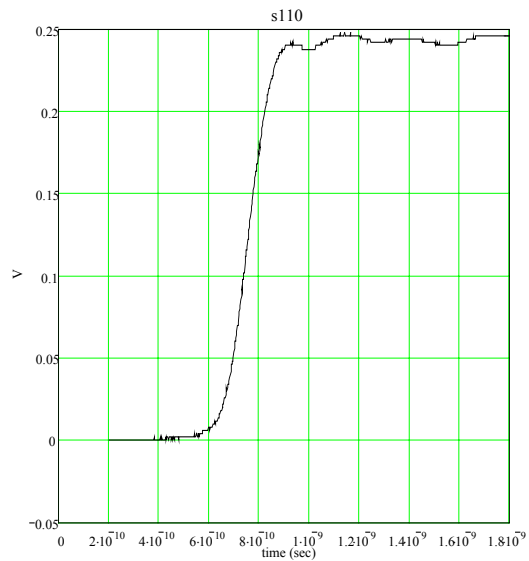
Tunnel diode pulser
5.15 ns RG214 into TDS 820



Tunnel diode pulser
55 ns Foamflex into TDS 820

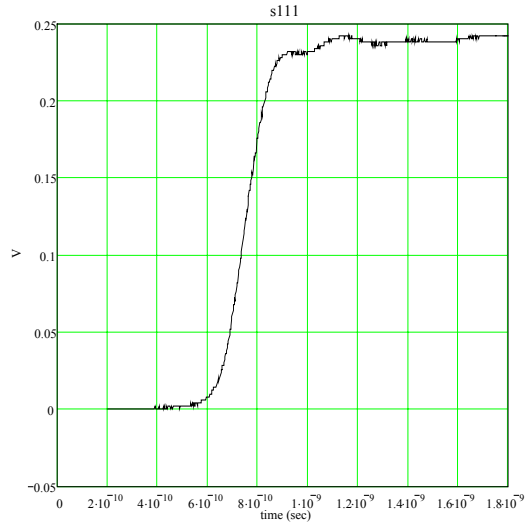


Tunnel diode pulser
6.54 ns RG214 into TDS 820

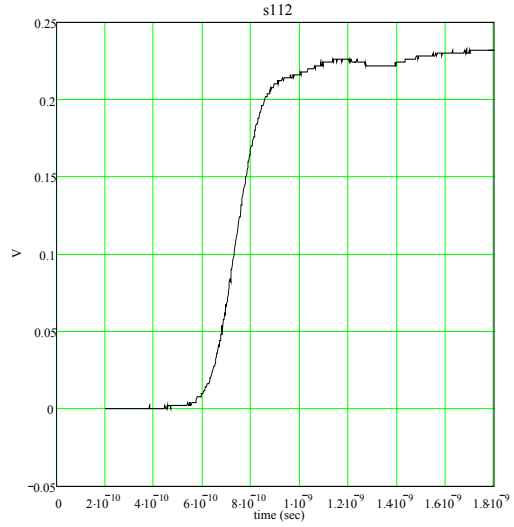


Appendix C. Datatakes 107-113(Cont.)

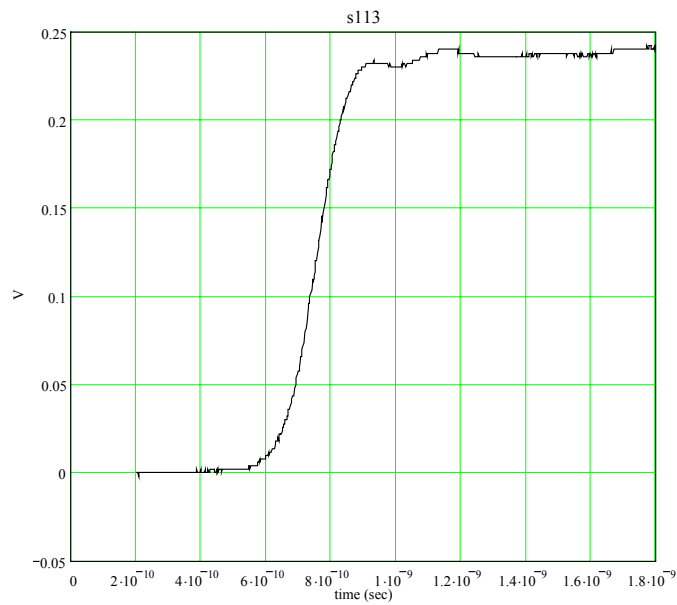
Tunnel diode pulser
14 ns RG214 into TDS 820



Tunnel diode pulser
19.63 ns RG223 into TDS 820

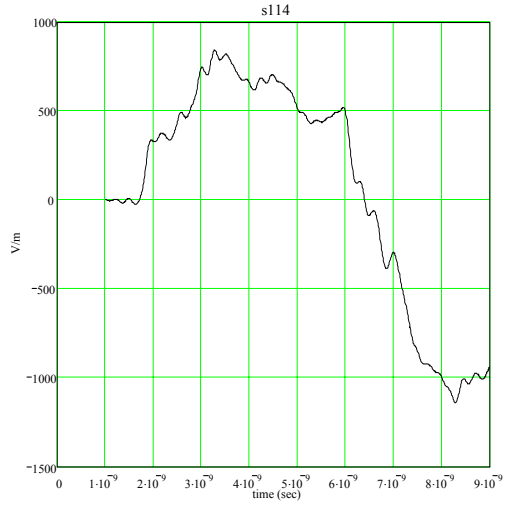


Tunnel diode pulser
28.5 ns Spiral line foamflex into TDS 820

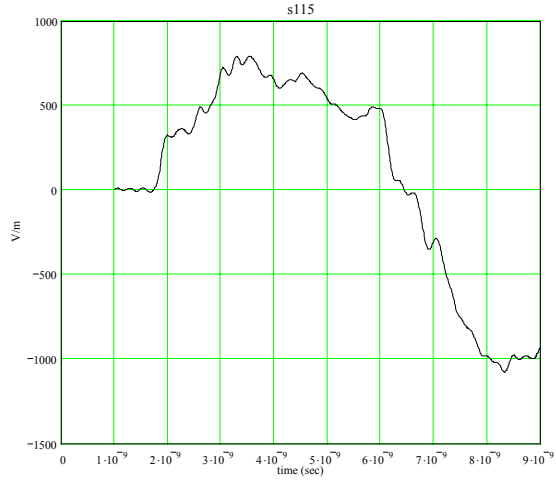


Appendix C. Datatakes 114-116.

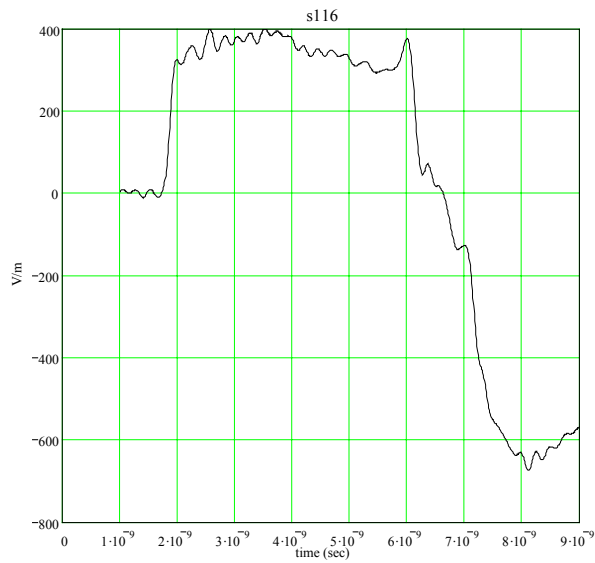
HYPS pulser/TDS820 6GHz sampling scope
 # of Antenna 1
 in phase
 normal bias resistor setup
 axis o-q
 radius -70 (cm)
 angle (degrees) 0
 Sensor Prodyne Bdot
 Aeff 10^{-5} m^2



HYPS pulser/TDS820 6GHz sampling scope
 # of Antenna 1
 in phase
 no bias resistors short
 axis o-q
 radius -70 (cm)
 angle (degrees) 0
 Sensor Prodyne Bdot
 Aeff 10^{-5} m^2



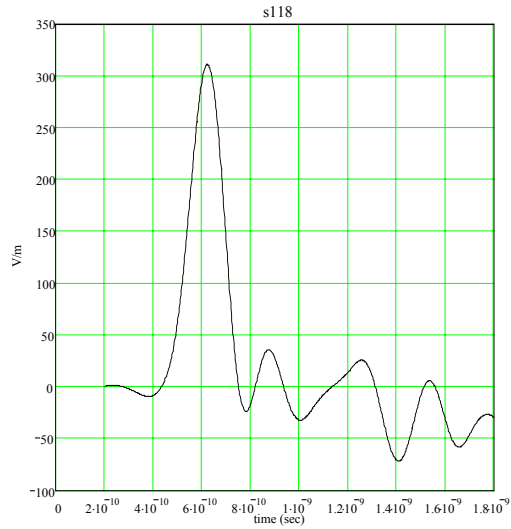
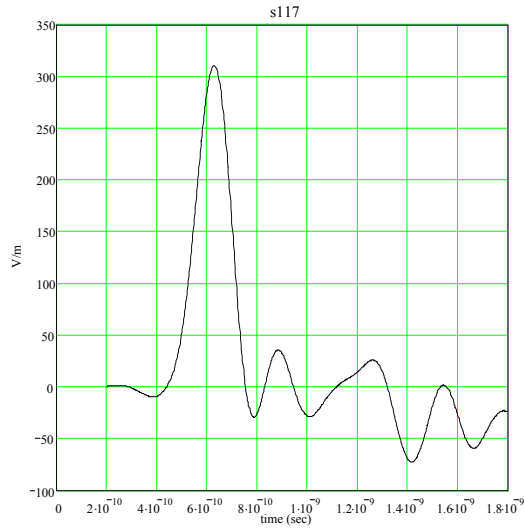
HYPS pulser/TDS820 6GHz sampling scope
 # of Antenna 1
 in phase
 no bias no shield
 axis o-q
 radius -70 (cm)
 angle (degrees) 0
 Sensor Prodyne Bdot
 Aeff 10^{-5} m^2



Appendix C. Datatakes 117-118.

HYPs pulser/TDS820 6GHz sampling scope
 # of Antenna 1
 in phase
 no bias no shield
 axis o-q
 radius 300 (cm)
 angle (degrees) 0
 Sensor Prodyne Bdot
 Aeff 10^5m^2

HYPs pulser/TDS820 6GHz sampling scope
 # of Antenna 1
 in phase
 normal resistive bias and shield
 axis o-q
 radius 300 (cm)
 angle (degrees) 0
 Sensor Prodyne Bdot
 Aeff 10^5m^2



Appendix C. Datatake 119.

HYPS pulser/TDS820 6GHz sampling scope

of Antenna 1

in phase

normal resistive bias and shield

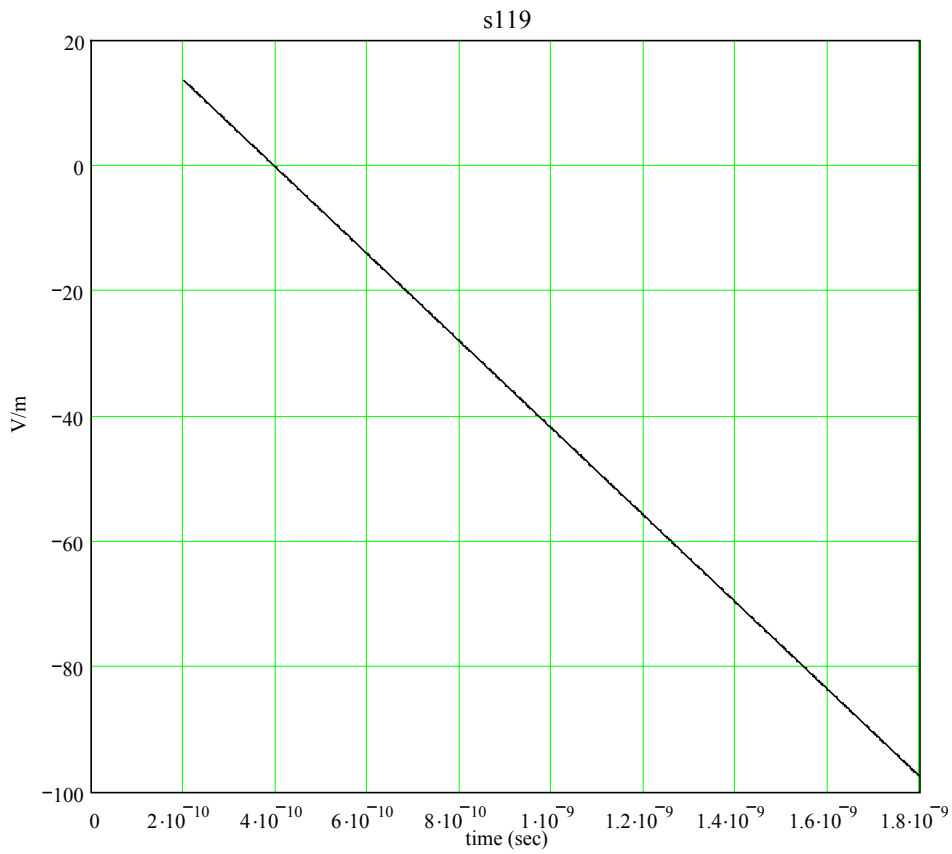
arcs p-q

radius 300 (cm)

angle (degrees) 6.64

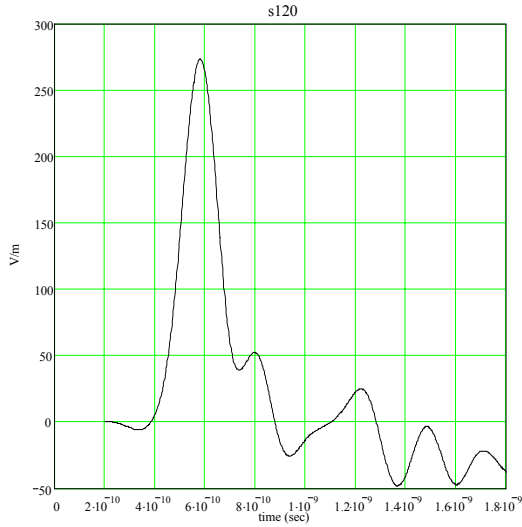
Sensor Prodyne Bdot

Aeff 10^{-5} m^2

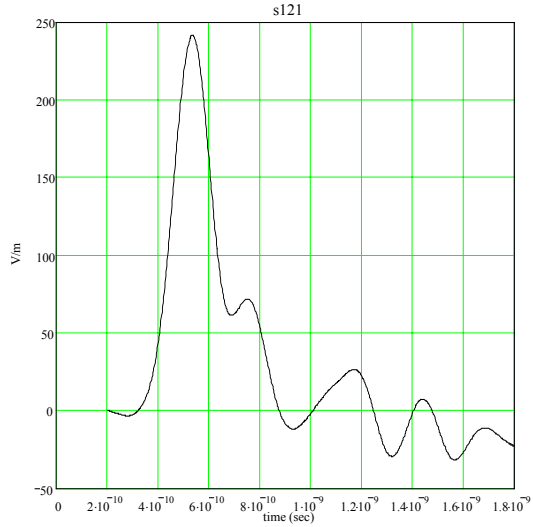


Appendix C. Datatakes 120-123.

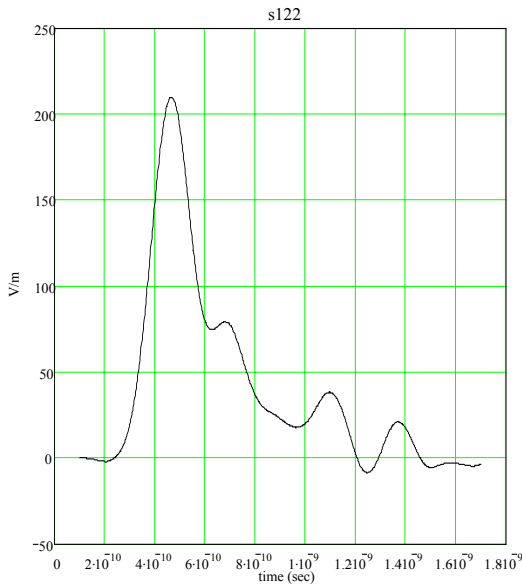
HYPS pulser/TDS820 6GHz sampling scope
 # of Antenna 1
 in phase
 normal resistive bias and shield
 arcs p-q
 radius 300 (cm)
 angle (degrees) 13.285
 Sensor Prodyne Bdot
 Aeff 10^5m^2



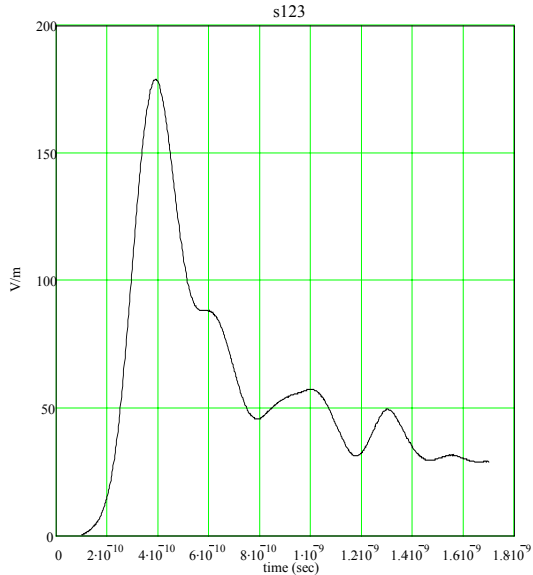
HYPS pulser/TDS820 6GHz sampling scope
 # of Antenna 1
 in phase
 normal resistive bias and shield
 arcs p-q
 radius 300 (cm)
 angle (degrees) 19.93
 Sensor Prodyne Bdot
 Aeff 10^6m^2



HYPS pulser/TDS820 6GHz sampling scope
 # of Antenna 1
 in phase
 normal resistive bias and shield
 arcs p-q
 radius 300 (cm)
 angle (degrees) 26.57
 Sensor Prodyne Bdot
 Aeff 10^5m^2

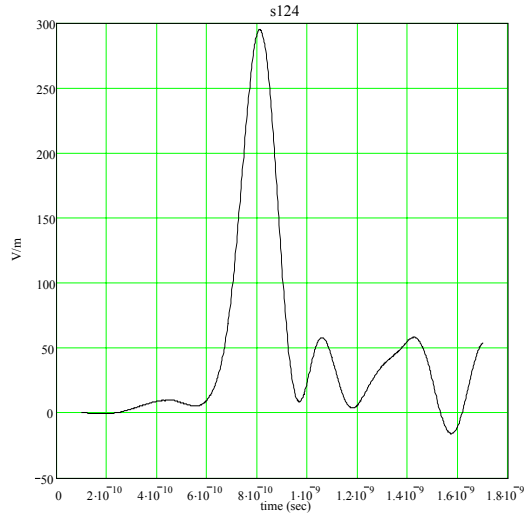


HYPS pulser/TDS820 6GHz sampling scope
 # of Antenna 1
 in phase
 normal resistive bias and shield
 arcs p-q
 radius 300 (cm)
 angle (degrees) 33.21
 Sensor Prodyne Bdot
 Aeff 10^6m^2

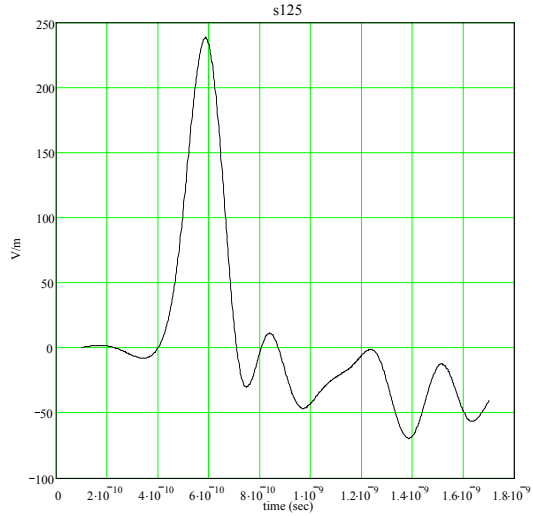


Appendix C. Datatakes 124-140.

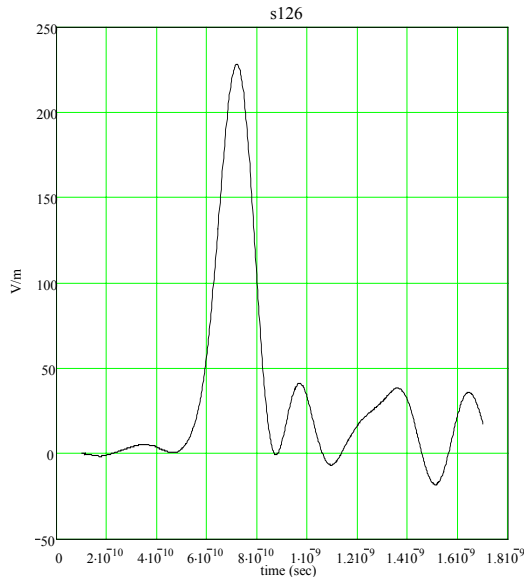
HYPS pulser/TDS820 6GHz sampling scope
 # of Antenna 1
 in phase
 normal resistive bias and shield
 axis o-q
 radius 350 (cm)
 angle (degrees) 0
 Sensor Prodyne Bdot
 Aeff 10^5m^2



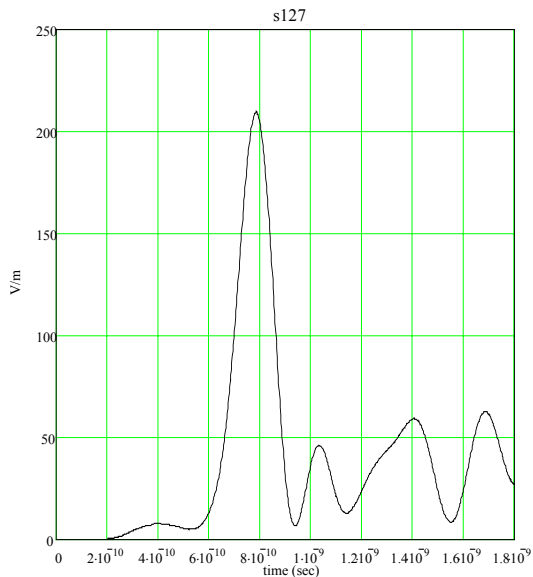
HYPS pulser/TDS820 6GHz sampling scope
 # of Antenna 1
 in phase
 normal resistive bias and shield
 axis o-q
 radius 400 (cm)
 angle (degrees) 0
 Sensor Prodyne Bdot
 Aeff 10^5m^2



HYPS pulser/TDS820 6GHz sampling scope
 # of Antenna 1
 in phase
 normal resistive bias and shield
 axis o-q
 radius 450 (cm)
 angle (degrees) 0
 Sensor Prodyne Bdot
 Aeff 10^5m^2

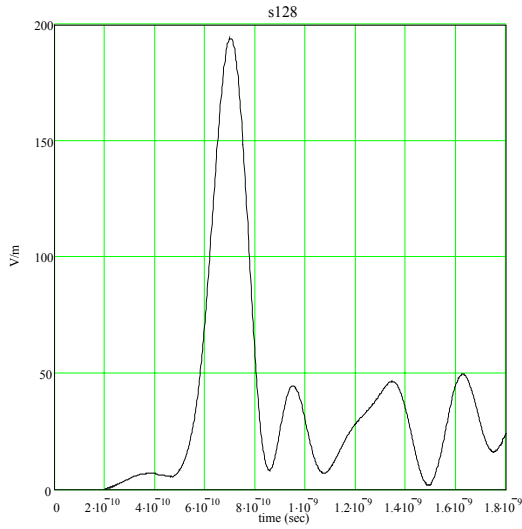


HYPS pulser/TDS820 6GHz sampling scope
 # of Antenna 1
 in phase
 normal resistive bias and shield
 axis o-q
 radius 500 (cm)
 angle (degrees) 0
 Sensor Prodyne Bdot
 Aeff 10^5m^2

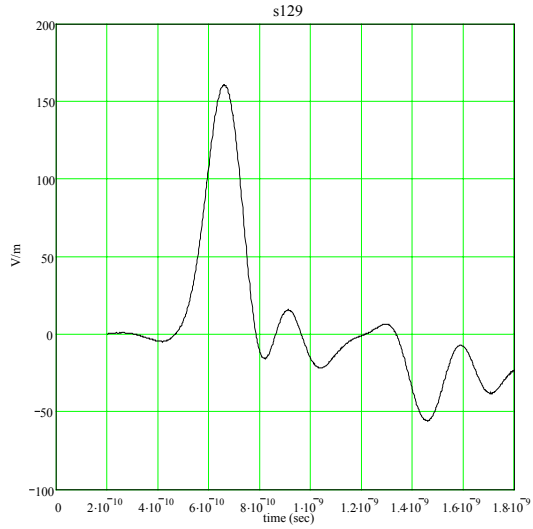


Appendix C. Datatakes 124-140(Cont.)

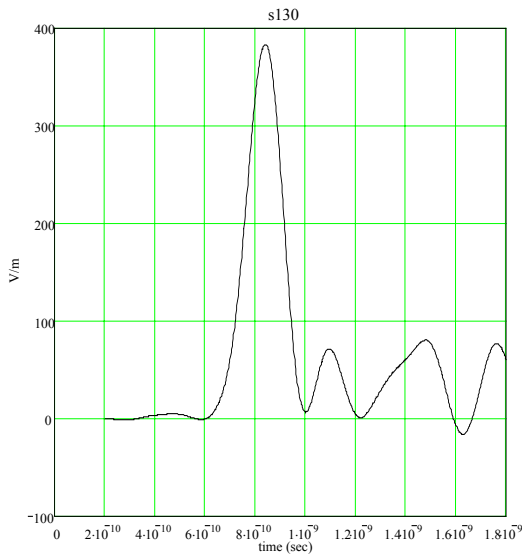
HYPS pulser/TDS820 6GHz sampling scope
 # of Antenna 1
 in phase
 normal resistive bias and shield
 axis o-q
 radius 550 (cm)
 angle (degrees) 0
 Sensor Prodyne Bdot
 Aeff 10^5m^2



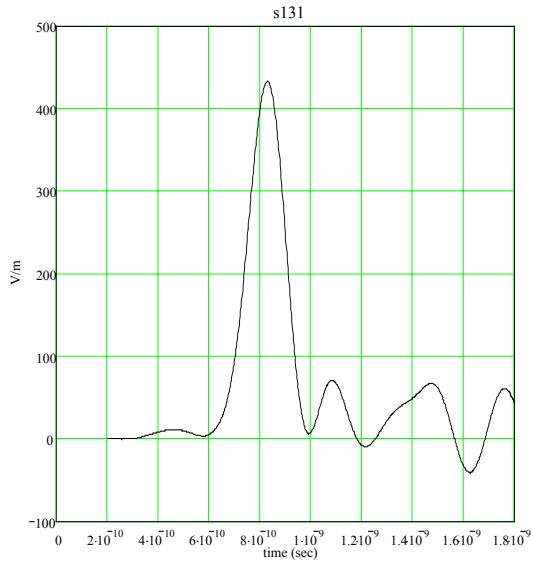
HYPS pulser/TDS820 6GHz sampling scope
 # of Antenna 1
 in phase
 normal resistive bias and shield
 axis o-q
 radius 600 (cm)
 angle (degrees) 0
 Sensor Prodyne Bdot
 Aeff 10^6m^2



HYPS pulser/TDS820 6GHz sampling scope
 # of Antenna 1
 in phase
 normal resistive bias and shield
 axis o-q
 radius 260 (cm)
 angle (degrees) 0
 Sensor Prodyne Bdot
 Aeff 10^5m^2

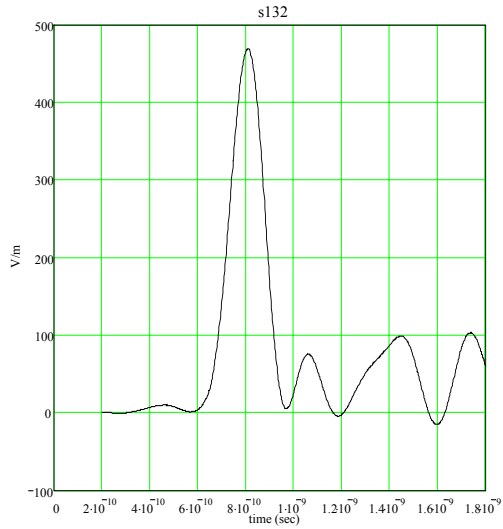


HYPS pulser/TDS820 6GHz sampling scope
 # of Antenna 1
 in phase
 normal resistive bias and shield
 axis o-q
 radius 230 (cm)
 angle (degrees) 0
 Sensor Prodyne Bdot
 Aeff 10^6m^2

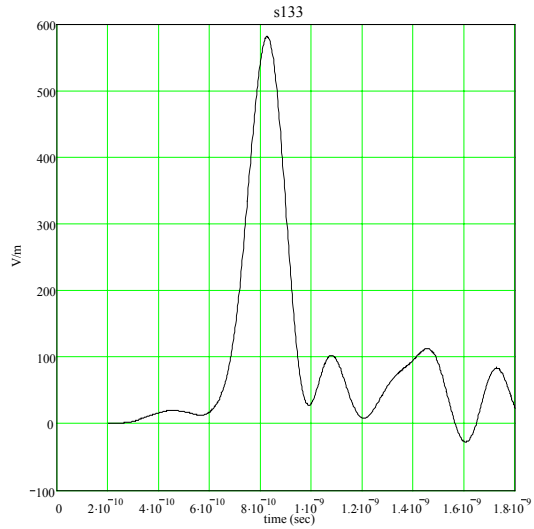


Appendix C. Datatakes 124-140(Cont.)

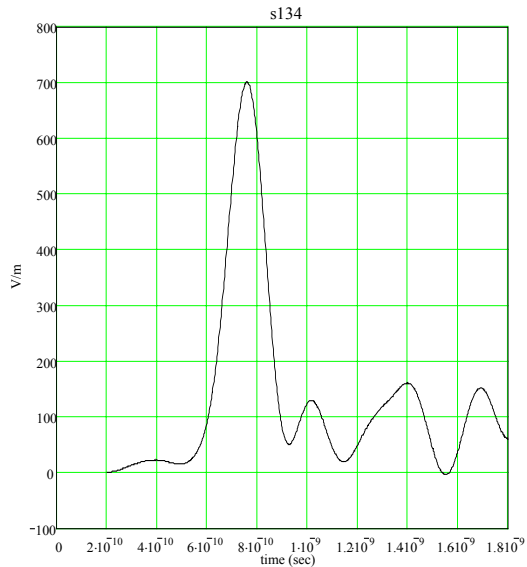
HYPs pulser/TDS820 6GHz sampling scope
 # of Antenna 1
 in phase
 normal resistive bias and shield
 axis o-q
 radius 200 (cm)
 angle (degrees) 0
 Sensor Prodyne Bdot
 Aeff $10^5 m^2$



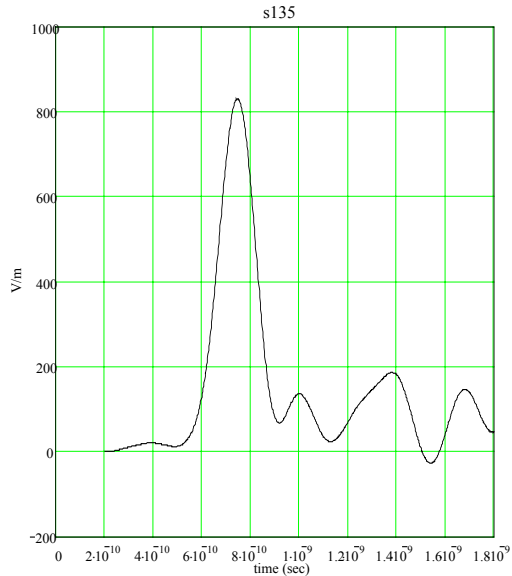
HYPs pulser/TDS820 6GHz sampling scope
 # of Antenna 1
 in phase
 normal resistive bias and shield
 axis o-q
 radius 170 (cm)
 angle (degrees) 0
 Sensor Prodyne Bdot
 Aeff $10^5 m^2$



HYPs pulser/TDS820 6GHz sampling scope
 # of Antenna 1
 in phase
 normal resistive bias and shield
 axis o-q
 radius 140 (cm)
 angle (degrees) 0
 Sensor Prodyne Bdot
 Aeff $10^5 m^2$

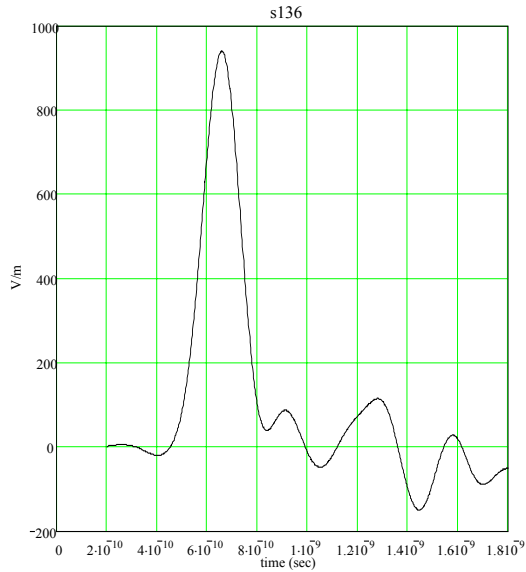


HYPs pulser/TDS820 6GHz sampling scope
 # of Antenna 1
 in phase
 normal resistive bias and shield
 axis o-q
 radius 110 (cm)
 angle (degrees) 0
 Sensor Prodyne Bdot
 Aeff $10^5 m^2$

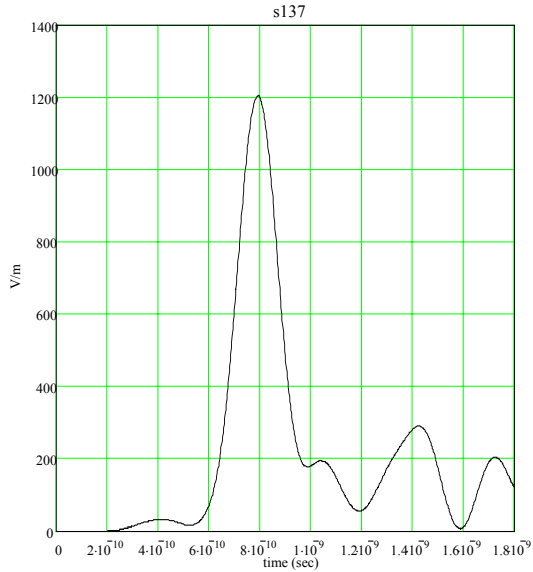


Appendix C. Datatakes 124-140(Cont.)

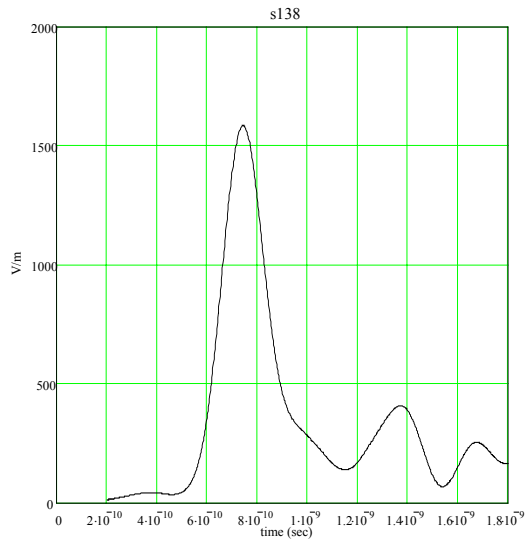
HYPS pulser/TDS820 6GHz sampling scope
 # of Antenna 1
 in phase
 normal resistive bias and shield
 axis o-q
 radius 90 (cm)
 angle (degrees) 0
 Sensor Prodyne Bdot
 Aeff 10^5m^2



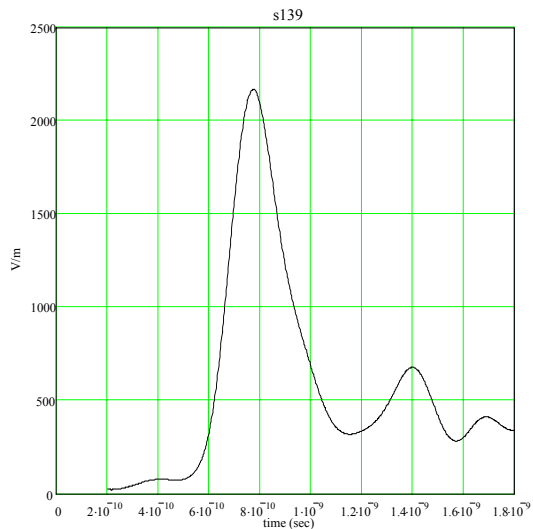
HYPS pulser/TDS820 6GHz sampling scope
 # of Antenna 1
 in phase
 normal resistive bias and shield
 axis o-q
 radius 70 (cm)
 angle (degrees) 0
 Sensor Prodyne Bdot
 Aeff 10^5m^2



HYPS pulser/TDS820 6GHz sampling scope
 # of Antenna 1
 in phase
 normal resistive bias and shield
 axis o-q
 radius 50 (cm)
 angle (degrees) 0
 Sensor Prodyne Bdot
 Aeff 10^5m^2

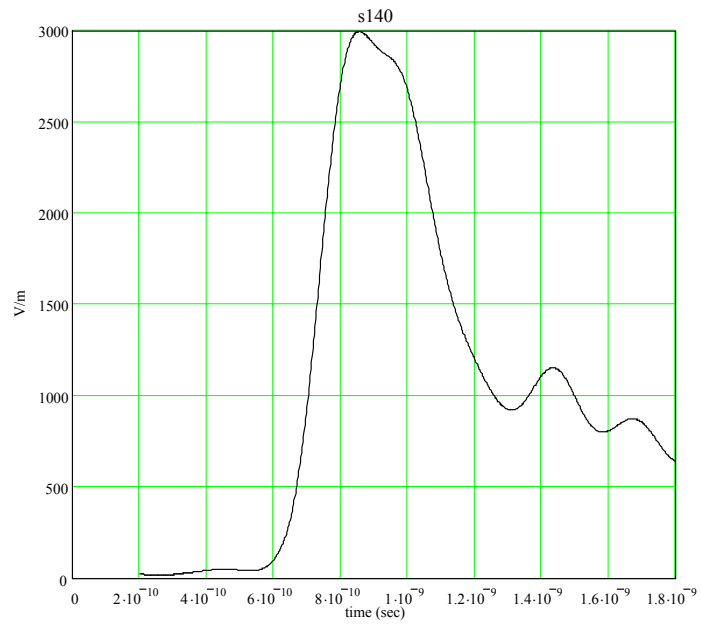


HYPS pulser/TDS820 6GHz sampling scope
 # of Antenna 1
 in phase
 normal resistive bias and shield
 axis o-q
 radius 30 (cm)
 angle (degrees) 0
 Sensor Prodyne Bdot
 Aeff 10^5m^2



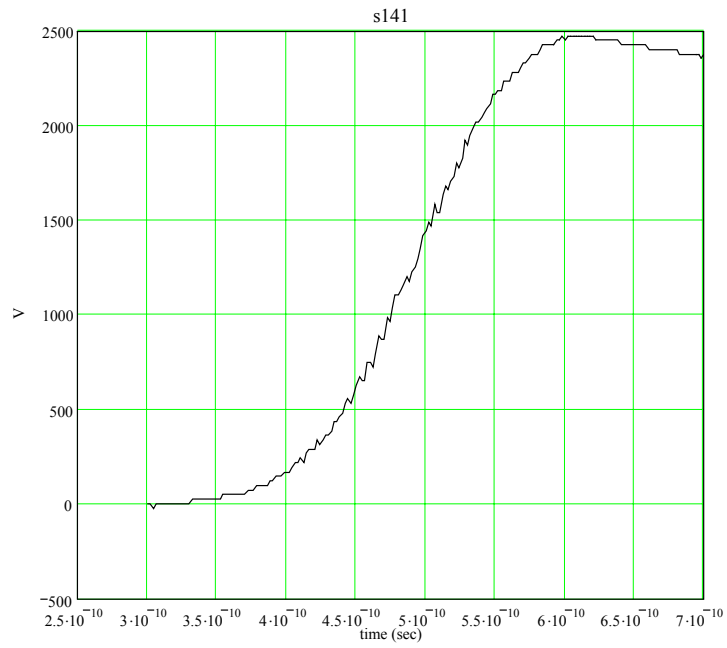
Appendix C. Datatakes 124-140(Cont.)

HYPS pulser/TDS820 6GHz sampling scope
of Antenna 1
in phase
normal resistive bias and shield
axis o-q
radius 10 (cm)
angle (degrees) 0
Sensor Prodyne Bdot
Aeff 10^{-5} m^2



Appendix C. Datatake 141.

HYPs Pulser ~169 ns rise time (flipped)
Antenna drive signal
.78 ns RG214
Barth Six Way Splitter
5:1, 10:1, 10:1

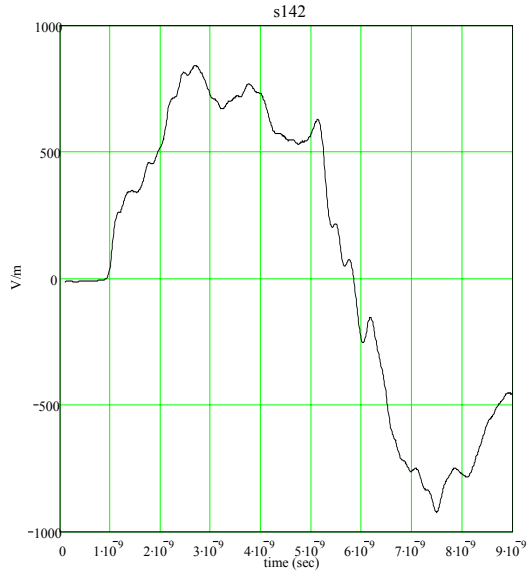


Appendix C. Datatakes 142-146.

HYPS pulser/TDS820 6GHz sampling scope

of Antenna 1
Standard resistor spacing

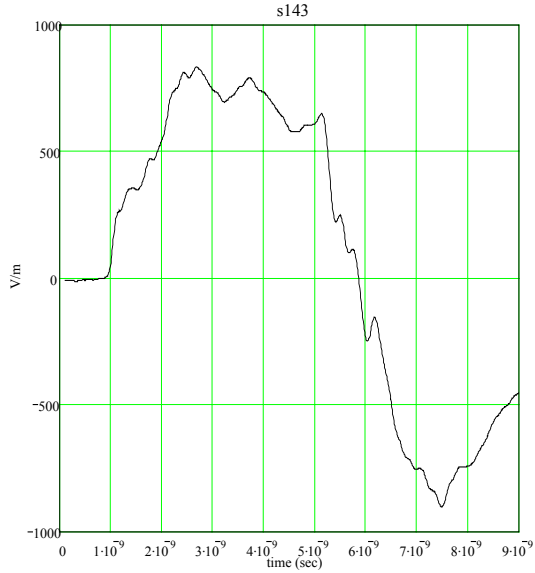
axis o-q
radius -70 (cm)
angle (degrees) 0
Sensor Prodyne Bdot
Aeff 10^5m^2



HYPS pulser/TDS820 6GHz sampling scope

of Antenna 1
wide (high L) resistor spacing

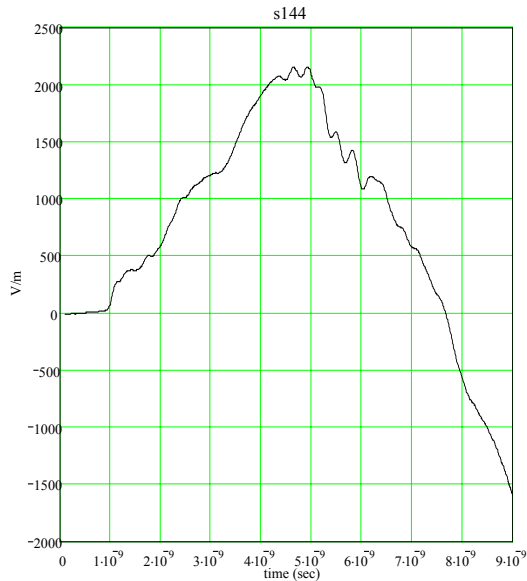
axis o-q
radius -70 (cm)
angle (degrees) 0
Sensor Prodyne Bdot
Aeff 10^5m^2



HYPS pulser/TDS820 6GHz sampling scope

of Antenna 1
LOW L setup

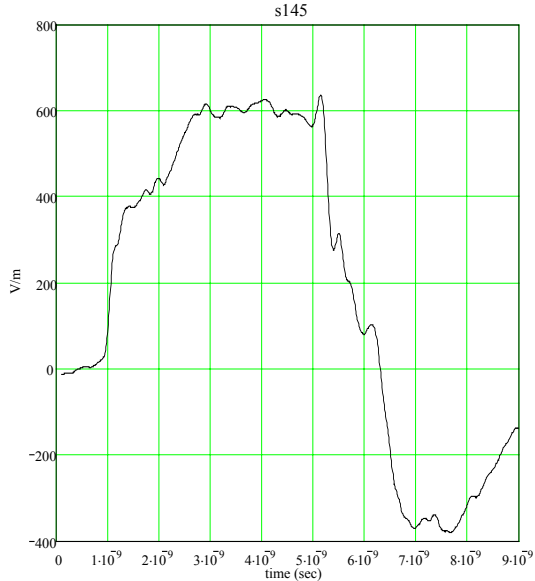
axis o-q
radius -70 (cm)
angle (degrees) 0
Sensor Prodyne Bdot
Aeff 10^5m^2



HYPS pulser/TDS820 6GHz sampling scope

of Antenna 1
High L setup

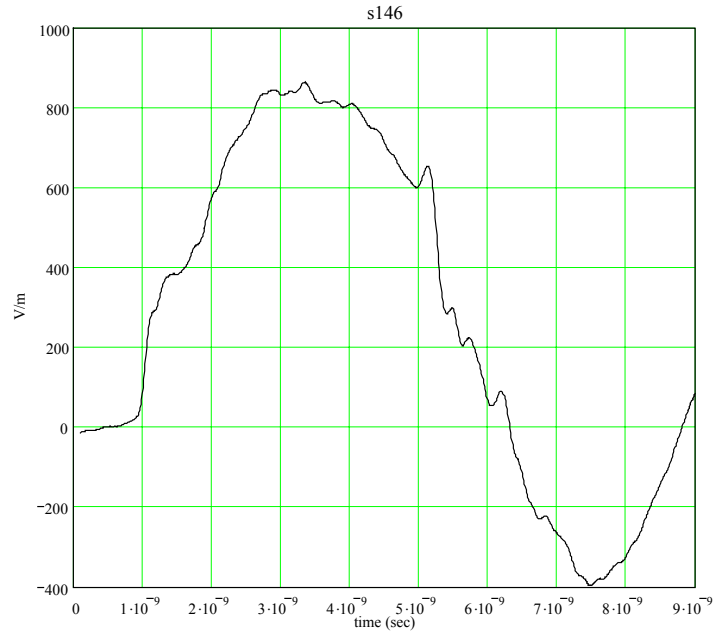
axis o-q
radius -70 (cm)
angle (degrees) 0
Sensor Prodyne Bdot
Aeff 10^5m^2



Appendix C. Datatakes 142-146(Cont.)

HYPS pulser/TDS820 6GHz sampling scope
of Antenna 1
connect res. strings together

axis o-q
radius -70 (cm)
angle (degrees) 0
Sensor Prodyne Bdot
Aeff 10^{-5} m^2



Appendix D. Details of High-Voltage Experiments



Figure D-1. View of a single TEM horn in an oil bath; energized by a hv (~ 300 kV) fast rising (~ 100 ps) pulse

DISTRIBUTION LIST

DTIC/OCP 8725 John J. Kingman Rd, Suite 0944 Ft Belvoir, VA 22060-6218	1 cy
AFRL/VSIL Kirtland AFB, NM 87117-5776	1 cy
AFRL/VSIIH Kirtland AFB, NM 87117-5776	1 cy
Official Record Copy AFRL/DEHP/Tyrone Tran	1 cy
Dave. V. Giri Pro-Tech 11-C Orchard Court Alamo, CA 94507-1541	1 cy
Vic Carboni TITAN Systems Corporation Pulse Sciences Division 2700 Merced Street San Leandro, CA 94577	1 cy